

**RL-TR-97-229, Volume II (of two)**  
**Final Technical Report**  
**February 1998**



# **ELECTRO-OPTIC COMPUTING ARCHITECTURES: COMPONENTS AND SYSTEM DESIGN AND ANALYSIS**

**Hughes Research Laboratories**

**Sponsored by**  
**Advanced Research Projects Agency**  
**ARPA Order No. A275**

**19980415 093**

*APPROVED FOR PUBLIC RELEASE; DISTRIBUTION UNLIMITED.*

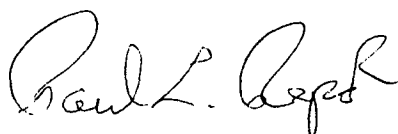
**AIR FORCE RESEARCH LABORATORY**  
**ROME RESEARCH SITE**  
**ROME, NEW YORK**

**[DTIC QUALITY INSPECTED 3]**

This report has been reviewed by the Air Force Research Laboratory, Information Directorate, Public Affairs Office (IFOIPA) and is releasable to the National Technical Information Service (NTIS). At NTIS it will be releasable to the general public, including foreign nations.

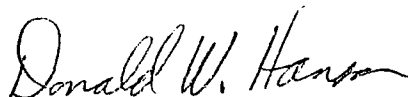
RL-TR-97-229, Volume II has been reviewed and is approved for publication.

APPROVED:



PAUL L. REPAK  
Project Engineer

FOR THE DIRECTOR:



DONALD W. HANSON, Director  
Surveillance & Photonics

If your address has changed or if you wish to be removed from the Air Force Research Laboratory mailing list, or if the addressee is no longer employed by your organization, please notify AFRL/SNDP, 25 Electronic Pky, Rome, NY 13441-4515. This will assist us in maintaining a current mailing list.

Do not return copies of this report unless contractual obligations or notices on a specific document require that it be returned.

**ALTHOUGH THIS REPORT IS BEING PUBLISHED BY AFRL, THE RESEARCH WAS ACCOMPLISHED BY THE FORMER ROME LABORATORY AND, AS SUCH, APPROVAL SIGNATURES/TITLES REFLECT APPROPRIATE AUTHORITY FOR PUBLICATION AT THAT TIME.**

ELECTRO-OPTIC COMPUTING ARCHITECTURES: COMPONENTS AND  
SYSTEM DESIGN AND ANALYSIS

U. Efron, S. Esener, C. S. Wu,  
P. J. Marchand, K. Sayyah, M. Yung,  
M. J. Little, R. A. Forber, J. A. Neff, C. Stirk

Contractor: Hughes Research Laboratories  
Contract Number: F30602-93-C-0173  
Effective Date of Contract: 12 July 1993  
Contract Expiration Date: 11 July 1997  
Program Code Number: 3D10  
Short Title of Work: Electro-Optic Computing Architectures:  
Components and System Design and Analysis  
Period of Work Covered: Jul 93 - Jul 97

Principal Investigator: Uzi Efron  
Phone: (310) 317-5806  
RL Project Engineer: Paul L. Repak  
Phone: (315) 330-3146

Approved for public release; distribution unlimited.

This research was supported by the Advanced Research Projects  
Agency of the Department of Defense and was monitored by  
Paul L. Repak, AFRL/SNDP, 25 Electronic Pky, Rome, NY.

**DTIC QUALITY INSPECTED 3**

REPORT DOCUMENTATION PAGE			Form Approved OMB No. 0704-0188	
<small>Public reporting burden for this collection of information is estimated to average 1 hour per response, including the time for reviewing instructions, searching existing data sources, gathering and maintaining the data needed, and completing and reviewing the collection of information. Send comments regarding this burden estimate or any other aspect of this collection of information, including suggestions for reducing this burden, to Washington Headquarters Services, Directorate for Information Operations and Reports, 1215 Jefferson Davis Highway, Suite 1204, Arlington, VA 22202-4302, and to the Office of Management and Budget, Paperwork Reduction Project (0704-0188), Washington, DC 20503.</small>				
1. AGENCY USE ONLY (Leave blank)		2. REPORT DATE <b>February 1998</b>		3. REPORT TYPE AND DATES COVERED <b>Final Jul 93 - Jul 97</b>
4. TITLE AND SUBTITLE <b>ELECTRO-OPTIC COMPUTING ARCHITECTURES: COMPONENTS AND SYSTEM DESIGN AND ANALYSIS</b>			5. FUNDING NUMBERS <b>C - F30602-93-C-0173 PE - 61101E/62712E PR - A275 TA - 00 WU - 01</b>	
6. AUTHOR(S) <b>U. Efron, S. Esener, C. S. Wu, P. J. Marchand, K. Sayyah, M. Yung, M. J. Little, R. A. Forber, J. A. Neff, C. Stirk</b>				
7. PERFORMING ORGANIZATION NAME(S) AND ADDRESS(ES) <b>Hughes Research Laboratories 3011 Malibu Canyon Road Malibu CA 90265</b>			8. PERFORMING ORGANIZATION REPORT NUMBER  <b>N/A</b>	
9. SPONSORING/MONITORING AGENCY NAME(S) AND ADDRESS(ES) <b>Advanced Research Projects Agency      Air Force Research Laboratory/SNDP 3701 North Fairfax Drive                      25 Electronic Pky Arlington VA 22203-1714                      Rome NY 13441-4515</b>			10. SPONSORING/MONITORING AGENCY REPORT NUMBER  <b>RL-TR-97-229, Volume II (of two)</b>	
11. SUPPLEMENTARY NOTES  <b>Air Force Research Laboratory Project Engineer: Paul L. Repack/SNDP/(315) 330-3146</b>				
12a. DISTRIBUTION AVAILABILITY STATEMENT  <b>Approved for public release; distribution unlimited.</b>			12b. DISTRIBUTION CODE	
13. ABSTRACT (Maximum 200 words) <b>The objective of the Electro--Optic Computing Architecture (EOCA) program was to develop multi-function electro-optic interfaces and optical interconnect units to enhance the performance of parallel processor systems and form the building blocks for future electro-optic computing architectures. Specifically, three multi-function interface modules were targeted for development - an Electro-Optic Interface (EOI), an Optical Interconnection Unit (OIU), and a Space-Time Compander (STC). Electro-optic 3-D interconnection module stacks were assembled, allowing for system global communication and fast efficient data routing and sorting. The achieved goal of the system study, to identify and analyze all the architectural implications due to the addition of optical based free-space interconnects in locally connected processor arrays, is leading to new highly optimized 3-D electro-optic computer processing networks.</b>				
14. SUBJECT TERMS <b>Optical Processing, Optical Computer Architecture, Optical Switching, Micro Optical Circuits</b>			15. NUMBER OF PAGES <b>110</b>	
			16. PRICE CODE	
17. SECURITY CLASSIFICATION OF REPORT  <b>UNCLASSIFIED</b>	18. SECURITY CLASSIFICATION OF THIS PAGE  <b>UNCLASSIFIED</b>	19. SECURITY CLASSIFICATION OF ABSTRACT  <b>UNCLASSIFIED</b>	20. LIMITATION OF ABSTRACT  <b>UL</b>	

# CONTENTS

	Page
1 INTRODUCTION .....	1
1.1 Electro-Optical Interface.....	1
1.2 Optical Interconnection Unit.....	2
1.3 Space-Time Compander.....	2
1.4 System Analysis.....	3
2 ELECTRO-OPTICAL INTERFACE .....	4
2.1 Flip-Chip Bonded Si/PLZT.....	4
2.2 Bypass-and-Exchange Switch Array .....	5
2.2.1 Design A .....	6
2.2.2 Design B.....	9
3 OPTICAL INTERCONNECTION UNIT .....	12
3.1 Transpose Interconnection .....	12
3.2 Relation Between OTIS and the Shuffle Exchange Network.....	14
3.3 OTIS System Analysis.....	15
3.3.1 Optical System Characterization and Derivations .....	15
3.3.2 System Power Considerations.....	16
3.3.3 Generalized System.....	18
3.3.4 Folded System.....	20
3.3.5 Bi-Directional System.....	22
3.3.6 Multi-Channel System .....	22
3.3.7 OTIS Issues.....	25
3.4 OTIS Design Verification .....	29

## CONTENTS (Continued)

		Page
4	SPACE-TIME COMPANDER.....	31
4.1	CCD-Based Liquid Crystal Imager/Modulator.....	32
4.1.1	CCD-LCLV Based Space-Time Compander.....	33
4.1.2	Mechanical Design.....	35
4.1.3	Electronic Driver Design .....	36
4.1.4	Optical Interfaces .....	36
4.2	CCD Design for STC Applications.....	37
4.2.1	CCD Design Analysis .....	38
4.2.2	CCD Design Analysis Tools.....	40
4.2.3	CCD Design Analysis Results .....	46
5	EOCA SYSTEM ANALYSIS .....	48
5.1	Electronic Versus Optical Interconnects in the 3-D Computer.....	48
5.1.1	Architecture Consideration .....	48
5.1.2	Technology Consideration .....	49
5.2	Optically Augmented 3-D VLSI Computer .....	56
5.2.1	The Optical Transpose Interconnection System .....	56
5.2.2	Additional Consideration on OTIS .....	58
5.2.3	Time Dilated Network .....	59
5.3	Applications Studies .....	62
5.3.1	FFT Studies.....	62
5.3.2	Routing and Sorting Applications.....	85
6	REFERENCES.....	93

# ILLUSTRATIONS

	Page
1-1 Basic Building Block of Electro-Optic Computer Architectures.....	2
2-1 Cross Section of a Flip-Chip Bonded Si/PLZT Smart Pixel.....	5
2-2 Basic Building Block of Electronic 1/2 Switches.....	6
2-3 Block Diagram of a 16-Channel Switch.....	7
2-4 Half-Switch (Design A).....	8
2-5 Cumulative Delays During Signal Propagation Through the Switch.....	9
2-6 Block Diagram of Half-Switch (Design B).....	10
3-1 Input and Output Plane of 16×4 OTIS, Showing Major and Minor Index Patterns as well as the Transpose Mapping of a Typical Signal Pattern .....	13
3-2 Side View of the OTIS Showing Imaging Through Coupled Lenslets Arrays.....	14
3-3 Off-Axis Illumination and Vignetting for a Light Transfer Located at the Edge of the Array.....	17
3-4 OTIS System for Accommodating Arbitrary Optoelectronic Layouts .....	18
3-5 Folded (Reflective) OTIS Configuration.....	21
3-6 Bi-Directional OTIS.....	23
3-7 Multi-Channel OTIS Implementation.....	24
3-8 Area Multiplexed Illumination Lenslets for the OTIS.....	25
3-9 Volume Holographic Beamsplitter for the OTIS.....	28
3-10 Experimental Setup for the 64×64 OTIS.....	29
3-11 Experimental Results for a 64×64 OTIS Interconnection.....	30
4-1 Schematic of Space-Time Compander Interface .....	31
4-2 Schematics of One Superpixel of the Space-Time Compander.....	32
4-3 Cross Section of the CCD-LCLV with Conductive Feedthrough in the Supporting Glass.....	34
4-4 The Concept of Using Microlens Array for Mapping Optical Images to Physically Separated CCD Arrays.....	37
4-5 Floorplan of One Superpixel of STC Indicating Direction of Charge Flow.....	39
4-6 (a) Spreadsheet Program and Plots for the epi Layer, the Replacement Well Implanted Profile, and the Threshold Implanted Profile.....	41
4-6 (b) Spreadsheet Program and Plots for the epi Layer, the Replacement Well Implanted Profile and the Threshold Implanted Profile.....	42

## ILLUSTRATIONS (Continued)

	Page
4-7 Spreadsheet Program for the calculating the Charge Transfer Efficiency, the Full Depletion Voltage Under the CCD Gate, the Threshold Voltage Body Factor and the Junction Capacitance Coefficients of the MOS Transistor in the Output Amplifier.....	43
4-8 Cross-Sectional 2-D Potential Profile of the Output MOS Transistor Showing the Separation of the Depletion Edges From the Source and the Drain, as Generated by Punch-Through Simulation Using PISCES .....	44
4-9 Output Amplifier Circuit Schematic, Device Models and the Voltage and Current Waveforms as Generated by Circuit Simulation Using SPICE .....	45
4-10 Floorplan of Space-Time Comander Chip .....	47
4-11 Space-Time Comander Superpixel (8×8 Array) Layout .....	47
5-1 Electronic vs. Optoelectronic Global Connections in a 3-D Computer System .....	50
5-2 (a) Physical and Circuit Equivalent Model of Electrical Connection in the 3-D VSLI Computer.....	51
5-2 (b) Simplified Circuit Equivalent Model of an Optoelectronic Interconnection .....	51
5-3 (a) Energy Requirements s. Line Length for Optoelectronic and Electronic Interconnections in the 3-D Computer.....	55
5-3 (b) Break-Even Line Length for Optoelectronic vs. Electronic Connections in the 3-D Computer .....	55
5-4 Figure 5-4. OTIS as a $\sqrt{P}$ -Shuffle Interconnection .....	57
5-5 Bi-Directional OTIS for Switching Applications .....	58
5-6 Principle of the Assembly of the Optically Augmented 3-D VLSI Computer .....	59
5-7 Performance of the Time-Dilated Network for (a) Random Traffic and (b) Permutation Traffic .....	61
5-8 OTIS for a Bit-Serial Connection Between PEs.....	73
5-9 OTIS for a Bit-Parallel Communication Between PEs.....	73
5-10 Bit-Serial/Custom Electronic Chips Approach.....	75
5-11 Bit-Parallel/COTS Chips Approach.....	80
5-12 A Simplified Version of a Two-Stage Electro-Optical Network.....	86
5-13 The 2S-EON as a Particular Case of the Expanded Delta Network .....	87
5-14 Schematic of Delta Network Constructed Using $n \times n$ Switches.....	88
5-15 With Global Control, Delta Network is a Two-Pass Network.....	89
5-16 Shearsort Algorithm: Two Dimensional Computation Model for $n \times n$ Array.....	90



## ILLUSTRATIONS (Continued)

	Page
5-17 The Basic Allowed Operations for the Shearsort Algorithm.....	90
5-18 Zero-One Principle.....	91
5-19 Proof Using the [0,1] Principle .....	92
5-20 Typical Embedding for Shearsort .....	92
5-21 Mapping the Shearsort into the Two-Stage Electro-Optical Network.....	92

# TABLES

	Page
5-1 Performance Comparison of the Regular And Augmented 3-D VSLI Computer for Image Processing.....	49
5-2 Performance Comparison of DSP and Dedicated FFT Chip-Sets .....	65
5-3 Summary of 2-D Complex FFT Performance of Various Super-Computer Configurations.....	66
5-4 Today's and Future Parameters for MCM Implementation.....	68
5-5 Power Consumption of On-Chip Wires for 0.8 $\mu\text{m}$ CMOS.....	69
5-6 Power Consumption of On-Chip Wires for 0.35 $\mu\text{m}$ CMOS.....	69
5-7 Performance of MCM Connections .....	69
5-8 Power Consumption of a Optoelectronic Link for 0.8 $\mu\text{m}$ CMOS .....	71
5-9 Power Consumption of a Optoelectronic Link for 0.35 $\mu\text{m}$ CMOS .....	71
5-10 Design Parameters of the FPU and Memory for the Bit-Serial/Custom-Chip Optoelectronic Approach .....	76
5-11 Summary of Area and Power Requirements of the Various System Components.....	77
5-12 Performance Results for the Bit-Serial/Custom Chips Optoelectronic FFT Approach.....	78
5-13 Performance Results for the Bit-Parallel/COTS Chips Optoelectronic FFT Approach.....	81
5-14 Performance of the Bit-Serial/Custom-Electronics MCM Implementation .....	83
5-15 Performance of the Bit-Parallel COTS-Chip MCM Implementation .....	84

# Section 1

## INTRODUCTION

Future high performance parallel computing systems must rely on the development of a high throughput three-dimensional interconnection system. To maximize the throughput while minimizing crosstalk and power requirements, the Electro-Optic Computing Architecture (EOCA) program seeks to add global inter-wafer optical interconnection capability to locally connected parallel processors (e.g., the Hughes 3-D computer and Multiple-Chip-Module processors). This would enable us to (a) free the processor from its present I/O limitations, allowing efficient parallel communication with optical memories and sensors; (b) allow an efficient coupling of optical co-processors to handle fine grain image processing and global 2-D operations at throughput rates exceeding terabits/sec; (c) allow efficient sorting operations to be carried out through the use of optical shuffling, with expected enhancements of about 100:1.

The objective of the EOCA program is to develop multi-function electro-optic interfaces and optical interconnect units to enhance the performance of the locally connected parallel-processor system and form the building blocks for future electro-optic computing architecture. Specifically, three multi-function interface modules: Electro-Optical Interface (EOI), Optical Interconnection Unit (OIU), and a Space-Time Comander (STC) – will be developed. A conceptual schematic of the EOCA system is depicted in Figure 1-1. Under the first year development tasks we designed all three interface modules and analyzed the component design. In parallel, we designed an EOCA based on parallel processing and interconnection architecture. A design analysis of the system and performance comparison were also carried out.

A brief overview of the design/design analysis effort is given next. A detailed description of this effort is given in Sections 2 to 5 below.

### 1.1 ELECTRO-OPTICAL INTERFACE

To couple locally connected processor arrays with optical interconnection, it is critical to integrate opto-electronic interface devices directly on silicon substrates. This can be realized by integrating light detectors and light transmitters, such as PLZT or III-V multiple quantum well (MQW) light modulators, on silicon wafers. The EOI allows bi-directional communication between a parallel electronic processor and a parallel optical interconnect unit over coarse-grain arrays. A 4×4 array of PLZT modulators with a silicon driver circuit has been designed for an EOI demonstration. The driver can deliver up to 35 V voltage swing, from a standard 5 V power supply, to activate PLZT modulators. In addition, two generations of electronic bypass-and-exchange switch arrays have been designed.

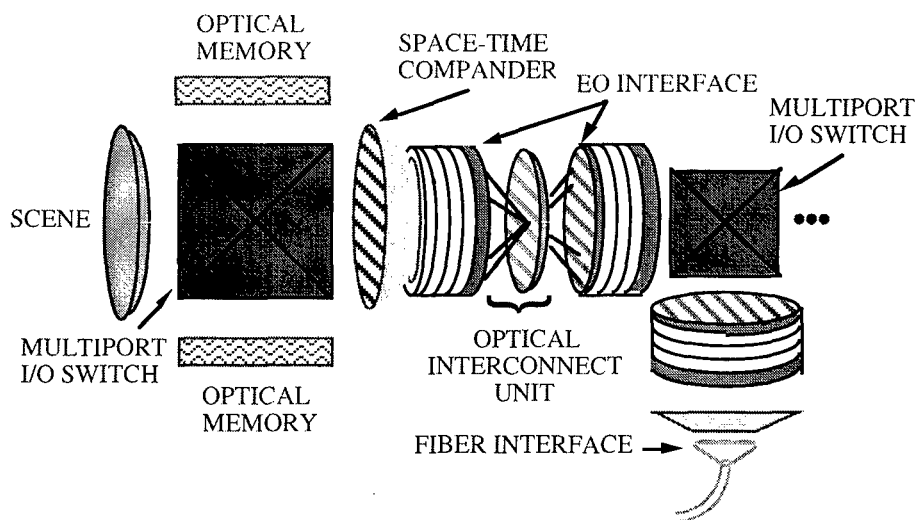


Figure 1-1. Basic building block of electro-optic computer architectures.

## 1.2 OPTICAL INTERCONNECTION UNIT

One of the key components of the proposed EOCA system is the OIU that provides the global interconnections. The optical transpose interconnection system (OTIS) is a simple, efficient, and scaleable means of providing a transpose interconnection utilizing only a pair of lenslet arrays. A detailed analysis of the OTIS optical system has been conducted as part of design analysis work. The geometrical relations for the optical system have been derived, including lens positions, system length, and system volume. The analysis of the OTIS system raises some important issues. First, the insertion losses are relatively high and must be reduced. Second, the use of a conventional Polarizing Beam Splitter (PBS) will create non-uniformity and crosstalk. Appropriate approaches, such as off-normal illumination and polarizing volume holographic beamsplitter, have been proposed to address those issues.

## 1.3 SPACE-TIME COMPANDER

The key function of the STC is to match fine-grain images with coarse-grain processor arrays. The function of size matching is performed by grouping every set of  $8 \times 8$  pixels in fine-grain images into a supercell. Each supercell is then registered with the corresponding processor in the coarse-grain processor arrays. By either compacting  $8 \times 8$  pixels into a supercell or expanding a supercell into  $8 \times 8$  pixels, the STC provides a bi-directional communication between a fine-grain image and a coarse-grain processor array.

In the area of the STC effort we first started the design analysis of the compander. A combined modulator/detector approach was selected to allow an efficient use of the compander surface area as an interface to a future ultra high resolution device. We then designed a  $128 \times 128$  pixel CCD-based STC. The heart of the combined modulator/detector STC is an  $8 \times 8$  charge-coupled device (CCD)

superpixel that can convert a parallel optical input into a serial electrical signal and vice versa. We completed two baseline designs of superpixel array (2 phase and 3 phase serial CCD) for the STC. The issues of device packaging and signal link have also been examined. We also laid out an optical design to link a fine-grain 2-D image to superpixels on the coarse-grain processor arrays.

#### **1.4 SYSTEM ANALYSIS**

It has been shown, architecturally, it is critical to add global interconnection capability to the locally connected parallel processor arrays to improve its processing speed particularly for image processing applications. The goal of this study is to identify and analyze all the architectural implications due to the addition of free-space optical interconnects in the locally connected processor array. To that effect, we first developed models for both electronic and free-space optical interconnect technologies. These interconnection models allow us to assess the unique advantages of our optically augmented 3-D computer approach. We also developed energy requirements and time-delay models for RC limited lines in the 3-D computer, for Si-CMOS receivers, and for three types of light transmitters (VCSELs, MQW modulators, PLZT modulators). In addition, we developed a model for terminated lines (transmission lines) as well as our global optoelectronic interconnect system. Results show significant advantages for free-space optical interconnects vs. RC limited lines in the 3-D computer environment. We also optimized the architecture of the one stage-shuffle interconnection network for permutation traffic in the 3-D computer and developed the concept of the time-dilated network. The performance of the EOCA system was also studied for (1) routing and sorting and (2) FFT applications.

## **Section 2**

# **ELECTRO-OPTICAL INTERFACE**

The EOI provides bi-directional communication between a parallel electronic processor and a parallel optical interconnect unit over coarse-grain arrays. In order to couple locally connected processor arrays with optical interconnection, it is critical to realize opto-electronic interface devices by integrating light detectors and light transmitters with silicon wafers. Flip-chip bonding is a mature and well-developed technique used extensively for silicon packaging. This technology is implemented in this program for Si/PLZT optoelectronic technology. A high voltage amplifier circuit has been designed for the need of flip-chip bonded Si/PLZT smart modulator. We have designed a 4×4 array of Si/PLZT smart modulator for an EOI demonstration (see Section 2.1). In addition, electronic bypass-and-exchange switches play an equal important role in implementing an efficient optoelectronic interconnection system. Two generation electronic bypass-and-exchange switch arrays have been designed and a 16×16 (16 inputs, 16 outputs) switch has been designed (see Section 2.2).

### **2.1 FLIP-CHIP BONDED Si/PLZT SMART PIXEL**

In the hybrid Si/PLZT optoelectronic technology a PLZT wafer is used both as a support substrate and for light modulation. The electronic driver circuitry is built on the silicon chips and connected to the PLZT modulator through metal bumps (as schematically shown in Figure 2-1). The silicon chips can be tested separately before placement on PLZT to insure a high yield process. The flip-chip process then mechanically aligns the silicon wafers to the corresponding PLZT modulators. To achieve a large dynamic range PLZT generally requires 20-40 V to modulate an external light. High voltage bipolar and MOS processes are presently incapable of supporting VLSI circuit densities. On the other hand, transistor breakdown voltages in VLSI chips are too low to provide high voltage outputs directly. We have designed a special circuit capable of delivering a driving voltage swing up to 35 V from a standard 5 V power supply. High breakdown voltage of the circuit is accomplished using series connected transistors and a current-mirror like structure.

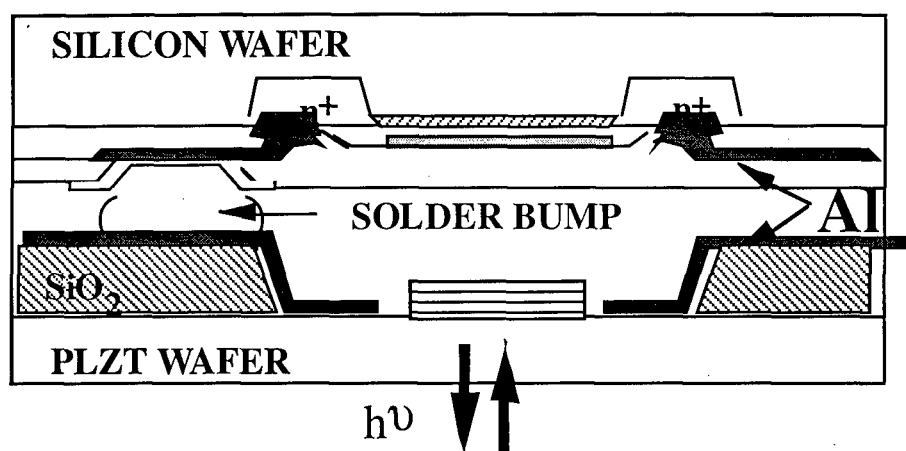


Figure 2-1. Cross section of a flip-chip bonded Si/PLZT smart pixel.

We have designed and integrated a 4×4 array of reflective PLZT modulators with the silicon driver circuit. The combination of the driver and the reflective PLZT modulator produces light modulation with a dynamic range of up to 600:1. Studies of speed response of PLZT 9.5/65/35 showed the rise and fall times to be less than 10 ns each, fundamentally limited by the driver circuitry. The Si/PLZT smart pixel is capable of building an optical link with a bit-error rate (BER) better than  $10^{-14}$  under the following experimental conditions:

- 5 Mbits/sec data rate
- 4×4 array of 40×40 μm modulators
- Modulator bias at 60 V
- Modulator voltage swing at 25 V
- 300 μW optical input per modulator with 10 μm spot

The output power swing was measured at 100 to 200 μW per modulator over the array.

Alternatively, MQW modulators can also be flip-chip bonded to 3-D silicon. In this case the driver circuit can be located either on the 3-D stack or be monolithically integrated with the modulator structure on the GaAs. In the case of a one-to-one optical interconnection system, MQW structures offer advantages over PLZT modulators. First, the driver requirements are dramatically reduced since MQW modulators can operate simply with logic-level voltage swings. Second the same MQW structure can be used either as a modulator or as a detector. And both input and output optical devices will lay on the same plane. This would eliminate the critical requirements for aligning the processor array with the optoelectronics. Further modifications might include using the same MQW structure as a bi-directional device (detector and modulator) in conjunction with a bi-directional driver/amplifier circuit.

## 2.2 BYPASS-AND-EXCHANGE SWITCH ARRAY

To achieve efficient data communication in the optoelectronic network, a key component is the electronic switch that performs the local routing of the data. A switch is implemented by cascading 2×2 bypass-and-exchange switches, partitioned into two 2-to-1 multiplexers, called half-switches

switch (as shown in Fig. 2-2). A pair of such half-switches is called partner half-switches. Every half-switch gets an input of its own, plus the input of its partner half-switch as its second input. Depending on the control signal, which can be fed externally (global control) or can be computed internally (self-routing), each half-switch transmits one of the two possible inputs to its single output. We further extended the switch to be bi-directional; the data flow direction can be controlled by one single control bit. Thus both inputs and outputs can be exchanged in the same switch. A complete  $16 \times 16$  switch consists of  $\log_2 N = 4$  stages of  $N = 16$  half-switches each, for a total of  $N \log_2 N = 64$  half-switches. The block diagram of a 16 channel switch is shown in Fig. 2-3.

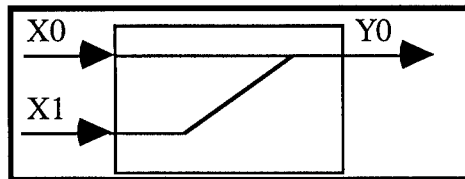


Figure 2-2. Basic building block of electronic 1/2 switches.

Two different half-switches have been designed for the OTIS. The first one, design A, is a simple, bi-directional 2-to-1 multiplexer. This was built as a proof of concept for the 2-D layout, and the operation of a half-switch as the building block of the complete switch. The second design, design B, is a novel self-routing half-switch, that can detect contention, and drop-and-resend data packets.

### 2.2.1 Design A

The block diagram of design A is shown in Fig. 2-4(a).<sup>(2-1)</sup> The half-switch uses an external direction signal that is also broadcast to every other half-switch in the entire switch. This signal determines the direction of the data flow. The direction signal is arbitrarily chosen to be 1 (dir is the direction signal) for a left to right data flow. In this case,  $x_0$  and  $x_1$  are the two inputs and  $y_0$  is the output, while  $y_1$  is floating. Another external control signal is sent to the half-switch, controlling which input channel it should transmit to its output. Again arbitrarily,  $c$  is chosen to be 1 ( $c$  is the control signal) when  $x_1$  is to be transmitted, and similarly,  $c = 0$  causes  $x_0$  to go through. If direction is reversed (i.e.  $dir = 0$ ), then  $c = 0$  causes  $y_0$  to be sent to  $x_0$ , and  $c = 1$  causes  $y_1$  to be sent to  $x_0$ . In this design, only four control bits are used for a four stage switch, labeled  $c_0$  through  $c_3$  (refer to Fig. 2-3). The same control bit is sent to all the half-switches on the same stage. As a result, only the final output destination of a single input can be determined, whereas the remaining 15 inputs go to the other 15 outputs without contention.



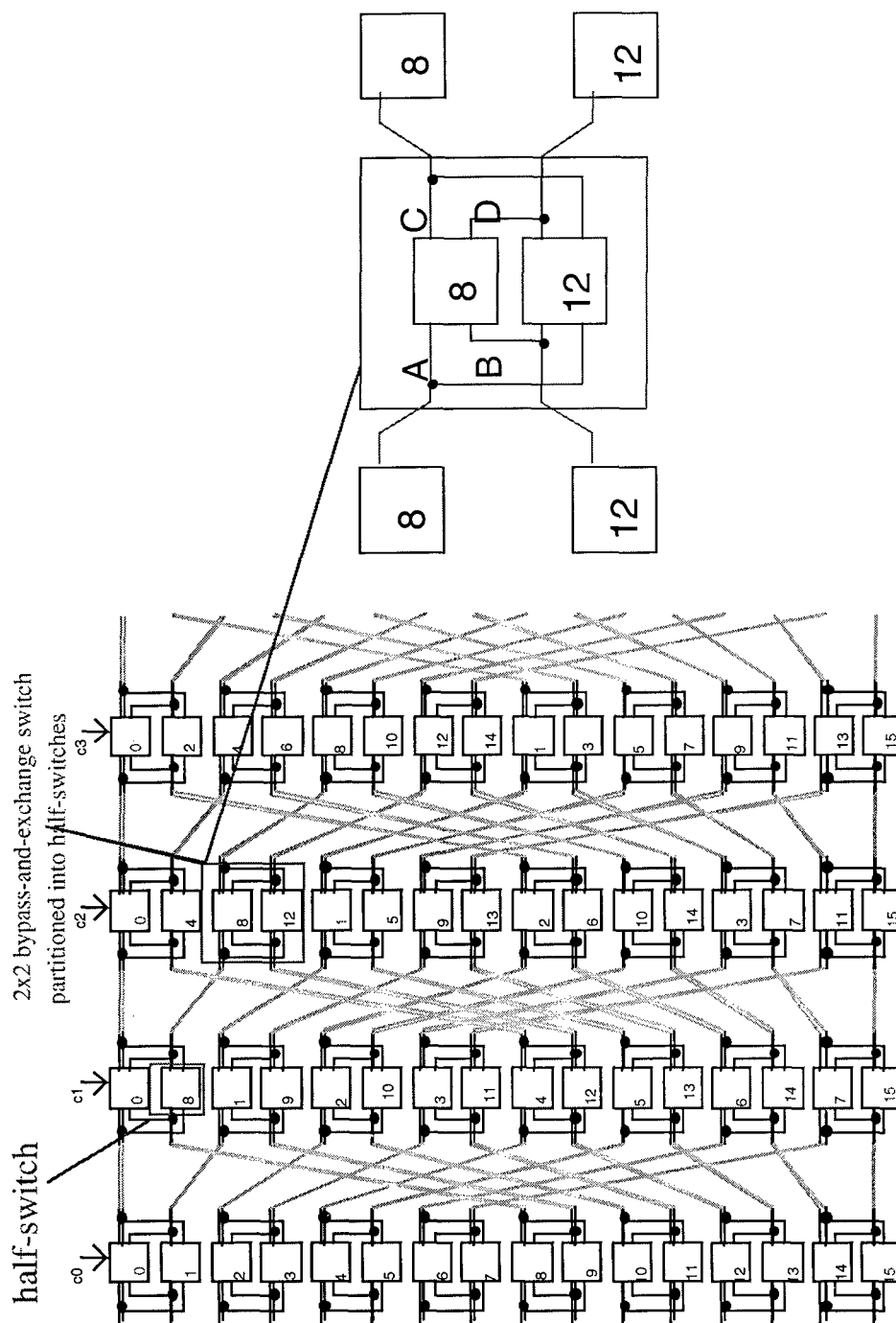


Figure 2-3. Block diagram of a 16-channel switch.

Figure 2-4(b) shows the circuit schematics for design A. The numbers next to the transistors give width/length in units of  $\lambda$ . The half-switch is implemented with only 24 transistors. For a given direction signal, half of the transistors are not used. As an example, if  $\text{dir} = 1$ , transistors M13 - M24 are not used since M13 and M16 block their final output. In addition, for that given direction signal, the control signal determines which input will be transmitted. For example, if  $c = 1$ , M5 and M8 block  $x_0$ , and  $x_1$  is sent through. Similarly, if  $c = 0$ , M1 and M4 block  $x_1$ , and  $x_0$

is transmitted. Effectively, for a given direction and control signal, the input is inverted twice to reach the output. Due to this simple structure, high-speed operations are achievable. For a 2.0  $\mu\text{m}$  CMOS technology, simulations showed a maximum speed of 250 Mbits/s.

For one input to output connection within the switch, the cumulative propagation delay per half switch is shown in Figure 2-5. The time indicated on top of each half switch shows how much the control bits must be delayed as the data progresses in the switch. To speed up the overall system

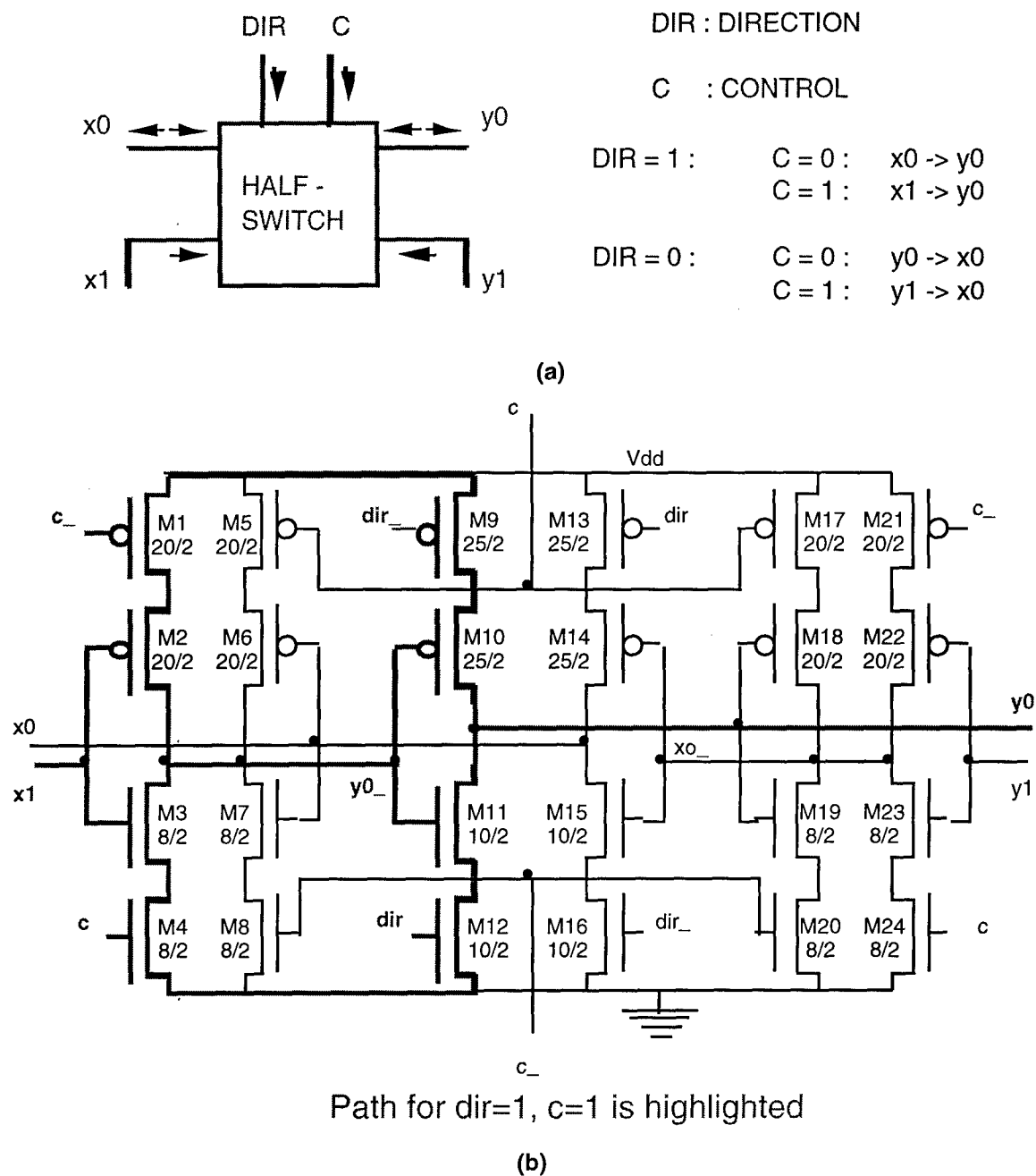


Figure 2-4. Half-Switch (design A). (a) Block diagram and truth table. (b) Circuit schematics.

and to make it scaleable, the control signals,  $c_0$ - $c_3$ , are fed into the switch in a pipelined fashion. In other words, the control bit,  $c_1$ , which belongs to the second stage is delayed externally by the same amount of time it takes for a signal to propagate through the first stage of half-switches. Similarly, the control bit to the third stage,  $c_2$ , is delayed twice that amount, and so on. This method ensures that the control signal and the inputs of a given stage arrive at the same time at the desired half-switches. Then, the speed of the overall system is directly equal to the speed of a single half-switch. As the switch size increases, the number of stages and the total number of half-switches increase. But, the overall speed stays constant since the propagation delay of a single half-switch is constant.

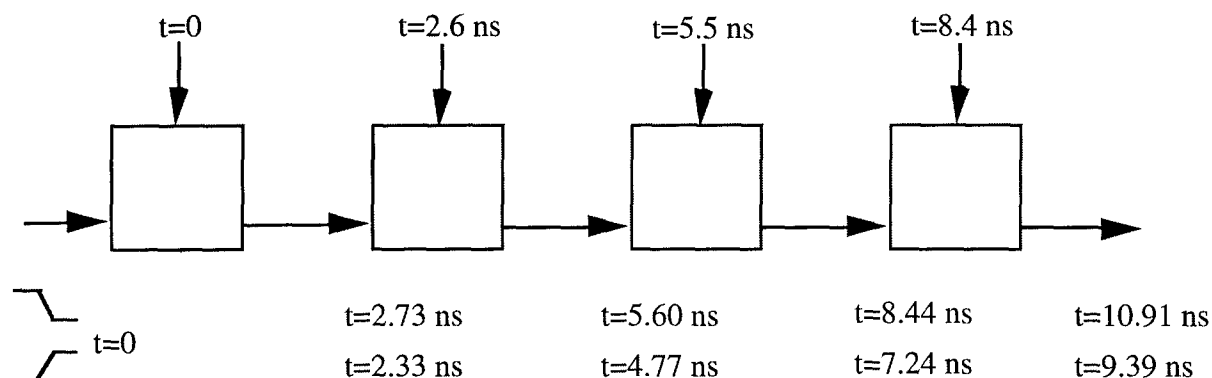
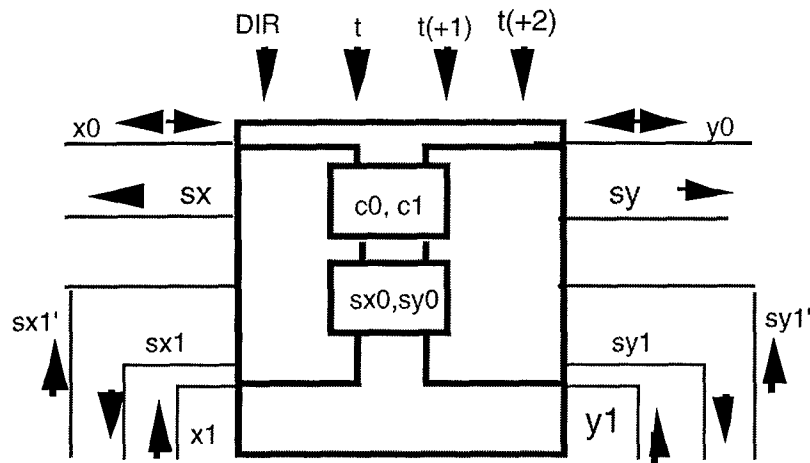


Figure 2-5. Cumulative delays during signal propagation through the switch.

### 2.2.2 Design B

Design B is built upon design A, but it adds functionality to the switch operation. The block diagram is shown in Fig. 2-6. It still acts as a 2-to-1 multiplexer. However, it has built-in self-routing capability, that is, the control bit for each half-switch is computed internally. Every input packet contains as a header, the address of its desired output destination (i.e. for  $N = 256$  channels,  $\log_2 N = 8$  bits of address are needed). As data packets are presented, the half-switches in the first stage process the first bit of each of their inputs, and decide on their control signal. The remaining 23 bits are then transmitted untouched. The same processing is done in the next stages until the data packet arrive at their output destination.



DIR : DIRECTION

t : TRANSMISSION ( = 1 FOR DATA BIT,  
= 0 FOR ADDRESS BIT )

t(+1) : t DELAYED BY ONE CYCLE

s : CONTENTION DETECTOR

c0 : CORRESPONDS TO " C " OF DESIGN A

c1 : =1 IF c0 IS A DON'T CARE

**Figure 2-6. Block diagram of Half-Switch (design B).**

As packets are transmitted through the switches, two of them may have to use the same half-switch to arrive at their output, and thus, there is contention (hot spot). In this case, the half-switch transmits one of the inputs in a deterministic way, and drops its other input. At the same time, to ensure that the dropped data is not lost, a contention signal is generated within the half-switch, where the blocking happened. This contention signal propagates in the direction opposite to the data flow, and follows backwards, the path that the dropped packet of data had followed up to that point. Once it reaches the dropped packet's input buffer, it sets the input buffer to resend the same packet, so that all the information is eventually routed through the network.

In this design, the direction of data flow is again determined by an external direction signal supplied to all the half-switches. In addition, an external transmission signal (t is the transmission signal) is provided to inform each half-switch that data transmission is occurring. This signal is set to 1 if the incoming bit is a data bit, and is set to 0 if it is an address bit. Therefore, for all the half-switches at a given stage,  $t = 0$  during the first cycle of a data packet, and  $= 1$  for the remaining 23

cycles. Just like in design A, the transmission signal is pipelined, that is, delayed by the same amount of time that the input takes to reach that stage. As a result, a transmission signal of 0 for 1 cycle, and 1 for 23 cycles, propagates from stage to stage at the same speed that the data propagates, with the 0 bit arriving at a stage when the control signals are to be computed at that stage (i.e. the incoming bits are address bits). This way, a single pulse of  $t = 0$  at the input buffer stage enables all the half-switches in the entire switch to know exactly when to process the incoming bits as their address bits rather than data bits. As each data packet is introduced into the pipeline, first the address bits are processed. This processing of the header of a data packet takes exactly  $2\log_2 N$  cycles, where a cycle is equal to the duration of a single bit. This is the time it takes for the last address bit (i.e. the  $(\log_2 N)^{\text{th}}$  bit) to be processed by the last stage (i.e. the  $(\log_2 N)^{\text{th}}$  stage). After that, the speed of that channel's throughput is equal to the speed of a single half-switch, since the pipeline is completely filled up at this point.

## Section 3

# OPTICAL INTERCONNECTION UNIT

The OIU allows a parallel optical interconnect to another EOI unit, thus enabling interconnection between two parallel electronic processors. The OIU further allows data shuffling to enable global operation (such as sorting) to be performed in the parallel electronic processors. The optical system includes the interconnection lenslets, based on the Optical Transpose Interconnection System (OTIS), and the elements required to power-up the modulators.

The Optical Transpose Interconnection System (OTIS) is a simple, efficient, and scalable means of providing a transpose interconnection utilizing only a pair of lenslet arrays. For the OIU applications the interconnection lenslets must provide the following requirements: high light efficiency and bi-directionality. The usefulness of the transpose interconnection has previously been shown for three architecture classes,<sup>(3-1)</sup> namely, shuffle-based multistage interconnection networks, mesh of trees matrix processors, and hypercube interconnections. Section 3.1 briefly reviews the transpose interconnection functionality and Section 3.2 describes the application of OTIS for shuffle exchange networks. Section 3.3 describes the basic OTIS optical system and various scalability parameters are analyzed including system length, system efficiency, and crosstalk. Variations of the basic OTIS optical system for different applications are introduced, namely a generalized system to match the geometry of any arbitrary optoelectronic chip layout, and the folded, bi-directional, and multi-channel systems. Design optimization solutions are also introduced in Section 3.3. A simplified version of OTIS has been successfully designed and tested for the OIU feasibility demonstration. In Section 3.4, experimental verification for a simple 64×64 channels OTIS is presented.

### 3.1 TRANSPOSE INTERCONNECTION

A transpose operation usually consists of symmetrically interchanging the elements of a 2-D array with respect to the first diagonal of that array. In this project, we propose to implement a particular transpose interconnection between two arbitrary planes where each row of the input and output arrays is arranged in a raster format within that array as shown in Figure 3-1. The transpose interconnection we describe is a one-to-one interconnection between  $L$  transmitters  $\{l_t\}$  and  $L$  receivers  $\{l_r\}$ , where  $l_t$  and  $l_r$  range from 0 to  $L-1$  and  $L$  is the product of two integers,  $M$  and  $N$ . Since  $L = M N$ , the indices  $l_t$  and  $l_r$  can be divided into ordered pairs  $(n_t, m_t)$  and  $(m_r, n_r)$  respectively, where  $m_t$  and  $m_r$  range from 0 to  $M-1$  and  $n_t$  and  $n_r$  range from 0 to  $N-1$ , such that:

$$l_t = M n_t + m_t ; l_r = N m_r + n_r$$

$$n_t = \text{trunc} ( l_t/M ) ; m_r = \text{trunc} ( l_r/N ) \quad (3-1)$$

$$m_t = l_t \text{ modulo } M ; n_r = l_r \text{ modulo } N$$

The indices  $n_t$  and  $m_r$  are referred to as the *major indices* of the transmitters and receivers, respectively,  $m_t$  and  $n_r$  are called the *minor indices*, and  $l_t$  and  $l_r$  are referred to as the *scalar indices*. In the transpose interconnection,  $(n_t, m_t)$  is connected to  $(m_r, n_r)$  if and only if  $m_t = m_r$  and  $n_t = n_r$ . Such an interconnection is called an  $M \times N$  transpose.

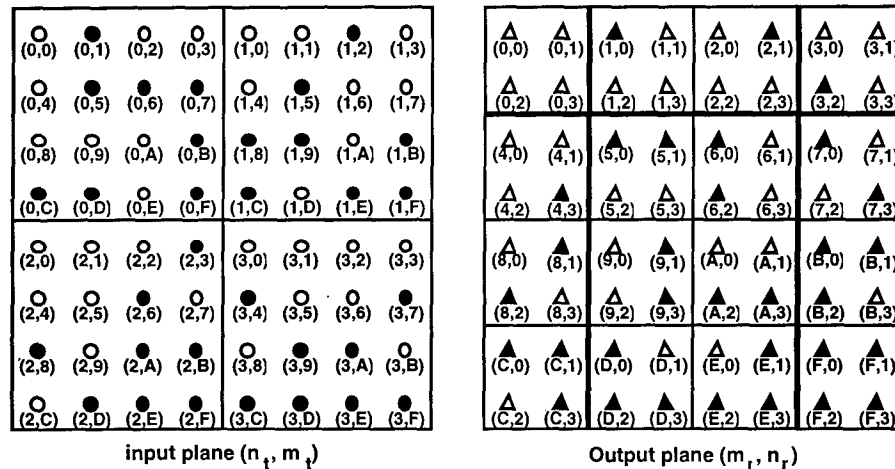


Figure 3-1. Input and output plane of a  $16 \times 4$  OTIS, showing major and minor index patterns as well as the transpose mapping of a typical signal pattern.

Figure 3-1 shows the physical layout of the transmitter and receiver planes of OTIS for  $M = 16$  and  $N = 4$ . Both planes are divided into regions in which the major index is constant. The *major pattern* of each plane indicates the location of each of these regions. The *minor pattern* indicates the location of the transmitters or receivers within a region. The major pattern of the transmitter plane is identical to the minor pattern of the receiver plane, except for a scaling factor  $\sqrt{M}$ . Likewise, the minor pattern of the transmitter plane is similar to the major pattern of the receiver plane, but is smaller by a factor  $\sqrt{N}$ . The particular order of indexing within a pattern will depend on the application architecture. However, the order of indexing within the major (minor) pattern of the transmitter plane must match the order of indexing within the minor (major) pattern of the receiver plane. The gray transmitters and receivers on Figure 3-1 show a pattern of signals mapped from the transmitter plane to the receiver plane via the transpose interconnection.

Figure 3-2 shows the side view of the OTIS optical system that connects the two planes described above; the top view would be similar. The major and minor indices are further divided into x and y components, so that the transmitters are indexed by  $(m_{ty}, m_{tx}, n_{ty}, n_{tx})$  and the

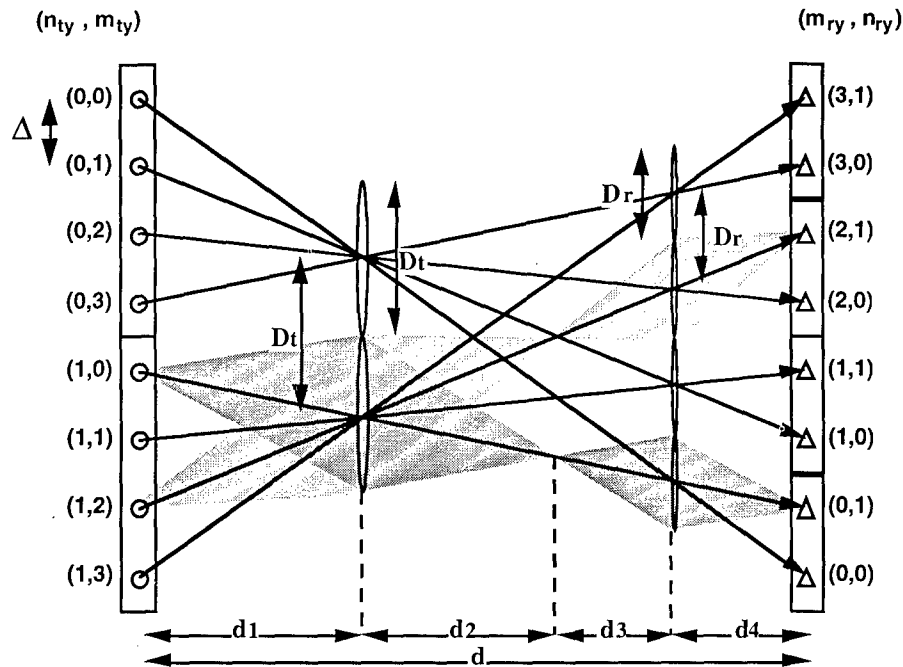


Figure 3-2. Side view of the OTIS showing imaging through coupled lenslets arrays.

receivers by  $(n_{ry}, n_{rx}, m_{ry}, m_{rx})$ . A  $\sqrt{N} \times \sqrt{N}$  array of lenslets is placed in front of the transmitter plane and a  $\sqrt{M} \times \sqrt{M}$  array of lenslets is located before the receiver plane.

The interconnection from transmitter  $(m_t, n_t)$  to receiver  $(n_r, m_r)$  is traced by the chief ray passing through the center of the transmitter lens  $m$  and the center of the receiver lens  $n$ . These two lenses comprise an imaging system between the transmitter and receiver planes. Note that the optical imaging system requires that the indexing in the receiver plane be rotated 180 degrees relative to the transmitter plane.

### 3.2 RELATION BETWEEN OTIS AND THE SHUFFLE EXCHANGE NETWORK

An important application of OTIS is in support of multistage interconnection network (MIN) architectures based on  $k$ -shuffles. A  $k$ -shuffle MIN functionally provides full connectivity between  $L$  input channels and  $L$  output channels in  $\log_k L$  stages of optoelectronic switch planes and  $(\log_k L) - 1$  stages of optical  $k$ -shuffles. One optoelectronic switch has  $k$  optical inputs (receivers) and  $k$  optical outputs (transmitters) and provides crossbar equivalent electronic switching between its  $k$  channels.

In a  $k$ -shuffle, the receiver  $l_r$  to which  $l_t$  is connected is given by

$$l_r = k \{l_t \text{ modulo } (L/k)\} + \text{trunc} (kl_t/L) \quad (3-2)$$



If  $M$  is set equal to  $L/k$  and  $N$  is set equal to  $k$ , then

$$l_r = N m_t + n_t \quad (3-3)$$

Equating Equations (3-2) with (3-3) for arbitrary values of  $l_t$  implies that  $n_t = n_r$  and  $m_t = m_r$ . Therefore, the  $k$ -shuffle is equivalent to a  $(L/k) \times k$  transpose. Note that an output switch in a  $k$ -shuffle OTIS-MIN corresponds to a major index region and that the number of major regions in the source plane is equal to  $k$ . An interesting application of OTIS-MIN arises when  $k = (M N)^{1/2}$  since the number of stages for routing becomes a constant:

$$\log_k L = \log_{\sqrt{MN}} MN = 2 \quad (3-4)$$

In this case, only two stages of optoelectronic switches and one stage of optics are required to perform full routing between source and destination planes, independent of the total number of communication channels in the MIN.

### 3.3 OTIS SYSTEM ANALYSIS

The analysis of the OTIS optical system is provided in this Section. The geometrical relations for the optical system are derived including lens positions, system length, and system volume. The light throughput efficiency and the insertion losses of the OTIS optical system are then analyzed. All these relations are derived for the basic OTIS optical system and extended to the generalized system for arbitrary optoelectronic chip layouts.

#### 3.3.1 Optical System Characterization and Derivations

In order to achieve the desired transformation the lenses must be separated by a distance  $D_t$  for the transmitter lenses and  $D_r$  for the receiver lenses (see Fig. (3-2)). Both  $D_t$  and  $D_r$  can be easily derived using simple geometric (similar triangles) relations:

$$\begin{aligned} D_t &= \left( \frac{\sqrt{MN} - 1}{\sqrt{N} + 1} \right) \Delta \\ D_r &= \left( \frac{\sqrt{MN} - 1}{\sqrt{M} + 1} \right) \Delta \end{aligned} \quad (3-5)$$

Note that the lens spacings  $D_t$  and  $D_r$  are also the clear apertures of the lenses above the transmitters and receivers planes respectively. The positions  $(x_i, y_j)$  of the center of the lenses in these planes are then given by:

$$(x_i; y_j) = \left[ \pm (1 + i) \left( \frac{\sqrt{MN} - 1}{\sqrt{N} + 1} \right) \frac{\Delta}{2}; \pm (1 + j) \left( \frac{\sqrt{MN} - 1}{\sqrt{N} + 1} \right) \frac{\Delta}{2} \right] \quad (3-6)$$

where  $i, j = 0, \dots, \sqrt{N}/2 - 1$ . In the case of a system as shown in Fig. (3-2), these would be the coordinates in the first lens (transmitter lenses) plane. Those for the second plane (receiver lenses) can be derived using Eq. (3-6) and replacing  $N$  with  $M$  and  $M$  with  $N$  respectively. It can also be

shown that the magnification of the transmitter lenses (X) must be the inverse of the magnification of the receiver lenses for an unit system magnification:

$$\frac{d_2}{d_1} = \frac{d_3}{d_4} = X = \frac{\sqrt{MN} - 1}{\sqrt{M} + \sqrt{N} + 2} \quad (3-7)$$

This leads to the following relation between the focal lengths  $f_t$  and  $f_r$  of the transmitter and receiver lenses respectively:

$$f_r = \frac{\sqrt{N} + 1}{\sqrt{M} + 1} f_t \quad (3-8)$$

By combining Eq. (3-5) and Eq. (3-8) it can be shown that the f-numbers ( $f_{\#}$ ) of the transmitter and receiver lenses have to be the same. It is then possible to derive the total length (d) of the system as a function of the system size (number of channels), the source spacing in the transmitter plane and the f-number of the lenses used in the system:

$$d = (\sqrt{N} + 1)(\sqrt{M} + 1) \Delta f_{\#} \quad (3-9)$$

The aspect ratio (AR) of the system can also be estimated. It is equal to the ratio of the system length to the transmitter (receiver) plane width:

$$AR = \left( 1 + \frac{1}{\sqrt{M}} + \frac{1}{\sqrt{N}} + \frac{1}{\sqrt{MN}} \right) f_{\#} \quad (3-10)$$

It is interesting to notice that the aspect ratio of the OTIS system is asymptotically equal to the f-number of the lenses of the system. Finally, the volume of the system can be approximated to:

$$V \approx (NM)^{3/2} \Delta^3 f_{\#} \quad (3-11)$$

These equations fully characterize the geometrical behavior of the OTIS optical system, assuring that the lenses perform the desired transformation. This optical system is advantageous in terms of complexity and alignment since only two planes of optical elements are required to interconnect two optoelectronic chips. Power considerations such as insertion losses, system efficiency and crosstalk are discussed in the next Section.

### 3.3.2 System Power Considerations

As can be seen in Fig. (3-2), the OTIS optical system does not achieve 100% light efficiency. This is because the light sources of one given *major pattern* in the transmitter plane do not illuminate only their dedicated lens. Some of the emitted light is lost on the edges of the chips where there is no transmitter lens and some other illuminates the neighboring transmitter lenses creating unwanted images (spots) in the receiver plane. However, it can be shown by ray tracing that these unwanted images are not a direct source of crosstalk<sup>(3-2)</sup> since they always lie outside the chip area in the receiver plane.

In the following, it is assumed that all transmitters in a given *major pattern* fully illuminate their dedicated lens and that the transmitters located at the edge of the transmitter plane do not over-illuminate their dedicated lens (Fig. 3-3). It is then possible to estimate the worst-case collection efficiency ( $\eta_{wc}$ ) of this lens system by calculating a simple area ratio.  $\eta_{wc}$  can be approximated by the ratio of the amount of light emitted by an edge transmitter and captured by its dedicated lens to the total area illuminated by this transmitter at the lens plane:

$$\eta_{wc} = \left( \frac{D_t}{3 D_t} \right)^2 = 11.1 \% \quad (3-12)$$

Another concern for such a system is the coupling light efficiency between the transmitter lens plane and the receiver lens plane. It turns out that in the OTIS system there will be no coupling losses (in first approximation). This is due to the design constraint that the f-numbers of the transmitter and receiver lenses have to be matched and that all the light transmitted by a transmitter lens will illuminate exactly the corresponding receiver lens. Therefore, if reflection losses and diffraction losses at the receiver lenses and at the detectors are neglected, the worst-case light efficiency (for an edge modulator) of the system will always be 11.1 %.

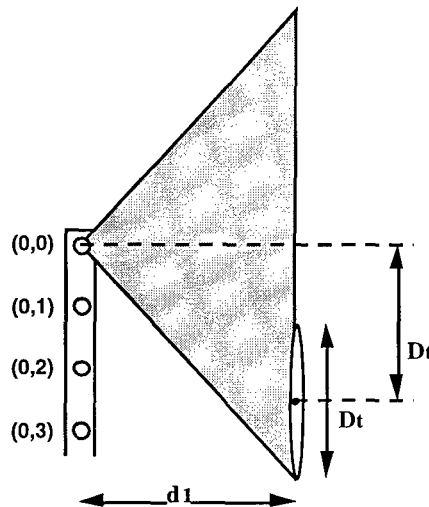


**Figure 3-3: Off-axis illumination and vignetting for a light transmitter located at the edge of the array**

The optical implementation of OTIS can be achieved with either refractive or diffractive optics. Utilization of diffractive optics in the system will decrease the light efficiency by a factor proportional to the number of phase levels used in the diffractive optics fabrication.<sup>(3-3)</sup> Furthermore, some of the incident light on the diffractive elements will diffract into higher order terms, thereby affecting the Signal-to-Noise Ratio (SNR) of the system. However, these effects will not be developed under this program since they have already been studied elsewhere.<sup>(3-4,3-5)</sup>

### 3.3.3 Generalized System

The OTIS optical system described in the previous sections assumes that the transmitters and the receivers on the optoelectronic integrated circuits lay on a regular square grid and that all the nodes of that grid are used. In practice, due to the electronic layout, it could prove useful for the optical system to be able to accommodate optoelectronic chips with different arrangements.

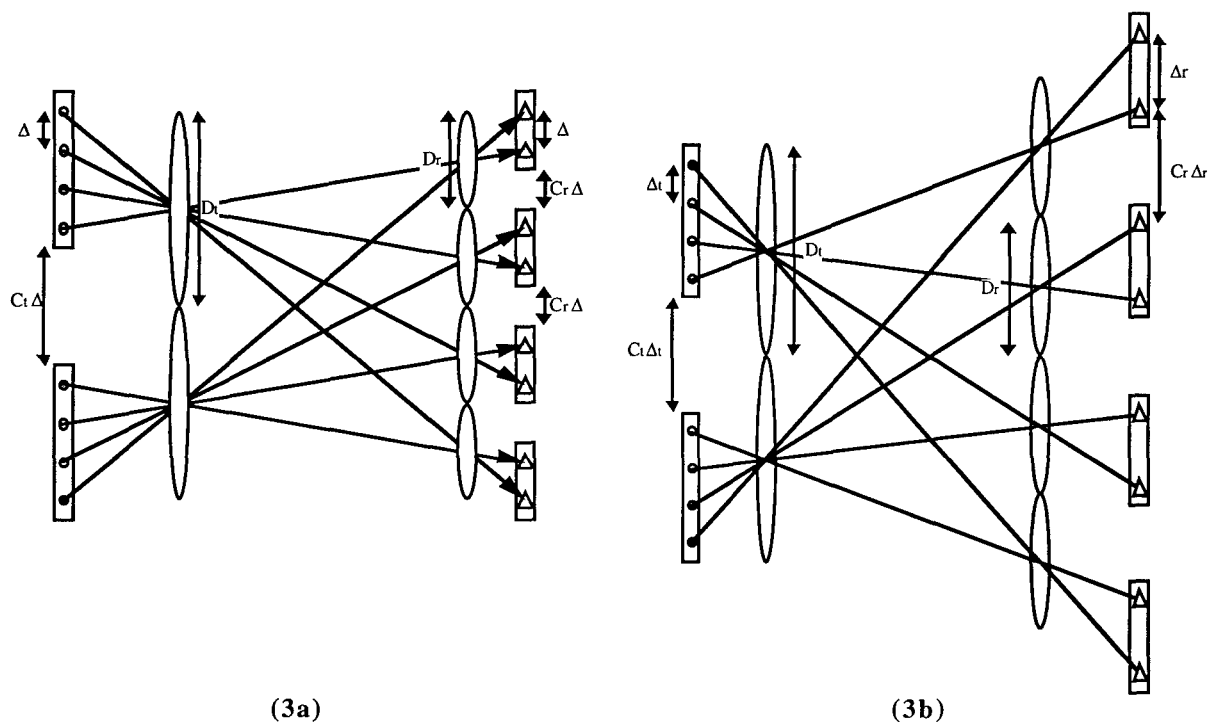


Figure 3-4. OTIS system for accommodating arbitrary optoelectronic layouts.

Figure 3-4a shows one possible case where there is a gap between the *major patterns* in both the transmitter ( $C_t$ ) and receiver ( $C_r$ ) planes. These gaps can be used for wiring electrical inputs and outputs on and off the chips, for bringing power lines to the different locations on the chips, or to accommodate the fact that the optoelectronic transmitter and receiver planes are built using multi-chip module technology. An addition to that case is shown in Fig. 3-4b where the spacing between nodes in the transmitter plane ( $\Delta_t$ ) is different from the spacing between nodes in the receiver plane ( $\Delta_r$ ). As in the previous section, it can be shown that the spacing between the transmitter lenses ( $D_t$ ) and the receiver lenses ( $D_r$ ) is:

$$D_t = \frac{[(\sqrt{M} + C_t)(\sqrt{N} + C_r) - 1]}{1 + \frac{\Delta_r}{\Delta_t}(\sqrt{N} + C_r)} \Delta_r \quad (3-13)$$

$$D_r = \frac{[(\sqrt{M} + C_t)(\sqrt{N} + C_r) - 1]}{\frac{\Delta_r}{\Delta_t} + (\sqrt{M} + C_t)} \Delta_r$$

Calculations similar as in the previous section lead to the following relation between the f-numbers of the transmitter lenses ( $f_{\#t}$ ) and the receiver lenses ( $f_{\#r}$ ):

$$\frac{f_{\#t}}{f_{\#r}} = \frac{(\sqrt{M} + C_t + 1) \left[ 1 + \frac{\Delta_r}{\Delta_t} (\sqrt{N} + C_r) \right]}{(\sqrt{N} + C_r + 1) \left[ \sqrt{M} + C_t + \frac{\Delta_r}{\Delta_t} \right]} \quad (3-14)$$

It is interesting to note that the f-numbers of both lens planes will be different only when the node spacing in the transmitter and receiver planes is different ( $\Delta_t \neq \Delta_r$ ). However, the overall magnification of the generalized system can be shown to be still 1 while the magnification of the first lenslet array (X) is:

$$X = \frac{d_2}{d_1} = \frac{d_3}{d_4} = \frac{\frac{\Delta_r}{\Delta_t} [(\sqrt{M} + C_t)(\sqrt{N} + C_r) - 1]}{\left[ \frac{\Delta_r}{\Delta_t} + \sqrt{M} + C_t \right] \left[ \frac{\Delta_r}{\Delta_t} (\sqrt{N} + C_r) + 1 \right]} \quad (3-15)$$

The length of the system can be derived from Eq. (3-13), Eq. (3-14), and Eq. (3-15), as a function of  $f_{\#t}$  or  $f_{\#r}$ :

$$d = (\sqrt{M} + C_t + 1) \left[ 1 + \frac{\Delta_r}{\Delta_t} (\sqrt{N} + C_r) \right] \Delta_t f_{\#t} \quad \text{or} \quad (3-16)$$

$$d = (\sqrt{N} + C_r + 1) \left[ \sqrt{M} + C_t + \frac{\Delta_r}{\Delta_t} \right] \Delta_t f_{\#r}$$

if  $\Delta_t = \Delta_r$ , the two relations in Eq. (3-14) are identical since the f-numbers are equal. It can be shown that the volume of the system still grows linearly with the number of channels in the system and the node spacing:

$$V \propto (NM)^{\frac{3}{2}} \Delta_t^3 f_{\#t} \quad (3-17)$$

The last metric of interest is the light collection efficiency as introduced in the previous section. It can be shown that the worst-case efficiency for the generalized system is:

$$\eta_{wc} = \left\{ 1 + \frac{\left[ (\sqrt{N} - 1) \left( \sqrt{M} + C_t + \frac{\Delta_r}{\Delta_t} \right) \right] + \left[ (\sqrt{M} - 1) \left( \frac{\Delta_r}{\Delta_t} (\sqrt{N} + C_r) + 1 \right) \right]}{\frac{\Delta_r}{\Delta_t} [ (\sqrt{M} + C_t) (\sqrt{N} + C_r) - 1 ]} \right\}^{-2} \quad (3-18)$$

By simply trading in chip area (increased receiver spacing or “gaps” between *major patterns*), the light collection efficiency of the system can be improved.

In the following sections, in order to simplify without loss of generality, M and N will be set equal (symmetrical system) and the product  $L = M^2 = N^2$  will be assumed to be a power of 4. Note that this type of system is particularly useful in the case of k-shuffle applications with  $k = M = N$ . In this case, the number of stages for routing or sorting of the k-shuffle multistage interconnection network becomes a constant independent of L ( $L = MN$  is the size or number of channels of the network). For routing applications, only 2 electronic switching stages and one optical interconnection stage will be required to achieve full connectivity for any L.

### 3.3.4 Folded System

The previously described systems perform the transpose interconnection but leave the transposed result on a different array than the original one. In some cases, it can be desirable to have both the original matrix and its transpose on the same array. Figure (3-5) shows a possible optical system that achieves the matrix transposition on a single optoelectronic chip. The light emitted by the transmitters is first imaged through the OTIS lenses onto an intermediate image plane shown by a dashed line on Fig. (3-5). A single imaging lens and a folding mirror are then used in a one-to-one, 4f configuration to flip this intermediate image back onto itself. Finally, the light goes through the OTIS lenses again to the detectors on the chip in order to complete the transpose operation.

The interconnection function achieved in this case is exactly that of a matrix transpose operation without any image inversion or rotation, leaving the elements of the first diagonal of the matrix unchanged and interchanging all the other elements of that matrix with respect to the first diagonal. It is important to note that only symmetrical systems ( $N = M$ ) can be folded in this manner. It can be seen on Fig. (3-5) that the apertures of the OTIS lenses in the folded configuration are no longer symmetrical with respect to their center and that the area between the lenses is actually used to block the incident or reflected light. This is required to achieve the transpose interconnection operation without any crosstalk between adjacent communication channels. The size of these beam blocks (bb) can be easily calculated and reduces to  $bb = X \delta$ , where X is the magnification of the

OTIS transmitter lenses and  $\delta$  is the spacing between modulators and detectors on the transmitter/receiver plane.

This configuration reduces the light collection efficiency and the light coupling efficiency of the system since the effective apertures of the OTIS lenses are reduced and light is blocked on both the forward path from the transmitters to the mirror and the reflected path from the mirror to the receivers. In this case the worst-case light efficiency of the system (Eq. (3-12)) reduces to:

$$\eta_{wc} = \left( \frac{D_t - 2 \text{ bb}}{3 D_t + \delta} \right)^2 \quad (3-19)$$

where  $D_t$  is the spacing between the centers of adjacent lenses. In order to minimize light losses in such a folded system, the receivers and transmitters should be laid out as close possible from each other on the optoelectronic chip; i.e.  $\delta$  should be as small as physically possible compared to  $\Delta_t$ .

For multistage interconnection network applications, the folded configuration only uses a single optoelectronic plane and a single optical interconnection plane, thereby reducing the amount of hardware in the system. However, such issues as buffering, time-multiplexing, and pipe lining of the data become of importance and must be evaluated<sup>(3-6)</sup> before a single chip implementation can be envisaged.

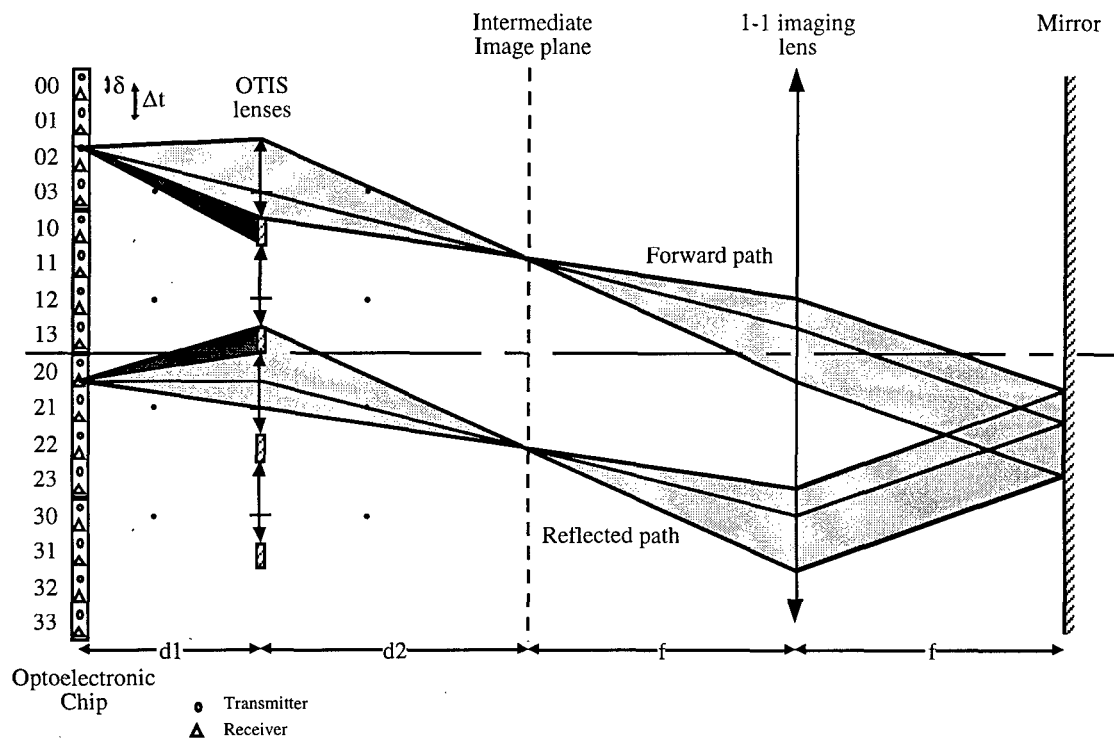


Figure 3-5. Folded (reflective) OTIS configuration.

### 3.3.5 Bi-directional system

An important feature of the Optical Transpose Interconnection System described in the previous sections is that it can be made bi-directional easily. This could prove useful in a number of applications. For interconnection networks in a packet switching configuration it allows blocking information to be sent back to the previous stages of the network in order to establish the correct routing path in the network. OTIS can also be used in a matrix-vector multiplier configuration (OTIS-MT) in support of neural network applications. In this case, the bi-directionality characteristic of OTIS can be used to implement an on-chip fully parallel back propagation learning system.

The implementation of the bi-directional OTIS optical system is shown on Fig. (3-6). Plane 1 and Plane 2 are now both transmitter/receiver planes. Plane 2 is actually rotated  $180^\circ$  with respect to plane 1 so that a transmitter on plane 1 faces a receiver on plane 2 and vice-versa. Similarities with the folded system from Fig. (3-5) can be observed in the fact that beam blocks between adjacent lenses are required in order to avoid crosstalk. These beam blocks are located on the lower half of the transmitter lenses and the upper half of the receiver lenses. As it was described in the previous section, the light collection efficiency and the light coupling efficiency are reduced. It can be proven that the beam blocks in this case are the same size as in the bi-directional system case and therefore, the worst-case light efficiency of the system is also given by Eq. (3-19).

### 3.3.6 Multi-channel System

A final interesting feature of the OTIS system is that it can become a multi-channel system where each node has more than a single pair of transmitter/receiver. This is useful in the case where more than bit serial communication is required in a system. For example, it could be required to have word parallel communication where each word would have 16 bits. In this case, each node would have  $4 \times 4$  transmitter/receiver pairs. It could also be useful in the case of interconnection networks where one transmitter/receiver pair would be used for data communication and one other for activation/blocking information. In this case, 2 transmitter/receiver pairs are required within each node. Finally, it could also prove useful to have 2 transmitter/receiver pair for each communication channel in order to implement differential readout (dual-rail logic) in the case where the intrinsic signal-to-noise ratio of the system is not sufficient to provide low communication bit error rates.



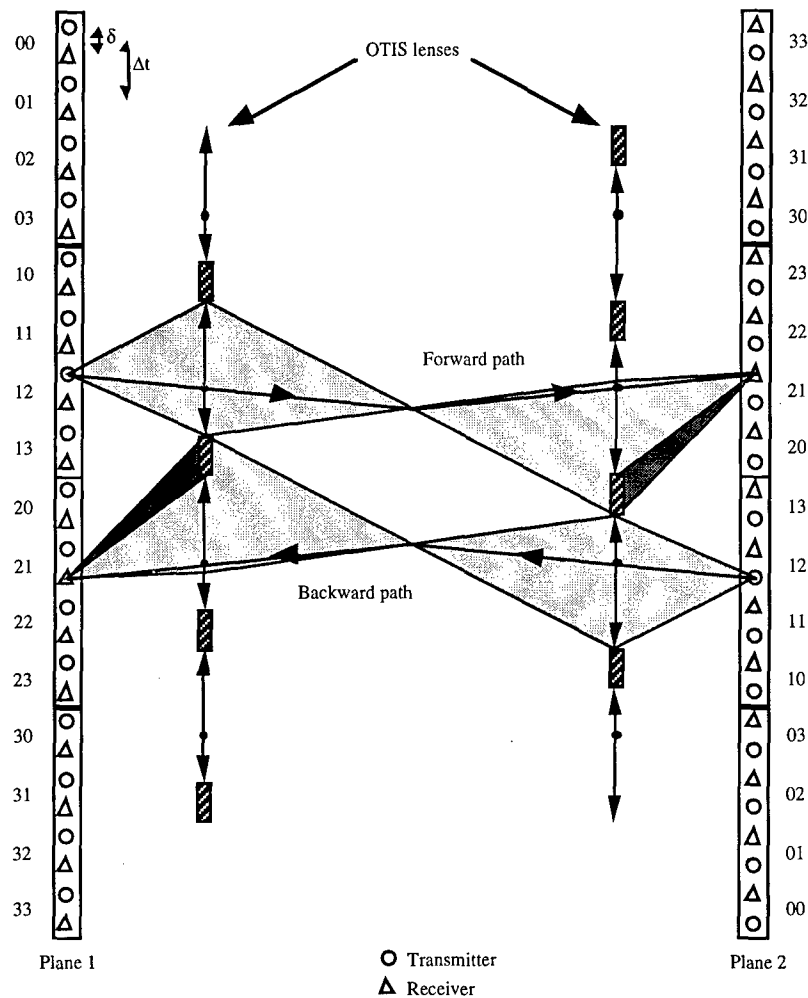


Figure 3-6: Bi-directional OTIS

Figure 3-7 shows a 1-D representation of a multi-channel system with 2x2 transmitter/receiver pairs within each node. As before, plane 2 is actually rotated 180° with respect to plane 1 so that a transmitter on plane 1 faces a receiver on plane 2 and vice-versa (Note that the multi-channel system is also bi-directional). In this case, beam blocks are also required around the lenses to achieve the transpose interconnection without any crosstalk. The size of these beam blocks can be easily derived and reduces to:

$$bb = X ( 2 K - c ) \delta \quad (3-20)$$

where  $X$  is the magnification of the transmitter lenses,  $K$  is the number of transmitter/receiver pairs within each node,  $\delta$  is the spacing between adjacent transmitter and receiver and  $c$  is a constant that can take two different values (see below). Two different beam blocks of different sizes located at the top and the bottom of the OTIS lenses are needed. Which beam block is used at the top or

bottom of the lenses will change from the plane 1 lenses to the plane 2 lenses (see Fig. 3-7). For the plane 1 lenses (on the left on Fig. 3-7),  $bb$  can be calculated with  $c = 1$  for the beam blocks at the top of each lens and  $c = 3$  for those at the bottom. In the second lens plane the beam block positions will be inverted for the same values of  $c$ . In this configuration, the light efficiency of the system is also reduced and it can be calculated to be:

$$\eta_{wc} = \left[ \frac{D_t - 2 bb_1 - bb_2}{3 D_t + (2 K - 1) \delta} \right]^2 \quad (3-21)$$

As previously, it can be seen that it is important to have the transmitters and detectors located toward the centers of each node (minimize all the terms of Eq. (3-21) except  $D_t$ ) in order to optimize (maximize) the worst-case light efficiency of the system.

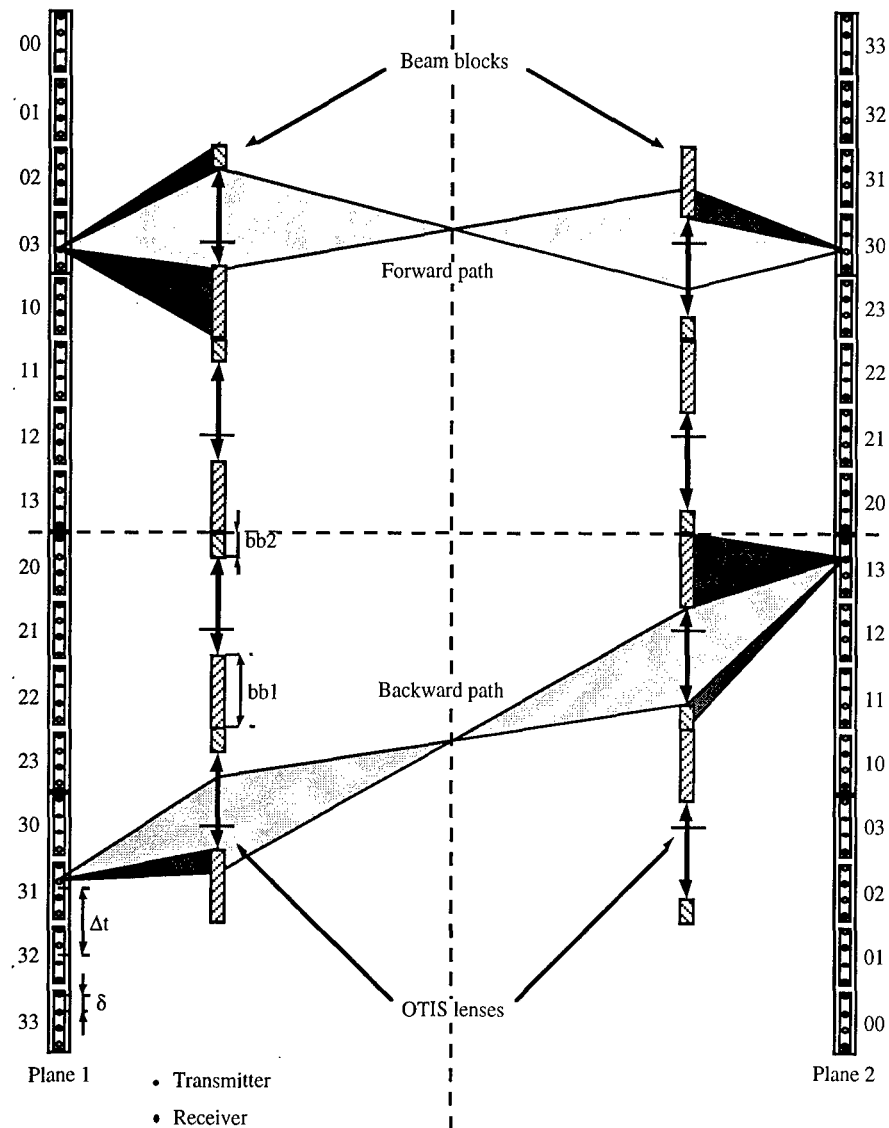


Figure 3-7. Multi-channel OTIS implementation.

### 3.3.7 OTIS Issues

The analysis of the OTIS system raises some important issues. First, the insertion losses are too high and must be reduced. Second, the use of a Polarizing Beam Splitter (PBS) will create problems in terms of uniformity and crosstalk.

#### 3.3.7.1 Array Illuminator

As shown in Section 3.3.2, the collection efficiency of the system can be as low as 10%. This is not acceptable and improvements have to be made. A possible improvement is shown in Fig. 3-8 where all the modulators in the system are illuminated at the correct angle so that all the light that passes through a modulator will be collected by the right OTIS lens. Such issues as the effect of non-normal incidence on the modulators, crosstalk and others has been studied and reported in the final report. Note that this system is also ideally suited for implementation with the Binary Computer Generated Hologram (BCGH) technology for reflective type modulators.

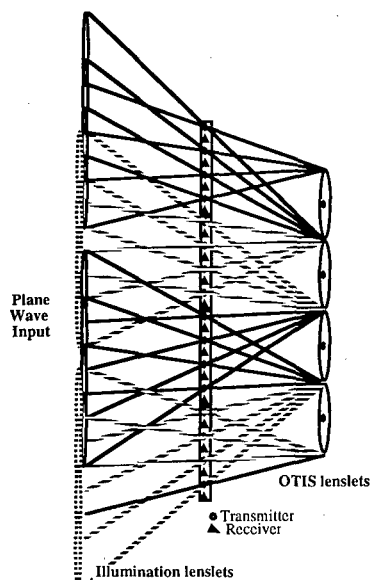


Figure 3-8. Area multiplexed illumination lenslets for the OTIS.

#### 3.3.7.2 Beamsplitter

Another problem in the optical system design is that a PBS is used for separating the modulator illumination path from the interconnect path. In the interconnect path, this will create some crosstalk and efficiency problems since the acceptance angle of a PBS is very limited ( $\pm 5^\circ$  at best even for a narrow band PBS). Therefore we have investigated alternative solutions: wire-grid polarizers and volume holograms.

A wire-grid polarizer could be considered as a replacement for the polarizing beamsplitter in the optical interconnection module. The role of the wire-grid polarizer in such a module would be to

bring the linearly polarized illumination beam (at a certain direction) to the light modulators, yet not interrupting the interconnection path. This may be accomplished by the nature of the wire-grid polarizer that it is virtually transparent to the orthogonally polarized light. To determine if a wire-grid polarizer is suitable for such a use, its transmission and polarization characteristics, especially the off-axis ones, should be examined. The analysis given below follows directly from a generalized model for wire-grid polarizers introduced by Yeh<sup>(3-7)</sup>: a wire-grid polarizer consists of parallel wires which reflects one polarization of incident electromagnetic radiation while transmitting the other, provided the period of the grid is smaller than the wavelength of the radiation.

In the generalized optical model developed by Yeh, a wire-grid polarizer is considered as a thin sheet of composite medium consisting of parallel slabs (or cylinders) of absorbing material (e.g., metal) immersed in an isotropic base medium. If the dimension of the wires and the spacing between them are sufficiently small compared to the wavelength of the electromagnetic radiation, the whole structure behaves like a homogeneous and uniaxially anisotropic medium. If the indices of refraction of the absorbing medium (wire) and the base medium are  $n_a$  and  $n_b$ , respectively, then the effective indices of the composite structure consisting of parallel slabs are given by (3-8)

$$\begin{aligned} n_{||}^2 &= v_a n_a^2 + v_b n_b^2, \\ n_{\perp}^2 &= n_b^2 + \frac{v_a (n_a^2 - n_b^2)}{1 + v_b (n_a^2 - n_b^2) / n_b^2} \end{aligned} \quad (3-22)$$

where  $v_a$  is the fraction of volume occupied by the absorbing medium and  $v_b = 1 - v_a$ . These equations are known as Weiner's equation of form birefringence.

A wire-grid polarizer made of good conductor behaves as a good conducting metal layer with an effective index of refraction  $n_{||}$  for incident radiation with electric field vector parallel to the wire grids and reflects most of the incident radiation if the layer is thick enough. For incident radiation with electric field vector perpendicular to the wire grids, the polarizer behaves as a dielectric layer and reflects no light provided the polarizer is properly anti-reflection coated. This assumption is true for the extreme case when the wire grids are made of perfect conductors and the base medium is pure dielectric, in which case the refractive indices given by Equation (3-22) become:

$$\begin{aligned} n_{||} &= \sqrt{v_a} n_a \\ n_{\perp} &= \sqrt{(v_a + v_b) / v_b} n_b, \end{aligned} \quad (3-23)$$

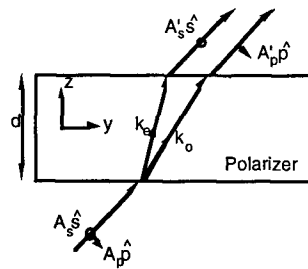
since  $\ln_a^2 \gg n_b^2$ . The condition  $\ln_a^2 \gg n_b^2$  is true for metals such as aluminum, silver, etc. in the infrared spectral regime. At  $\lambda = 10 \mu\text{m}$ ,  $\ln_a^2 = 5200$  and  $4800$  for aluminum and silver, respectively.<sup>(3-9)</sup> Therefore, if both modes are excited at the input face of the polarizer, the incident

radiation with electric field vector parallel to the wire grids sees a complex refractive index of  $n_{||}$  with a large imaginary part and is attenuated strongly, while the radiation with electric field vector perpendicular to the wire grids sees a real refractive index of  $n_{\perp}$  and propagates freely in the polarizer.

However, this is not completely true in the visible spectral regime. At  $\lambda = 0.55 \mu\text{m}$ ,  $|\text{Im} n_a^2| = 36$  and  $10$  for aluminum and silver, respectively. Hence,  $n_{\perp}$  is not a real number but has a complex part as given by Eq. (3-22). Therefore the radiation with electric field vector perpendicular to the wire grids does not propagate freely but experience attenuation. On the other hand,  $n_{||}$  does not have a very large imaginary part anymore and the radiation with electric field vector parallel to the wire grids is not attenuated strongly. These conditions may have severe effects on the transmission and polarization characteristics of the wire-grid polarizer in the visible spectral regime. The polarization selectivity can be increased by increasing the volume of the metallic layer. This, however, decreases transmission.

To have an idea about the polarization characteristics, we can consider the wire-grid polarizers developed by Texas Instruments, Inc.<sup>(3-10)</sup> by vacuum evaporation technique. Their low density polarizer had a degree of polarization of about  $0.88$  and transmission of  $0.40$  at  $0.8 \mu\text{m}$ . A higher density one had a degree of polarization of  $0.99$  and transmission of  $0.23$  at  $0.85 \mu\text{m}$ . The performances were much poorer at  $0.5 \mu\text{m}$ . In addition, these were the normal incident radiation characteristics.

To determine the polarization properties of a wire-grid polarizer in the case of off-axis incident radiation, it is sufficient to consider the relation between the fields incident on a thin uniaxially anisotropic medium and the fields transmitted through it. Consider the figure below:



Transmission of light through a uniaxial plate at off-axis incidence can be written in the matrix form, ignoring the multiple reflections in the plate, as :

$$\begin{bmatrix} A'_s \\ A'_p \end{bmatrix} = \begin{bmatrix} t_{os} & t_{es} \\ t_{op} & t_{ep} \end{bmatrix} \begin{bmatrix} e^{-ik_{oz}d} & 0 \\ 0 & e^{-ik_{ez}d} \end{bmatrix} \begin{bmatrix} t_{so} & t_{po} \\ t_{se} & t_{pe} \end{bmatrix} \begin{bmatrix} A_s \\ A_p \end{bmatrix} \quad (3-24)$$

where  $t_{so}$ ,  $t_{po}$ ,  $t_{se}$ ,  $t_{pe}$ ,  $t_{os}$ ,  $t_{es}$ ,  $t_{op}$ ,  $t_{ep}$  are the transmission coefficients,  $k_{oz}$  and  $k_{ez}$  are the  $z$  components of the wave vectors  $k_o$  and  $k_e$ , respectively. This expression relates the transmitted wave amplitudes  $A_s'$  and  $A_p'$  to the incident waves  $A_s$  and  $A_p$ . The definitions for the transmission coefficients and the wave vectors have been omitted here, and can be found in Yeh. However, it can be easily seen that the expressions for  $A_s'$  and  $A_p'$  will have both  $A_s$  and  $A_p$  terms. In other words, even if one of the orthogonal polarization components of the incident radiation is zero, at the output both of the orthogonal polarization components will be excited. This concludes that a wire-grid polarizer does not provide an advantage over a beamsplitter cube when the angular field properties are considered.

Since wire-grid polarizers do not offer significant advantages over PBSs, we are now investigating the possibility of using a volume hologram (and their Bragg selectivity properties) to differentiate between the illumination and interconnect optical paths, as depicted in Figure 3-4. The volume hologram is recorded by interfering two orthogonal plane waves in the holographic material. When readout by a plane wave (power in), the grating couples the light into another plane wave (illumination) which is used by the illumination lenslet array to create a spot array on the modulators. When the light is reflected by the modulators it hits the OTIS lenslets. Due to the topology of the OTIS interconnect, no significant plane wave component is created in the interconnection path and therefore all the light is coupled to the other OTIS lenslet array and focused down onto the detectors.

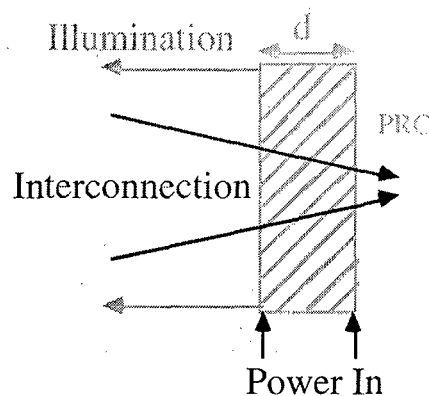


Figure 3-9. Volume holographic beamsplitter for the OTIS.

Since a single hologram is recorded in the holographic medium, it can have very high efficiency. Also, the hologram can be fixed off-line (using for example thermal fixing in  $\text{LiNO}_3$ ) and then used in the system. Such issues as recording uniformity, crosstalk, packaging, optimal thickness, optimal holographic material, and others have been studied and shown favorable responses.

### 3.4 OTIS DESIGN VERIFICATION

To demonstrate the OTIS concept an experimental system has been designed by implementing a one stage  $64 \times 64$  ( $N \times M$ ) symmetrical ( $N = M$ ) OTIS optical system. The system consists of a  $64 \times 64$  pinhole array (the input plane) and its associated illumination lenslet array, two refractive lenslet arrays for the interconnection, and a CCD camera as the output plane detector (shown in Figure 3-10).

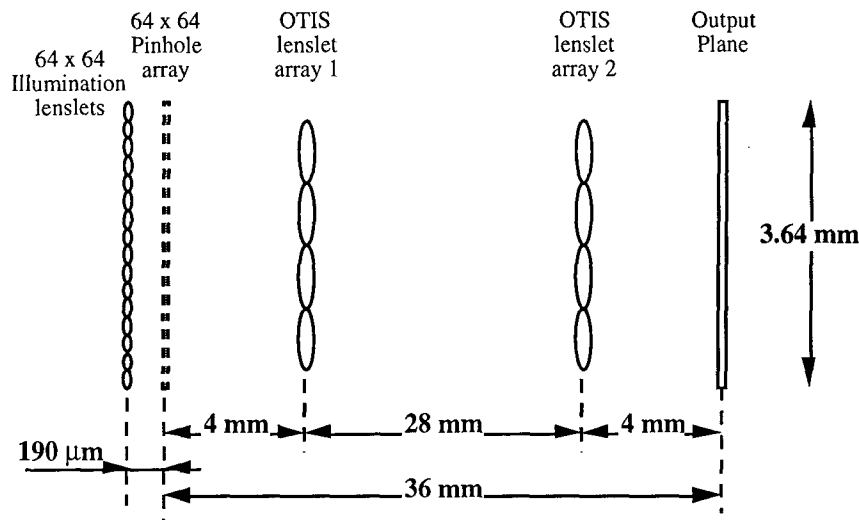
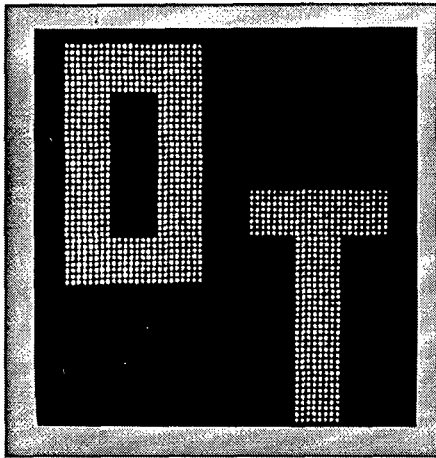
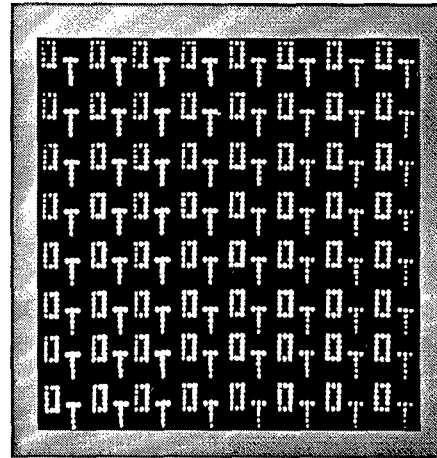


Figure 3-10. Experimental setup for the  $64 \times 64$  OTIS demonstration.

The  $64 \times 64$  pinhole array was fabricated using our electron beam lithography system. The pinholes were obtained via chrome-etch on a glass plate and have a  $5 \times 5 \mu\text{m}$  square aperture. They are spaced  $57 \mu\text{m}$  apart for a total input plane size of  $3.64 \text{ mm}$ . As illustrated in Figure 3-11, the pattern formed by the input pinholes represents the letters **OT**. The illumination lenslets have a  $190 \mu\text{m}$  focal length with an aperture of  $57 \mu\text{m}$  ( $f/\# \approx 3.3$ ) that matches the pinhole spacing and array format. The illumination lenslets were also fabricated using electron beam lithography system, exhibiting a minimum feature size of  $1.87 \mu\text{m}$ . However, since power was not an issue in this experiment, the lenses are kept as binary amplitude elements with a simple fabrication step of chrome-etch on glass. If light efficiency was critical, the lenses could easily be fabricated as multi-level phase elements. The interconnection lenslet arrays were purchased from Adaptive Optics Associates and they were fabricated in stamped epoxy on a glass microscope slide. The lenslet array size is  $20 \times 32$  and each lenslet has a  $399 \mu\text{m}$  aperture for a focal length of  $3.12 \text{ mm}$ , leading to a  $f/\#$  of approximately 8. As expected, the system achieves a one to one imaging transformation and the output plane pattern (see Figure 3-11) consists of the **OT** letters reduced in size by a factor of  $8 \left( \sqrt{N} \right)$  and replicated  $8 \times 8$  times over the output plane. An optimized design of this experimental system is currently under investigation. The optimization will be based on aspheric diffractive optical elements by using Code V<sup>(3-11)</sup> optical system design software.



Input Plane



Output Plane

Figure 3-11. Experimental results for a 64×64 OTIS interconnection.



## Section 4

# SPACE-TIME COMPANDER

The addition of an optical interconnect to the parallel locally-connected computer architecture allows an efficient optical image processing and global 2-D operations. The Space-Time Compander (STC) provides a parallel, bi-directional communication between coarse-grain processor arrays and fine-grain subsystems, such as optical memories, sensors, or optical co-processors. This parallel interface must allow data to either "expand" or be "compacted" in its spatial size: from the large fine-grain array size to the smaller coarse-grain processor array size. The most straight forward approach is to have a buffer array to convert the 2-D spatial (parallel) information into 1-D time (serial) information. The concept of space-time compander is illustrated in Figure 4-1.

The buffer array structure can be accomplished by the use of the charge coupled device (CCD) technology. This is based on the fact that the CCD technology can provide all three functions needed for such buffer structure namely, (1) time-sequential serial charge or voltage pattern

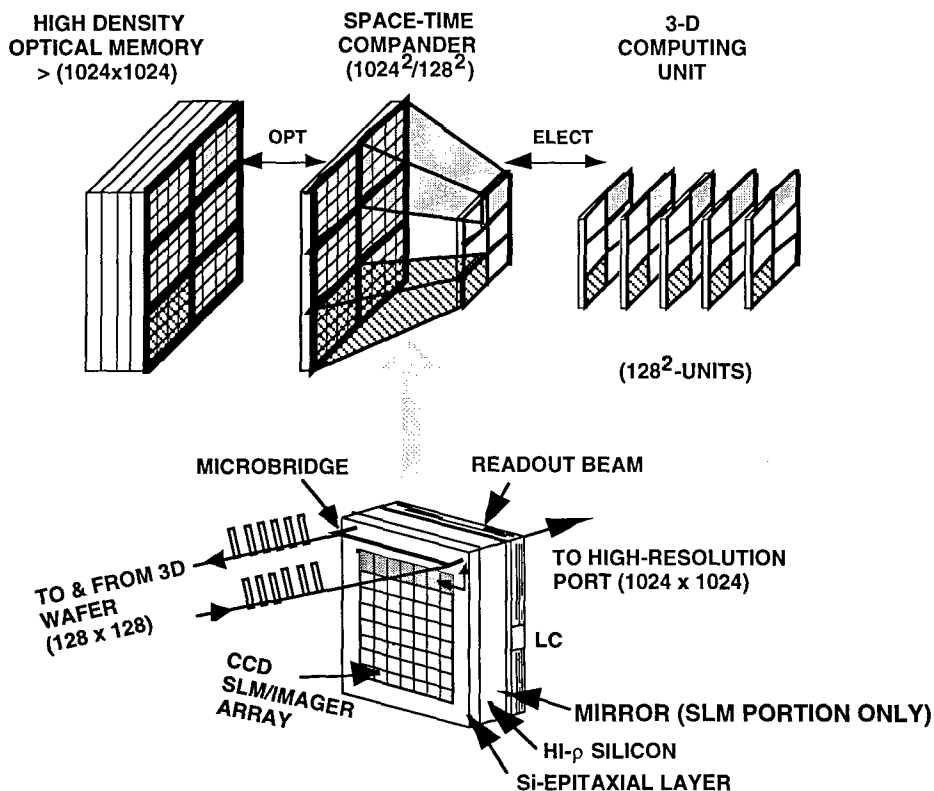


Figure 4-1. Schematic of space-time compander interface.

buffering, (2) imager technology, and (3) spatial light modulator driver technology.<sup>(4-1,4-2)</sup> Section 4.1 describes the design of modifying the Hughes CCD-LCLV and the associated optical systems for the STC application. In Section 4.2, a detailed CCD design analysis for the CCD-based STC is discussed.

#### 4.1 CCD-BASED LIQUID CRYSTAL IMAGER/MODULATOR

To efficiently communicate between a coarse-grain  $128 \times 128$  parallel processors and a fine-grain ( $1024 \times 1024$ ) optical information, the STC is designed to buffer each  $8 \times 8$  array of the  $1024 \times 1024$  port in a superpixel. The superpixel size was determined ( $448 \mu\text{m}$ ) in an attempt to match the size of Hughes 3-D computer module. The first design issue is the use of a *combined, dual purposes* modulator/detector array versus *separate* modulator and detector arrays in each superpixel (as schematically illustrated in Fig. 4-2). The main advantage of the combined approach is a simple optical system, while its main disadvantage is the comprised

performance of both detector and modulator arrays. On the other hand, the separate approach suffers a complicated optical system, but the imager and modulator can be individually designed and tuned for their optimum performance. This design flexibility is necessary only if we plan to deal with analog data with a large gray scale. For binary data the combined modulator/detector approach is preferred for the minimum optical system complexity associated. For a given physical 2-D size of the STC superpixel the combined modulator/detector approach also provides a larger pixel size and thus a better modulation transfer function (MTF). To squeeze two  $8 \times 8$  CCD arrays and two microbridges in a  $448 \mu\text{m}$  super-pixel, the CCD pixel size must be highly reduced and may not be able to support a 50% MTF in the conventional CCD-LCLV. Extensive research efforts

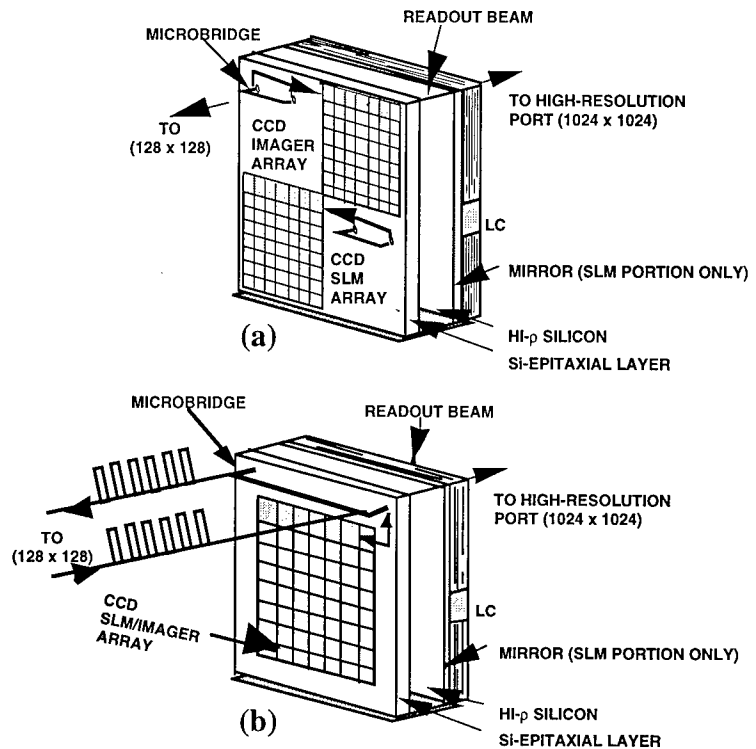


Figure 4-2. Schematics of one superpixel of the space-time compander: (a) separate modulator and detector arrays and (b) combined modulator/detector array.

will then be required to push for the resolution improvement. The design for the combined modulator/ imager approach is described next.

#### **4.1.1 CCD-LCLV Based Space-Time Compander**

Analysis shows that we can obtain a combined modulator/detector device with a slight modification of the current Hughes CCD-LCLV structure. By replacing the 5  $\mu\text{m}$  epilayer currently used on the p-Si substrate for the fabrication of the CCD gate structures with a thin (about 0.2  $\mu\text{m}$ ) p-type sheet implant layer and using a leaky mirror, the CCD-LCLV can also be used as an aerial imager. For this purpose, however, the combined device has to be operated at two different wavelengths for writing into and reading from the high resolution optical element (e.g., optical memory, etc.). In the write-in phase, the optical beam is reflected from the device and is modulated by the two-dimensional charge pattern information in the CCD array for addressing the high resolution element, while in the readout phase, the optical information from the high resolution element is transmitted through a specially designed leaky mirror resulting in a two dimensional charge pattern which is then read by the CCD array. To obtain high resolution in the imager it is necessary to deplete the entire Si substrate. The use of the thin p-type implanted layer allows the depletion of the entire Si substrate by the CCD gate voltage that would not be otherwise possible with the currently used p-type epilayer.

One of the important issues in developing the CCD-LCLV based STC involves device packaging. To directly communicate with processors, it is necessary to make electrically contact from the each of STC superpixels to the corresponding node on the processor array. A simple approach is to treat the CCD-LCLV as a single 3-D wafer, thus it can communicate with the 3-D computer through the microbridges or metal bump technologies. This approach is simple for implementation, but it lacks a precise control in the thickness uniformity of liquid crystal layer. Although this approach may suffer the nonuniformity of output light modulation, it is well suited for binary data modulation. On the other hand, since both CCD-LCLV and the parallel processor array (through D/A converters) are capable of dealing analog signal, it may be beneficial to push for analog devices. For this purpose it will be necessary to control the flatness of the CCD-LCLV by improving the device packaging techniques.

An optically flat Si substrate is required in the CCD-LCLV in order to obtain a uniform liquid crystal layer and hence a uniform output light intensity. Currently the Si substrate in the CCD-LCLV is flattened using our transfer bonding technique<sup>(4-3)</sup> in which the Si wafer is first contact bonded temporarily to an optically flat glass and the exposed side of the Si wafer is then epoxy bonded to a supporting glass substrate. After curing the epoxy, the temporary optical flat is then removed and a Si surface as flat as the optical flat is exposed. Consequently, any nonuniformity in the thickness of the Si substrate is embedded in the epoxy.

Electrical contact can be accomplished by using a glass substrate with conductive feedthroughs in which an array of holes is first made in the glass and then filled with a silver fret glass. The silver fret is initially in a paste form and mechanically pushed through the holes. It is then fired at about 300°C to form a solid conductive glass feedthrough. The holes in quartz substrate can be made by laser drilling using a high power CO<sub>2</sub> laser. Holes as small as 8-10 mils in diameter, which are within the predetermined 448  $\mu\text{m}$  superpixel size, can be made using this technique. It is also possible to use fiber optic capillary arrays to form necessary through-substrate holes.

The conductive feedthroughs in the supporting glass substrate can be electrically connected to the contact pads on the CCD circuit by using the indium bump or flip-chip bonding technique. An array of Indium bumps of about 1 mil in size with a periodicity of 448  $\mu\text{m}$ , corresponding to the unit supercell size in the 3-D computer, can be evaporated on both the CCD contact pads and the conductive feedthroughs using a shadow mask before the transfer bonding process. The design concept of the feedthrough packaging is illustrated in Figure 4-3. Again, this approach is not critically needed if the binary operation is adapted in the system.

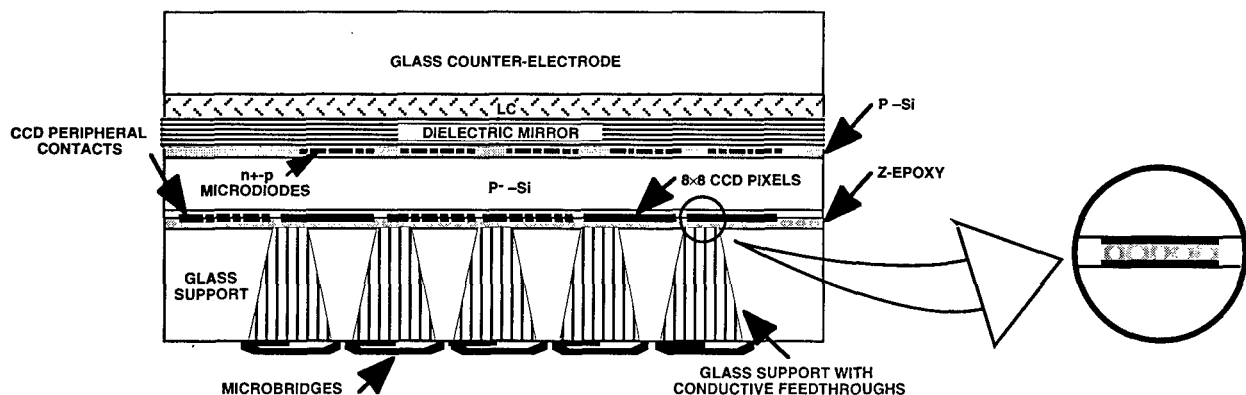


**Figure 4-3. Cross section of the CCD-LCLV with conductive feedthroughs in the supporting glass.**

To make contact between the conductive feedthroughs in the glass support just mentioned and the corresponding pads of the STC superpixels, we can use a special adhesive which is conductive only in one direction.<sup>(4,4)</sup> As a result of embedded gold-coated particles which are compressed along this direction during curing, this adhesive, which is referred to as the z-axis adhesive, conducts only in the direction along its thickness. There is no conduction in the lateral directions due to the low density of these particles. This approach has been verified to be suitable for the STC assembly.

#### 4.1.2 Mechanical Design

In order to use the CCD chip as an optical device it is necessary to package it so that the back surface of the chip with the liquid crystal layer is exposed. This means that the chip has to be mounted in a flip-chip fashion with the CCD side in contact with the substrate. This requires an interconnect method between the CCD pads and the substrate. This is frequently done in the industry using a Z-axis adhesive that conducts vertically between the substrate and the chip, but not horizontally between lines or pads.

A design was generated for the layout of the substrate. This included analyzing the overall size constraints and coming up with a fanout pattern that allowed as many superpixels as possible to be brought out to a contact area around the edge. The drive signals also had to be brought in through some kind of detachable connector. A mechanical design of the mounting fixture was also developed since it was an integral part of the system surrounding the support substrate.

A one inch square quartz plate was chosen as the substrate for the compander chip. A fanout and interconnect pattern was designed that provided connection for the drive signals along one edge and contact to 88 of the superpixels on the other edges. The drive signals will be connected to the substrate using a mating Kapton ribbon cable with a pressure plate contact. An alternative fanout pattern was also designed that allowed contact to the optical and electrical test devices on the side of the chip.

The mechanical design of the mounting fixture was also completed. It was desirable to keep the size small and the assembly simple. The mounting base plate for the substrate was only one half inch larger than the substrate and will support the pressure connector for the drive signals. A counterelectrode holder and pressure plate will also mount directly to the base plate. The whole assembly could be mounted vertically for testing on an optics bench.

A mechanical design was also developed for depositing the ITO layer on the counter-electrodes with a contact metalization on the side of the glass. The technique used a shadow mask approach with an angled deposition for the metal. Glass samples used under the CCD-LCLV project were found to be compatible with the compander, so it was not necessary to re-design new pieces. Drawings for the shadow mask fixture were fabricated.

A Kapton ribbon connector was designed to provide signal contacts to the compander substrate. The layout was designed using a PCB CAD program and the artwork was photographically reduced. The pattern was contact printed onto the Kapton material and etched. The copper traces were tin plated in the contact area to prevent oxidation. Continuity was measured to ensure all lines were defect free. The edge of the ribbon will be pressed against the substrate contacts using a pressure plate with a rubber gasket. The other end of the ribbon cable had a commercially available high density connector that connected to the drive electronics.

The cable to the drive electronics was wired in parallel with the probe card connector so the mounting fixture or the probe station could be used without having to interchange coax cables. The mounting fixture was tested with a continuity check to make sure all the signals were getting through to the CCD substrate.

#### **4.1.3 Electronic Driver Design**

For the Space-Time Comander to be used as an imager it will be necessary to view the output data visually to demonstrate proper operation. A computer program was written to display the active elements of the superpixel array on the computer screen with the proper aspect ratio and spacing. The data in selected superpixels could be dynamically updated on the screen as the CCD was read out. A commercial 24 channel logic analyzer module was used to sample the superpixels simultaneously and transmit the data over a high speed serial link to the host computer. The update rate was somewhat less than the actual CCD frame rate, but the visual image would give the desired results.

A system level design was completed for driving the comander in both the imager and light valve modes. The logic analyzer module was used to accept data in the imager mode and output it over the serial interface. The same signal lines were used to input the data in the light valve mode. A circuit board would be added to the CCD clock timing generator to allow data patterns to be generated for stripes and squares of various pixel sizes. The patterns were static but could be changed through wiring options for each superpixel. A new computer system was installed with a higher clock rate to speed up the display process somewhat, although a faster system would ultimately be wanted for real time demonstrations.

#### **4.1.4 Optical Interfaces**

Limited by the physical presence of microbridges in the 3-D computers and the nature of the CCD structures, the STC supercells must be physically separated from each other with a fairly large gap. This prevents us from using a simple magnify/demagnify optical system to bridge between fine-grain images and the coarse-grain processors. The optical system in the STC must be capable of grouping supercells from continuous fine-grain images and matching those supercells to isolated coarse-grain processors. This function may be achieved with appropriate lens arrays. The lens arrays are used to group the supercells and physically separate them from a continuous image, the concept is illustrated in Figure 4-4. Each lens in the array will image a portion of the fine-grain image to the corresponding CCD sub-array. The design constrain is to prevent multiple images from neighboring lenses overlapped on a single CCD imager. On the other hand, the images are allowed to be overlapped in the area between the CCD arrays. Thus, a practical match can be achieved by balancing the image magnification ratio (MR) and the coverage ratio (CR). Here the

coverage ratio is defined by the ratio of the size of input image “viewed” by a single lens to the size of the supercell. The lens design must follow the constraint:

$$CR \leq \frac{2 - MR}{MR} \quad (4-1)$$

here the magnification ratio is less than one; demagnification is required for the operation. Once the lens array satisfies the imager requirement, it will automatically meet the need for the modulator function. This is based on the fact that there is no information in the adjacent area between the CCD arrays.

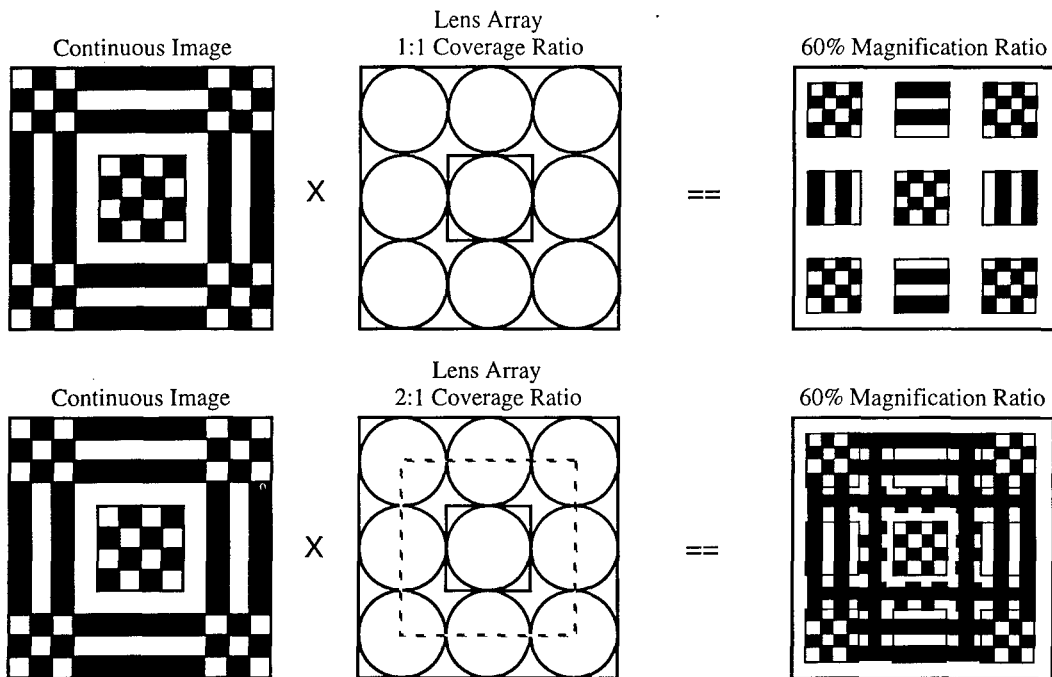


**Figure 4-4.** The concept of using microlens array for mapping optical images to physically separated CCD arrays. The ideal case is to demagnify the necessary area in the optical image to the CCD array. Image overlapping is allowed if the lens imaging constraint is followed.

## 4.2 CCD DESIGN FOR STC APPLICATION

The design of the CCD Componder circuit on the input (front) side of a wafer involves the analysis of the normal CCD device and also the interaction of the CCD to the liquid crystal devices on the output (back) side of the wafer. Initial design efforts for the CCD circuit on the STC were concentrated on defining the specifications of the circuit. The physical constraints imposed by the backside spatial light modulating (SLM) layers and the compatibility with the 3-D Computer were considered. These specifications and considerations were used as the basis in establishing the CCD process supported by our potential CCD foundry (Orbit Semiconductor). The design issues span

over three inter-related levels: circuit design, device design and process design. This section describes the pertinent design parameters in each level.

#### **4.2.1 CCD Design Analysis**

The process and device designs are usually driven by circuit level specifications. The CCD circuit has two physical requirements: it should contain a  $16 \times 16$  array of identical super-pixels and each super-pixel should equal in size to a node on the parallel processor array. The existing 3-D Computer design has a node size of  $448 \mu\text{m} \times 448 \mu\text{m}$ . Each superpixel is further required to consist of a  $8 \times 8$  array of serial-parallel-serial (SPS) CCD pixels, one I/O pad and the necessary input and output circuitry as shown in Figure 4-5. Given these constraints, the CCD pixel size should be maximized to allow maximal charge transfer between the CCD and the liquid crystal devices while keeping crosstalk among pixels minimal. A pixel size of  $30 \mu\text{m} \times 30 \mu\text{m}$  is chosen with  $22 \mu\text{m}$  wide channel and  $8 \mu\text{m}$  spacing. Next important circuit parameter is the number of clock phase of the CCD array. It must satisfy the layout constraint imposed by the above pixel size, and the signal integrity requirement which is determined by the operational frequency and the charge transfer efficiency. The operational frequency is targeted at 1.25 MHz for analog signals, assuming an 8-bit D-to-A conversion from the 3-D Computer which runs at 10 MHz. To safeguard against process and design uncertainties, two clock schemes (two-phase and three-phase) for the serial-CCD circuit had been included on the wafers. The two-phase structure is desirable because it requires one less clock driver and the clock line width is slightly larger. However, it requires an extra implant and is more critical regarding clock drive parameters.

In addition to the CCD array pixels, we have to design the input circuit and the output amplifier. We have decided to use the charge presetting (Tompsett scheme) input circuit for its high linearity and low noise characteristics. For the output amplifier, we have picked the floating diffusion scheme. The detailed design of the amplifier requires more detailed simulation which will be discussed later.

The primary device design parameter is the charge transfer efficiency. It is a function of, among other parameters, the clock voltage and whether the CCD is a surface or buried channel device. For process simplicity, we incline towards a surface channel device but this decision requires confirmation from analysis on the charge transfer efficiency and will be discussed in next section. Another important device parameter is the gate voltage/substrate doping required to deplete the substrate fully (from front to back side) for the imager mode of operation. The objective is to deplete the substrate with as low a voltage as possible within the constraints of the wafer thickness and substrate doping concentration. From a mechanical standpoint, we have succeed in processing wafer with thickness not smaller than  $125 \mu\text{m}$  and this will be our thickness target. We can also obtain  $p^-$ -type wafers with doping level not higher than  $5 \times 10^{12}/\text{cm}^3$  consistently. Given these



targets, the expected full depletion voltage is calculated to be about 60 V. However, this substrate doping level would be too low for the CCD circuit operation and an epi layer of higher doping level is required. To facilitate deep through-wafer depletion, the 5  $\mu\text{m}$  epilayer generally used on the  $\text{p}^-$ -Si substrate for fabricating the CCD gate structures is replaced with a thin (about 0.2  $\mu\text{m}$ ) p-type sheet implant layer. In the output amplifier section, the MOS transistor also needs characterization to avoid source-drain punch-through. This affects the operating voltage as well as the minimum gate length (hence speed) of the output device. Other device parameters that need to be characterized include the threshold body factor and the junction capacitance which impact the circuit operation.

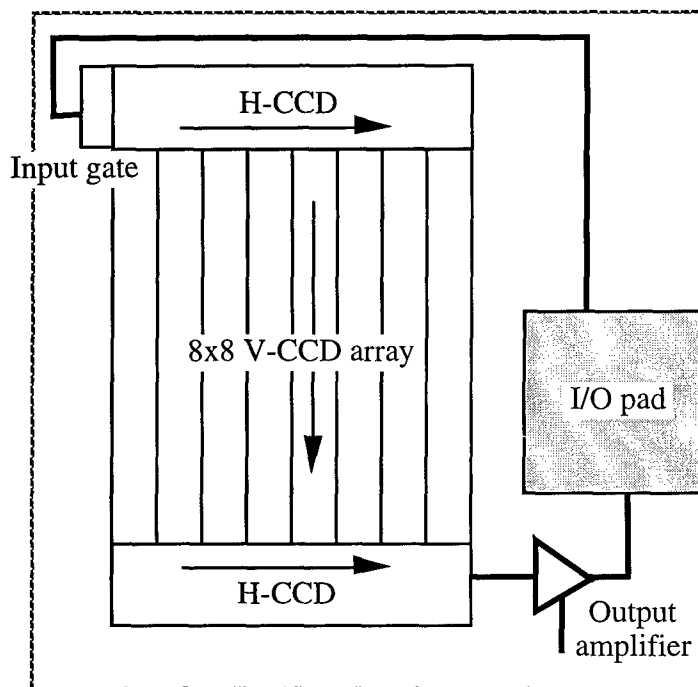


**Figure 4-5. Floorplan of one superpixel of STC indicating direction of charge flow.**

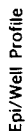
In the process design area, the number of poly (CCD electrode) layers will be determined by the clock phase requirement of the CCD circuit. A three-phase clock requires three poly layer while a two- or four-phase clock requires only two poly layer. For a two-phase clock an additional barrier implant is needed, though it can be the same as the threshold adjust implant. Another important process parameter is the gate dielectric thickness, which has to support the maximum gate voltage at full depletion. The epi layer and the threshold adjust implant are the two major adjustable processing steps that have direct impact on the device and circuit characteristics described above. Finally, the source-drain dopant specie (arsenic versus phosphorus) determines the junction depth and affects the punch-through voltage.

### 4.2.2 CCD Design Analysis Tools

In order to quantify the interaction of the above mentioned circuit, device and process parameters, both analytical and numerical tools have been employed. For analytical tools, we have developed two spreadsheet (Excel) programs. The first program calculates the doping profile of the epi layer and the threshold adjust implant as a function of the process parameters such as implant dose and high temperature processing steps. It also explores the approximate replacement of the epi layer by a well implant and a long drive-in step which we shall also pursue experimentally. This program approximates the implanted profile as a Gaussian profile and calculates the spreading of the dopants due to thermal diffusion while taking into account the segregation of the dopant (boron) at the oxide interface. The final profile is then fitted with a Gaussian profile which can then be used in commercial 2-D numerical device simulation programs. A sample of the spreadsheet printout together with plots of the epi layer, the replacement well implanted profile and the threshold implanted profile are shown in Figure 4-6.

The second spreadsheet program calculates the charge transfer efficiency as a function of the number of clock phase, voltage and other process, device and circuit parameters, both for the Horizontal (serial) and the Vertical (parallel) CCD devices. The program takes into account the self-induced field, the fringing field, the diffusion and the surface-state components, and combine them in an approximate way to arrive at an effective transfer efficiency. This program also calculates the 1-D full depletion voltage under the CCD gate, the threshold voltage body factor and the junction capacitance coefficients of the MOS transistor in the output amplifier circuitry. The last two sets of parameters will be used as device parameter inputs to commercial circuit simulation programs. A sample of the spreadsheet printout is shown in Figure 4-7.

Two numerical simulation programs have been used for the CCD design. On the device level, the 2-D device simulation program PISCES was used for source-drain punch-through simulation. Given a MOS transistor structure and the applied terminal voltages, the program will solve the 2-D Poisson's and Continuity equations for the electrical potential and the carrier concentrations. A sample potential profile is shown in Figure 4-8 showing the separation of the depletion edges between the source and the drain of the transistor. This simulation is performed with a drain voltage of 16 V, giving enough margin for a 12 V operation. On the circuit level, circuit simulator MacSPICE was used to simulate the CCD output amplifier and to guide the layout design of the various transistors. Because of the highly non-uniform substrate doping seen by the transistors, two device models were used to represent the transistors that operate in the respective substrate voltage ranges. The output amplifier circuit schematic and its voltage and current waveforms are shown in Figure 4-9.



41

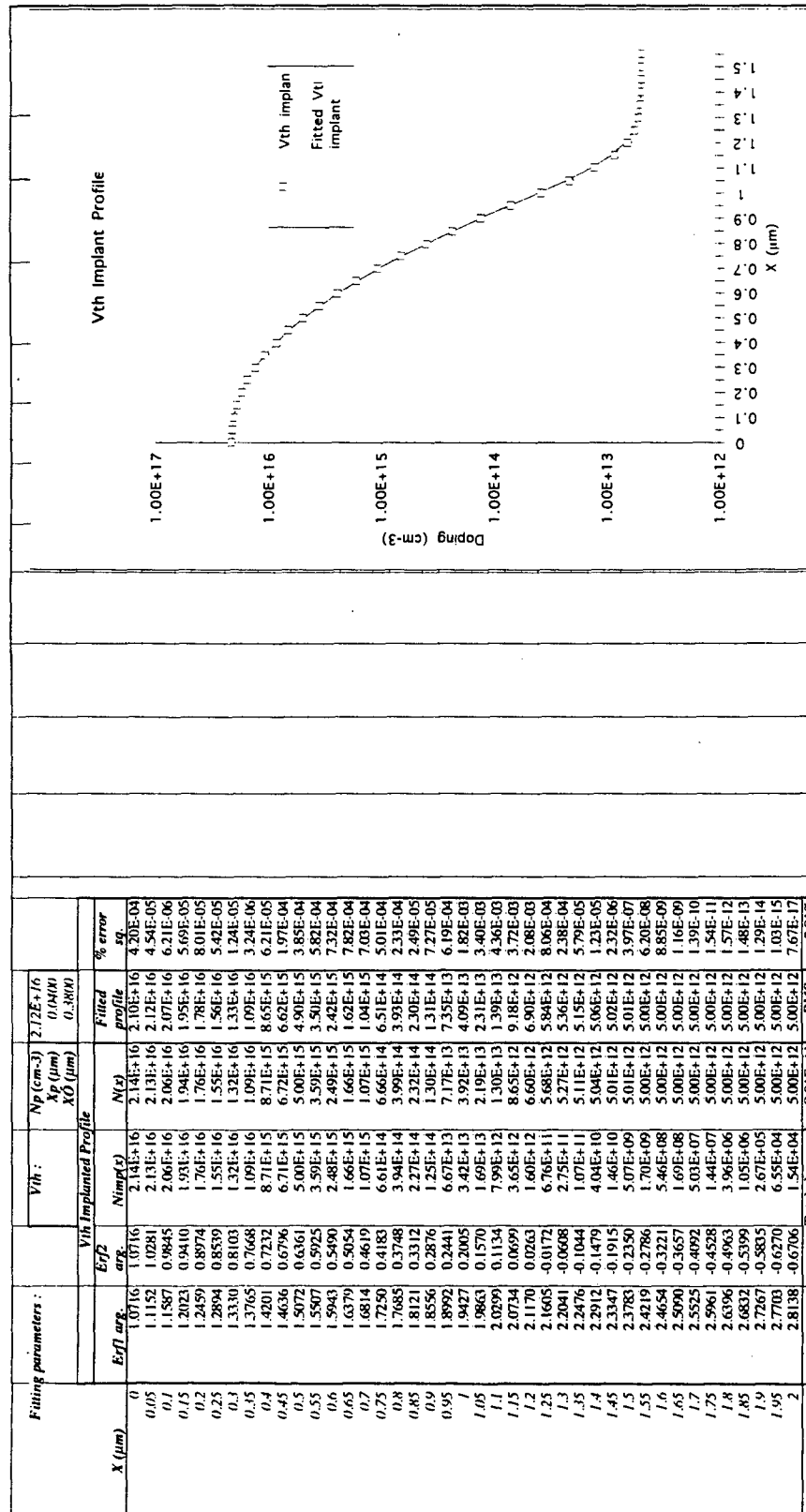


Figure 4-6 (b). Spreadsheet program and plots for the epi layer, the replacement well implanted profile and the threshold implanted profile.

**Figure 4-7. Spreadsheet program for calculating the charge transfer efficiency, the full depletion voltage under the CCD gate, the threshold voltage body factor and the junction capacitance coefficients of the MOS transistor in the output amplifier.**

## CCD punch-through - Potential

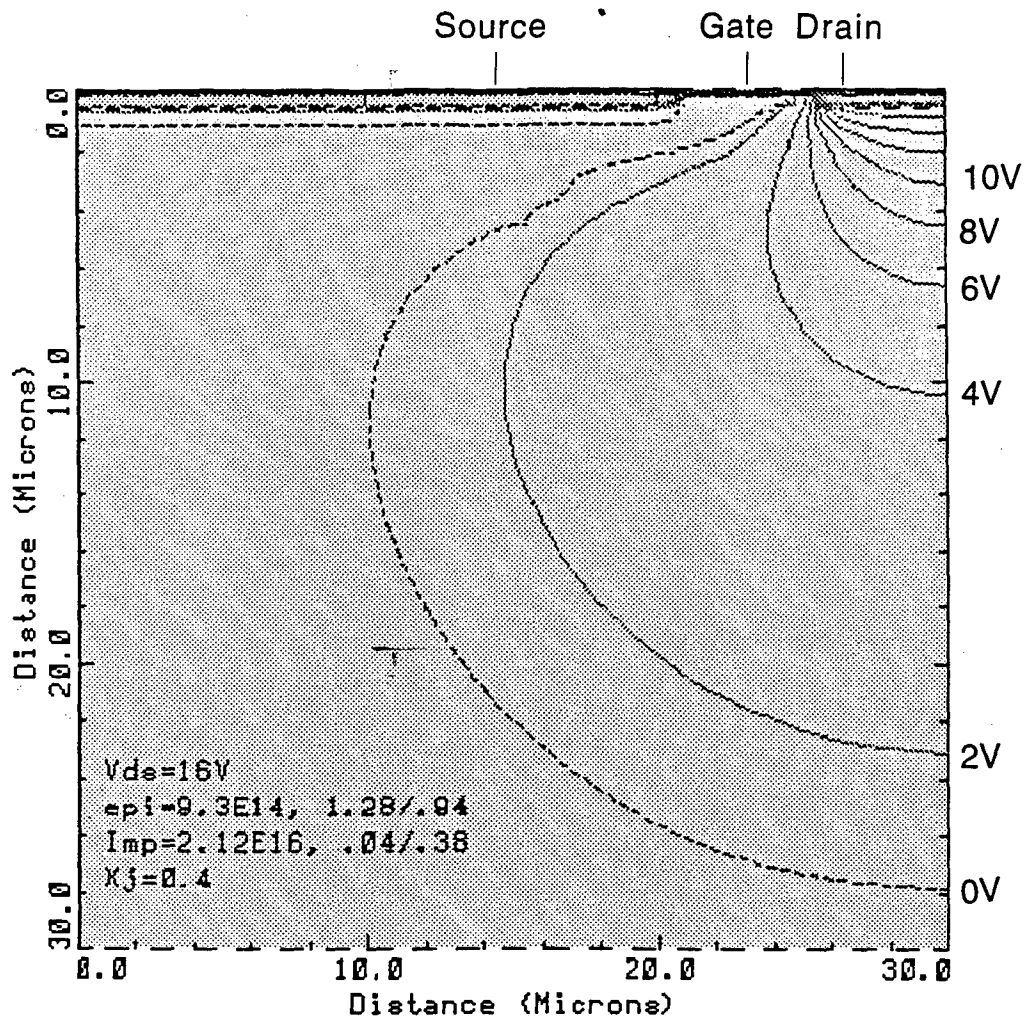


Figure 4-8. Cross-sectional 2-D potential profile of the output MOS transistor showing the separation of the depletion edges from the source and the drain, as generated by punch-through simulation using PISCES.

# CCD COMPANDER OUTPUT AMPLIFIER SCHEMATIC Single stage source follower, thick gate dielectric

```

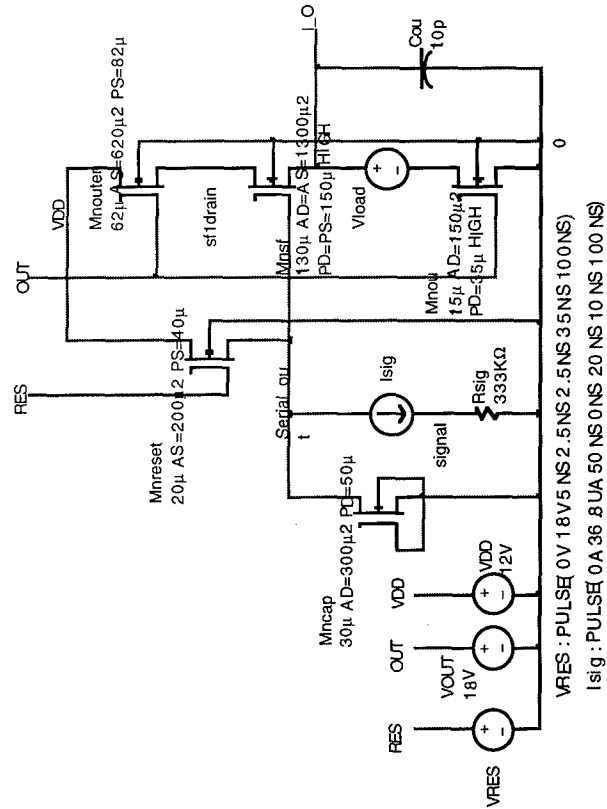
SF CCE2=include CCD_nom1.nal
!Cserial_out=5V
OPTION S DEF L=6U DEF W=3U DEF AD=40P DEF AS=40P DEF PD=21U DEF PS=21U
+ REL TOL=.005 A BSTOL=100P VNTOL=1.0U1 TL1=200
+ FV TOL=1E-13 PIVREL=1E-3
TRAN 5NS 100NS

```

\*\*\*\* Calculated N-Channel CCD model parameters (950Å+700Å gate) \*\*\*\*  
 \*\*\*\*\* NMOSH HIGH model for Vsb=0 to 5V, NMOS model for Vsb=6 to 10V  
 \*\*\*\*\*

model NMOS NMOS level=2 uo=600 vto=2 tpg=1 tox=137e-9 xj=4e-6  
 + nsub=7e16 nfs=5e10 ucrit=164e3 uexp=-.3855 vmax=61.2e3 rsh=30 ld=.1e-6  
 + neff=0.8 delta=1.8 pb=0.8 cj=1.2e-4 mj=1.67 cjsw=.0002e-6  
 + mjsw=0.8 cgso=08e-9 cgdo=08e-9 cgbo=.0003e-6

model NMOSH HIGH NMOS level=2 uo=600 vto=2 tpg=1 tox=137e-9 xj=4e-6  
 + nsub=1.5e16 nfs=5e10 ucrit=164e3 uexp=-.3855 vmax=61.2e3 rsh=30 ld=.1e-6  
 + neff=0.8 delta=1.8 pb=0.8 cj=1.2e-4 mj=2 cjsw=.0002e-6  
 + mjsw=0.8 cgso=.08e-9 cgdo=.08e-9 cgbo=.0003e-6



FINAL  
DESIGN

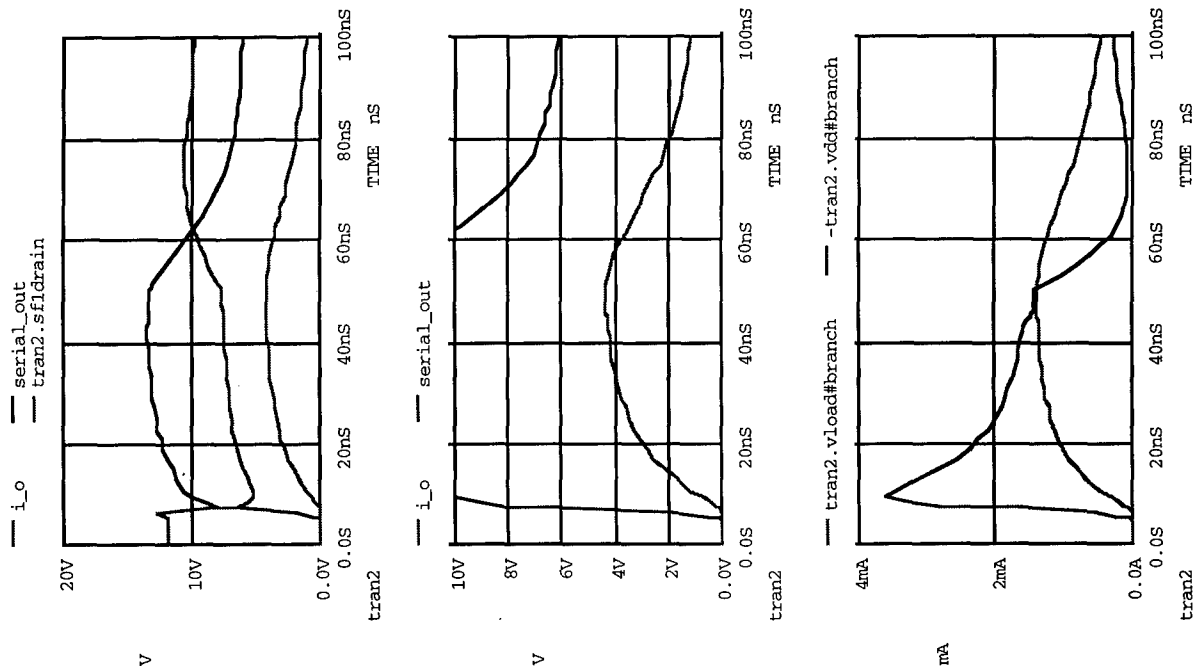


Figure 4-9. Output amplifier circuit schematic, device models and the voltage and current waveforms as generated by circuit simulation using SPICE.

### 4.2.3 CCD design analysis results

Based on the above design analysis, we completed the CCD circuit design and, together with the circuit foundry, established the process necessary for its fabrication. The basic design parameters are summarized below :

#### 1. Circuit:

- Surface channel CCD
- Two phase clock or three phase clock for H-CCD, and three phase clock for V-CCD
- Charge presetting input scheme
- Floating diffusion output amplifier with one source-follower stage

#### 2. Device:

- 12 V operating voltage except for the RESET and OUTEN control lines which use 18 V
- Full depletion voltage about 64 V
- Minimum gate length of output transistor is 6  $\mu\text{m}$
- Threshold voltage of output transistors is 2 V with body factor ranging from 1.9 to 3.0  $\sqrt{\text{V}}$
- Zero-bias junction capacitance is  $1.2 \times 10^{-4} \text{ F/m}^2$  with voltage coefficient = 1.67 – 2

#### 3. Process:

- 2- $\mu\text{m}$ -thick,  $1 \times 10^{15}$  per  $\text{cm}^3$  p-epi layer on  $5 \times 10^{12}$  per  $\text{cm}^3$  p-substrate
- Triple poly
- Single metal
- 950-Å-thick oxide + 750-Å-thick nitride gate dielectric
- Threshold adjust (also serve as barrier) implant parameters :  $9 \times 10^{11}/\text{cm}^2$  boron at 100 keV
- Arsenic source-drain implanted junction of 0.4- $\mu\text{m}$  deep

An overall charge transfer efficiency of about 94% is expected from this design when operating at 1.25 MHz or slower.

Overall we had eight different versions of the circuit chips incorporated in the floorplan of the whole wafer and one of each was available for pre-thinning characterization. In each of the circuit chips, besides the  $16 \times 16$  superpixels, there were test circuits that could be used to characterize line resolution and transfer efficiency of the front-back charge transfer process. There were also test circuits for testing the operation of individual super-pixel, a shorter serial-CCD chain and a shorter parallel-CCD chain (the product had an  $8 \times 8$  CCD array). Figure 4-10 shows the floorplan of a typical Comander chip with test cells populating to the right and below the  $16 \times 16$  superpixel array. Figure 4-11 shows the layout of the superpixel containing an  $8 \times 8$  CCD array.



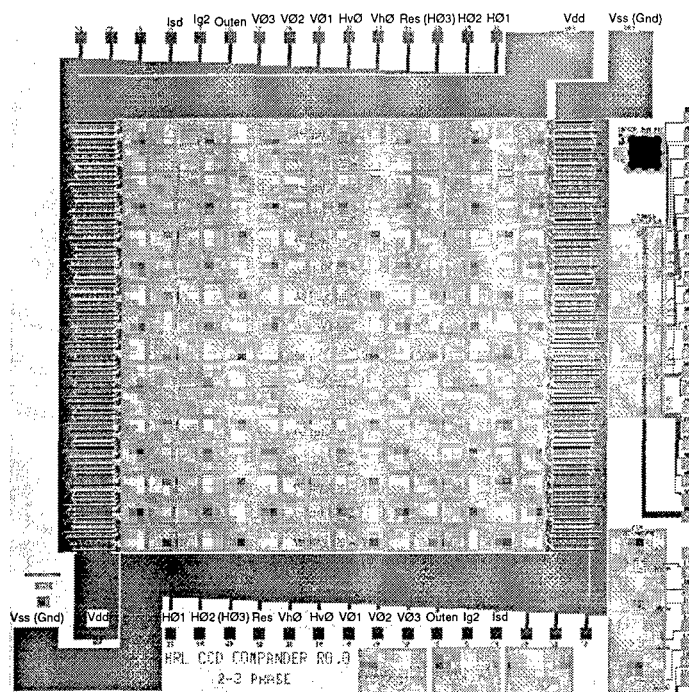


Figure 4-10. Floorplan of Space-Time Compander chip.

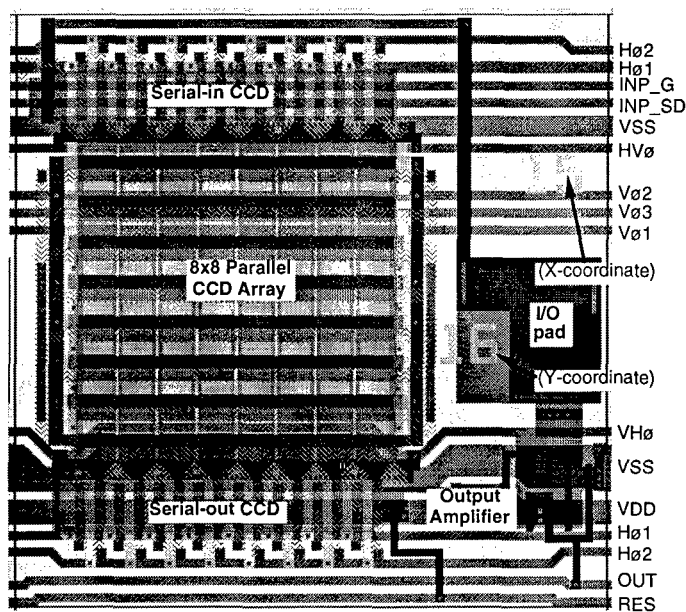


Figure 4-11. Space-Time Compander superpixel (8x8 CCD array) layout.

## **Section 5**

# **EOCA SYSTEM ANALYSIS**

For the purpose of EOCA system analysis we have developed switching energy requirements and delay models for RC limited lines in the 3-D computer, as well as simplified models for Si-CMOS light receivers, and integrated lasers. We developed models for comparing the performance of electronic and optical interconnects. Results (see Subsection 5.1) show significant advantages for free-space optical interconnects versus RC limited lines in the 3-D computer environment. In the general area of the EOCA, we also optimized the architecture of the one stage-shuffle interconnection network for permutation traffic in the 3-D computer (see Section 5.2) and developed the concept of the time-dilated network for low blocking communications. The routing and sorting and the FFT operations on the EOCA system are analyzed and presented in Subsection 5.3.

### **5.1 ELECTRONIC VERSUS OPTICAL INTERCONNECTS IN THE 3-D COMPUTER**

An important study in this program is to identify when and how free-space optical interconnects should be used in the 3-D computer. It has been proven that, architecturally, it is critical to provide global interconnections to the 3-D computer to speed-up the machine, in particular for image processing applications. In this section we first outline the limitations of the 3-D electronic systems compared to similar 3-D stacked systems which would be interconnected using free-space optoelectronic technology. Then we show that from a power/throughput point of view free-space optoelectronic technology is a good candidate to implement such global connections.

#### **5.1.1 Architecture Consideration**

It is instructive to compare the potential performance of the Hughes 3-D VLSI computer with its electronic counterparts as well as with the potentials of the optically augmented 3-D computer. Here, computational tasks for low level and higher level image processing applications are considered. These tasks can be classified either by their computational complexity or by the globality of information transfer required by the computation. Simple operations involving multiple images such as image addition and subtraction require only point-wise operations between images. Point or "histogram" based operations manipulate the value of a pixel based on the values of some or all or the other pixels in the image, but do not require knowledge about specific pixel location. Window or "convolution" based operations apply kernels of arbitrary sizes to enable pixel values to be modified by a function of the other pixels within the window. For compute bound

operations, such as matrix inversion or window-based convolution, erosion, dilation etc., the 3-D computer provides fast processing by virtue of its single-instruction multiple data parallel processing capability: window operations are reduced from  $O(N^2K^2)$  time for a serial processor to  $O(K^2)$  time for the 3-D computer for a kernel of size  $K \times K$  pixels; likewise the time complexity of matrix inversion is reduced from  $O(N^3)$  to  $O(N)$ .<sup>(5-1)</sup>

In the cases where the computational complexity is bound by the communication capability of the machine, the use of an optoelectronic multistage interconnection network (MIN) within the 3-D computer can significantly reduce processing times. In Table (5-1), processing times for the optically augmented 3-D machine are compared to the 3-D computer and a serial electronic approach for communication bound operations. For applications such as routing and FFT, that are naturally suited to a Butterfly network structure, the optoelectronic system provides significant speedup. For certain point operations, data-sorting may be required. This will be possible in  $O(\log^2 N)$  time using a MIN. Finally,  $K \times K$  kernel generation can be performed in parallel assuming additional simple functionality can be incorporated into the switching elements of the multistage interconnection network.<sup>(5-2)</sup>

**TABLE 5-1. Performance comparison of the regular and augmented 3-D VLSI computer for Image processing applications.**

NxN image KxK window	Serial Electronic Processor # processors = 1	3-D VLSI Computer # processors = $P=N^2$	Optically Augmented 3-D VLSI Computer # processors = $P=N^2$
Point Operations (e.g. Histogram Calc.)	$O(N^2)$	$O(N)$	$O(\log_2^2 N)$
Fourier Transform (DFT/FFT)	$O(N^2 \log_2 N)$	$O(N)$	$O(\log_2 N)$
Routing (e. g. matrix transpose)	$O(N^2)$	$O(N)$	$O(\log_2 N)$
KxK Kernel Generation	$O(K^2)$	$O(K^2)$	$O(\log_2^2 K)$

### 5.1.2 Technology Consideration

As illustrated in Fig. (5-1), there are two ways of implementing global connections within the 3-D VLSI computer: one using free-space optoelectronics, the other with a dedicated interconnection layer. We assume that the interconnections on the dedicated layer are RC limited lines since their lengths and their operating frequency do not provide transmission line regime. The electrical model we use for the electrical interconnections, from the source on the lower layer to the destination on the upper layer through an Al line on the interconnection layer, is shown in

Fig. 5-2(a). Note that throughout this section it is assumed that data is coded on the links in an Non-Return-to-Zero fashion. In addition, to simplify the derivations, a 50% duty cycle is also assumed.

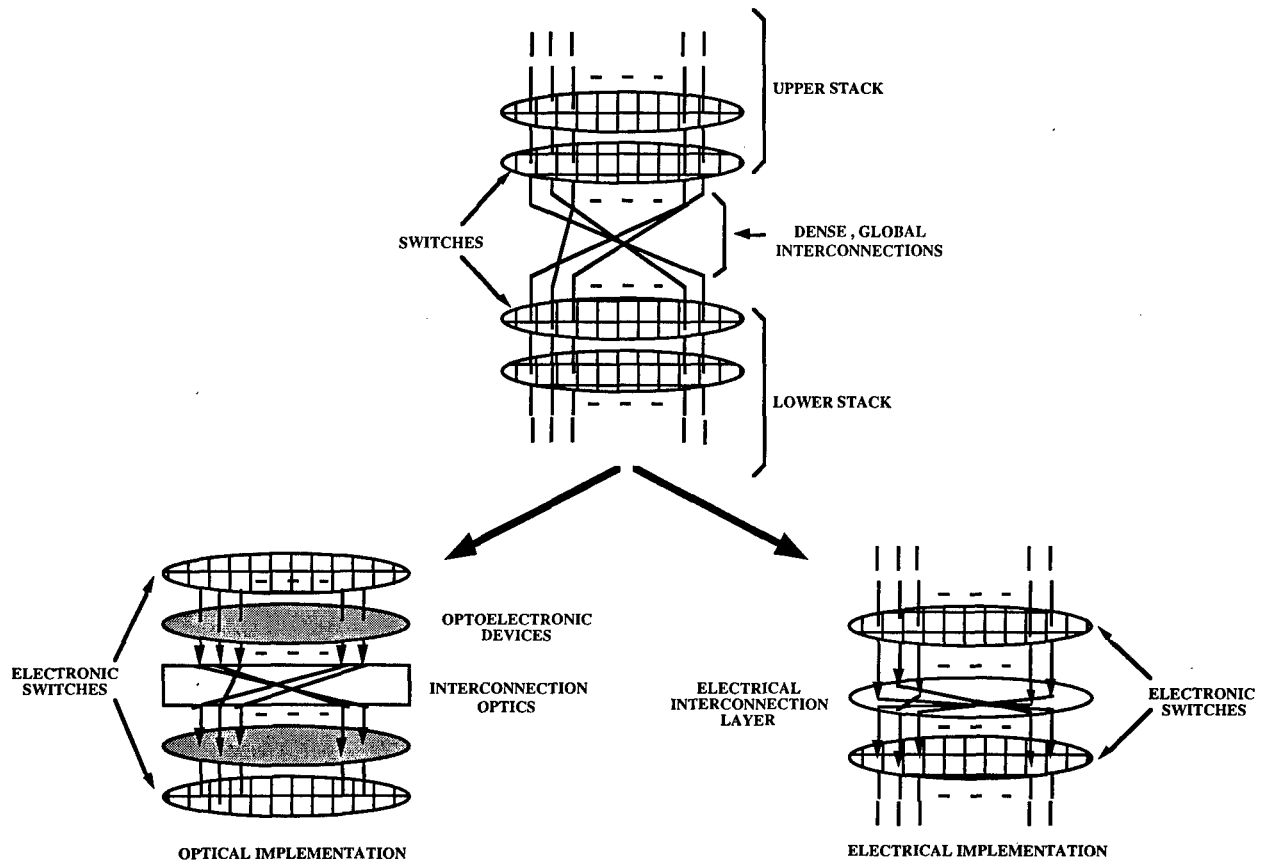


**Figure 5-1. Electronic vs. optoelectronic global connections in a 3-D computer system.**

From source to destination, the electrical model contains: a driver  $D$  with an output capacitance  $C_{out}^d$ , a switch ( $C_s, R_s$ ), a bridge ( $C_{BR}$ ) and via ( $C_{via}, R_{via}, I_{leak}$ ) pair, the Aluminum line on the interconnection layer ( $R_{int}, C_{int}$ ), another bridge/via pair, and a CMOS receiver  $R$  with an input capacitance  $C_{in}^r$ . The switches provides bi-directionality to the connection in order to preserve the functionality of the 3-D computer. In this model we use a standard superbuffers (multistage) design for the source driver.<sup>(5-3)</sup> It can be shown that the required number of stages ( $n$ ) to drive the connection and the delay ( $T_d$ ) introduced by the driver is:

$$n = \frac{\ln\left(\frac{C_{load}}{C_0}\right)}{\ln(\beta)}$$

$$T_d = n[1 + (\beta - 1)p]R_0C_0 \quad (5-1)$$

We use standard CMOS 1.2  $\mu\text{m}$  technology parameters which leads  $\beta = 5$ ,  $C_0 = 23 \text{ fF}$ ,  $R_0 = 8.7 \text{ K}\Omega$ ,  $C_{\text{load}} = 3 \text{ pF}$ , and  $p = 0.25$ . This yields  $n = 3$  and  $T_d = 1.3 \text{ nsec}$ . The vertical delay for the via/bridge pair can be calculated as:<sup>(5-4)</sup>

$$T_{VB} = 0.7R_S[C_S + C_{in}^r + C_{out}^d + C_{BR} + C_{VIA} + 2C_S + C_{in}^{rp}] + 0.4R_{VIA}C_{VIA} + 0.7R_{VIA}[2C_S + C_{in}^{rp}] + 0.7R_S[C_S + C_{in}^{rp}] \quad (5-2)$$

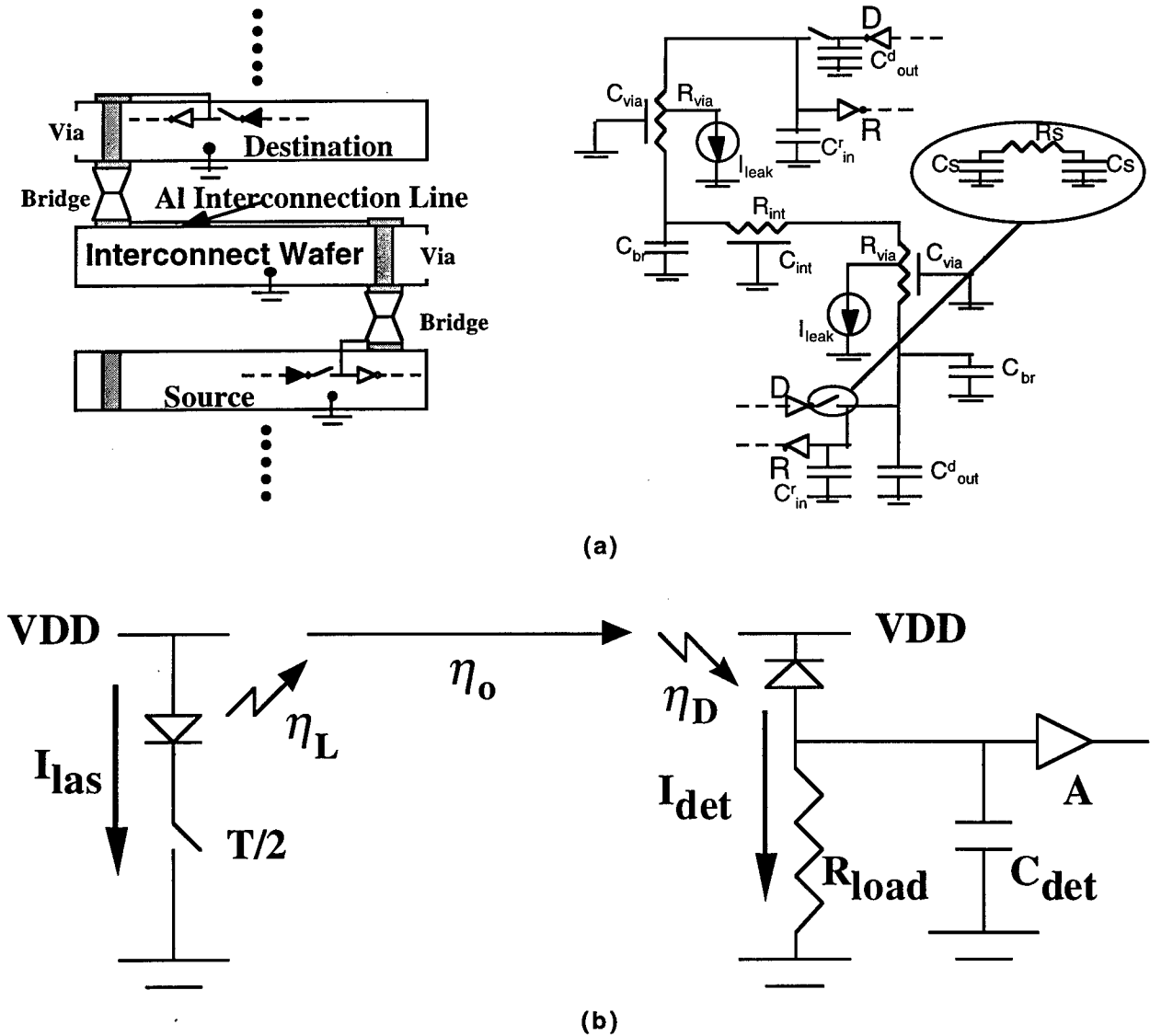


Figure 5-2. (a) Physical and circuit equivalent model of electrical connection in the 3-D VLSI computer, (b) Simplified circuit equivalent model of an optoelectronic interconnection

with  $R_{\text{via}} = 20 \Omega$  (resistance of a via),  $C_{\text{BR}} + C_{\text{VIA}} = 1.5 \text{ pF}$  (capacitance of a bridge + a via), and  $C_{\text{P}_{\text{in}}} = 0.86 \text{ pF}$  (input capacitance of a repeater).  $C_{\text{r}_{\text{in}}}$  is the input capacitance of the CMOS receiver and  $C_{\text{d}_{\text{out}}}$  is the output capacitance of the driver. Note that the switches are chosen so that they are as large as the largest inverter which leads  $R_{\text{S}} = 100 \Omega$  and  $C_{\text{S}} = 60 \text{ fF}$ . By combining Eq. (5-1) and Eq. (5-2) and using the values for  $1.2 \mu\text{m}$  technology it can be shown the total vertical propagation delay ( $T_{\text{V}}$ ) from the driver to the interconnection layer is:

$$T_{\text{V}} = 1.7 \text{ nsec} \quad (5-3)$$

Then, we need to calculate the delay for the Al interconnection line on the interconnection layer. In order to minimize the delay on this line, it is necessary to use optimally designed repeaters in terms of size and spacing. For  $1.2 \mu\text{m}$  technology, it can be shown that for a line of length  $L_{\text{int}}$ , the optimal number of repeaters ( $k$ ), the optimal repeater size ( $h$ , in terms of minimum gate size) and the delay ( $T_{\text{IW}}$ ) are:<sup>(5-4)</sup>

$$\begin{aligned} k &= \frac{L_{\text{int}}}{1.67} \\ h &= 77 \\ T_{\text{IW}} &= 0.4 L_{\text{int}} \end{aligned} \quad (5-4)$$

Since the line segments between repeaters ( $1.67 \text{ cm}$ ) have similar parasitic characteristics as the bridge/via pair, the last repeater on the interconnection layer is capable of driving the vertical connection through via/bridge to the CMOS receiver at the destination. The delay ( $T_{\text{L}}$ ) of this last part of the interconnection can be calculated from Eq. (5-4) with  $L_{\text{int}} = 1.67 \text{ cm}$ :

$$T_{\text{L}} = 0.67 \text{ nsec} \quad (5-5)$$

Therefore, the total delay for source to destination ( $T_{\text{SD}}$ ), as a function of the interconnection line length on the interconnection layer and given in nsec, is simply found by adding Eqs (5-3), (5-4), and (5-5):

$$T_{\text{SD}} = T_{\text{V}} + T_{\text{L}} + T_{\text{IW}} = 2.4 + 0.4 L_{\text{int}} \quad (5-6)$$

The delay due to the interconnection will then limit the maximum clock frequency at which a connection of a given length can be driven. Two cases are being envisaged: one where the data is sent straight from the source to the destination, one where the data is being latched on the interconnection layer and then resent.

The total equivalent driver size ( $H$ ) of the interconnect from source to destination, where  $H$  is expressed in terms of the relative size to a minimum size inverter, is then:

$$H = 31 + 77 \left( \frac{L_{\text{int}}}{1.67} + 1 \right) \quad (5-7)$$

which corresponds to three inverters in the superbuffer of sizes 1, 5, and 25 and  $L_{int}/1.67$  repeaters of size 77.

The other metric of interest for this analysis is the energy ( $E_{elec}$ ) required to drive the connection from source to destination as a function of the line length on the interconnection layer. It can be shown that the total switching energy required per bit is simply the sum of the DC energy due to the junction leakage in the vias plus the switching energy defined as the power required times the rise time:

$$E_{elec} = Pt_r + 2I_{leak}V_{DD}T \quad (5-8)$$

where  $P = H \frac{V_{DD}^2}{R_0}$ ,  $t_r$  is the rise and time (assumed equal to the fall time) of a switching transition,  $1/T$  is the operating frequency of the system,  $V_{DD}$  is the supply voltage, and  $I_{leak}$  is the leakage current of the vias. The interesting result from the delay and switching energy requirement models is that both increase linearly with the interconnection length ( $L_{int}$ ) on the interconnection layer.

We now have to derive the equivalent energy model for an optical link ( $E_{opt}$ ) in order to compare electronic and optoelectronic technologies for interconnections in the 3-D computer environment. Fig. (5-2b) shows the simplified model that we used for an optical link. We assume a VCSEL as a light transmitter with a threshold current ( $I_{th} = 1$  mA), a bias voltage  $V_{DD}$ , a laser current ( $I_{las}$ ), and a conversion efficiency ( $\eta_L$ ). We also assume a p-n junction diode receiver ( $R_{load}$ ,  $C_{det}$ ) with a quantum efficiency ( $\eta_D = 0.3$ ) that generates a photo current ( $I_{det}$ ), followed by an amplifier circuit of gain  $A$ . The free-space link between the transmitter and the receiver is modeled by a simple optical transmission efficiency ( $\eta_O$ ).

Assuming a voltage power supply  $V_{DD} = 5V$  identical for both transmitter and receiver circuits, an operating frequency of  $1/T$  (with a rise time  $t_r$  and a fall time  $t_f$ ), and a standard detector capacity ( $C_{det} = 110$  fF for a standard Si PIN diode in  $1.2 \mu m$  technology) the energy requirement for the optoelectronic link is simply:

$$E_{opt} \cong V_{DD} \frac{T}{2} (I_{las} + I_{det} + I_{th}) \quad (5-9)$$

In this equation the DC power consumption in the CMOS receiver is neglected as it will always be much less than the other terms. Also note that  $I_{det}$  only becomes significant at very high speeds. Considering the speed requirement of the detector ( $I_{det} = C_{det} \left( \frac{V_{DD}}{A} \right) \frac{1}{t_r}$ ) and the relation between

the required laser current and the detector current ( $I_{las} = \frac{I_{det}}{\eta_L \times \eta_O \times \eta_D}$ ) Eq. (5-9) reduces to:

$$E_{opt} \cong a \frac{C_{det} V_{DD}^2}{2A\eta} + \frac{TI_{th} V_{DD}}{2} \text{ per bit} \quad (5-10)$$

with  $\eta \equiv \eta_L \times \eta_O \times \eta_D$  and  $a \equiv T/t_r$ . Note that the first term of Eq. (5-10) is the photo current required for switching the connection while the second term is the energy required to maintain the VCSEL at the threshold current value. The parameters which present the most interest in Eq. (5-10) are the product  $\eta A$ , which represents the overall efficiency of the optoelectronic interconnect (including the detection circuit). It can be easily seen that for a given operating frequency ( $1/T$ ) the required switching energy is directly related (inversely proportional) to  $A\eta$  whereas for small values of  $T$  (large operating frequency) the second term of equation 10 becomes negligible. For the rest of the calculations we assume that  $a = 5$  in Eq. (5-10), which means that the rise time ( $t_r$ ) is assumed to be 20% of the operating period (this is usually considered an acceptable value).

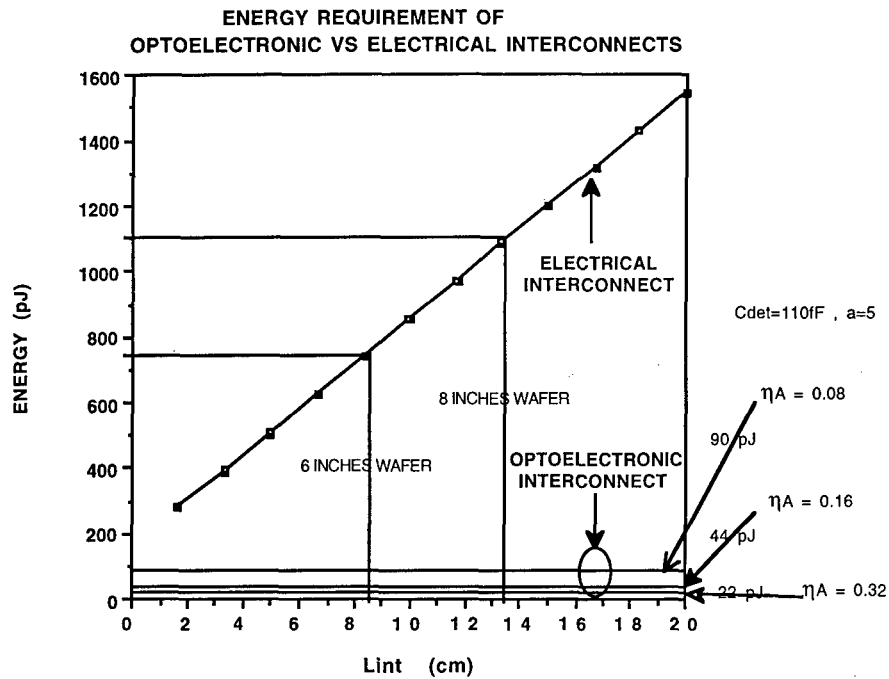
Figure (5-3a) shows the plot of switching energy requirements for both technologies. For each line length ( $L_{int}$ ), the operating frequency is taken as the maximum achievable by the electronic line. This makes the second term of Eq. (5-10) negligible and the optical energy becomes a constant essentially independent of line length. It can be seen that at the highest achievable channel speed, an electrical connection in the 3-D computer, requires 3 to 20 times more switching energy than its optoelectronic counterpart.

In the energy model that we have developed, it can be seen that there are two independent contributions to the total electrical switching energy. One,  $E_{ver}$ , is due to the vertical connections (source, bridges, vias, destination) and is a constant, independent of connection length. The other,  $E_{iw}$ , is due to the line on the interconnection layer and increases with line length.

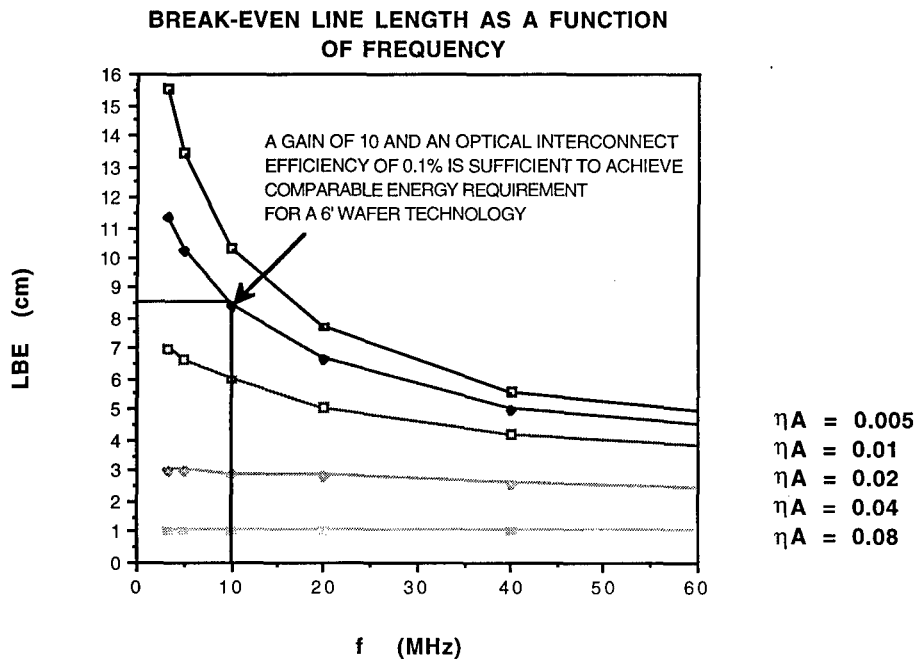
$$E_{elec} = E_{ver} + E_{iw} \quad (5-11)$$

Therefore, for a given operating frequency, we can find the break-even line length, at which it becomes advantageous to use an optical link. From the previous equations it can be shown that if the product  $A\eta$  is greater than 0.15, then  $E_{ver} > E_{opt}$  and it is always advantageous to use optoelectronics. If  $A\eta$  is smaller than 0.15 then there will be a domain (up to a specific break-even length) where it is advantageous to use an interconnection layer. Note that a gain-efficiency product of 0.15 means an optoelectronic system with a wall plug efficiency of 1.5 % and a receiver circuit gain of 10 which is readily achievable today with optoelectronic technologies. In addition, this assumes that a single inverter is used as an amplifier in the receiver circuit, limiting the range of possible values of  $A$  to less than 20. If more gain was required in the receiver, more complex designs such as multi-stage transimpedance receiver circuits could be used. However, the power consumed in the receiver would also be increased.





(a)



(b)

Figure 5-3. (a) Energy requirements vs. line length for optoelectronic and electronic interconnections in the 3-D computer, (b) Break-even line length for optoelectronic vs. electronic connections in the 3-D computer.

The results on the break-even line length are shown in Fig. (5-3b). For example at the present speed of a few tens of MHz in a 3-D computer, it already is more efficient to use free-space optoelectronics interconnects with a gain-efficiency product of only 0.01 (e.g., wall plug optical efficiency of 0.1% and receiver circuit gain of 10) for connections greater than 8 cm. Such wire lengths will exist in a system implemented on 4-inch wafers or equivalent that require global connections. This is a very encouraging result because today's optoelectronic technology already allows such gain-efficiency products in free-space links.

## 5.2 OPTICALLY AUGMENTED 3-D VLSI COMPUTER

It has been shown in the previous sections that global interconnections are advantageous for many operations in a parallel system. In addition, free-space optoelectronic technologies offer good performance potential for implementing such connections.

### 5.2.1 The Optical Transpose Interconnection System

The Optical Transpose Interconnection System (OTIS) is a one-to-one interconnection between  $P$  transmitters  $\{P_t\}$  and  $P$  receivers  $\{P_r\}$ , where  $P_t$  and  $P_r$  range from 0 to  $P-1$  and  $P$  is the product of two integers,  $M$  and  $N$ . Since  $P = MN$ , the indices  $P_t$  and  $P_r$  can be divided into ordered pairs  $(n_t, m_t)$  and  $(m_r, n_r)$  respectively, where  $m_t$  and  $m_r$  range from 0 to  $M-1$  and  $n_t$  and  $n_r$  range from 0 to  $N-1$ , such that:

$$P_t = M n_t + m_t ; P_r = N m_r + n_r$$

$$n_t = \text{trunc} ( P_t/M ) ; m_r = \text{trunc} ( P_r/N ) \quad (5-12)$$

$$m_t = P_t \text{ modulo } M ; n_r = P_r \text{ modulo } N$$

The indices  $n_t$  and  $m_r$  are referred to as the *major indices* of the transmitters and receivers, respectively,  $m_t$  and  $n_r$  are called the *minor indices*, and  $P_t$  and  $P_r$  are referred to as the *scalar indices*. In the transpose interconnection,  $(n_t, m_t)$  is connected to  $(m_r, n_r)$  if and only if  $m_t = m_r$  and  $n_t = n_r$ . Such an interconnection is called an  $M \times N$  transpose.

An important application of OTIS is in support of multistage interconnection network architectures (OTIS-MIN) based on  $K$ -shuffles.<sup>(5-5)</sup> A  $K$ -shuffle MIN functionally provides full connectivity between  $P$  input channels (PEs) and  $P$  output channels (PEs) in  $\text{Log}_K P$  stages of optoelectronic switch planes and  $(\text{Log}_K P) - 1$  stages of optical  $K$ -shuffles. One optoelectronic switch has  $K$  optical inputs (receivers) and  $K$  optical outputs (transmitters) and provides full routing between its  $K$  channels. In a  $K$ -shuffle, the receiver  $P_o$  to which  $P_i$  is connected is given by:

$$P_o = K \{ P_i \text{ modulo } (P/K) \} + \text{trunc} ( P_i/P ) \quad (5-13)$$

where  $\text{trunc}(x)$  is defined as the greatest integer  $\leq x$ . If  $M$  is set equal to  $P/K$  and  $N$  is set equal to  $K$  then

$$P_0 = N m_i + n_i \quad (5-14)$$

Equating (12) with (14) for arbitrary values of  $P_i$  implies that  $n_0 = n_i$  and  $m_0 = m_i$ . Therefore, a  $K$ -shuffle is equivalent to a  $(P/K) \times K$  transpose. An interesting application of the OTIS-MIN arises when  $K = (MN)^{1/2}$  since the number of stages for routing becomes a constant:

$$\text{Log}_K P = \text{Log}_{\sqrt{MN}} MN = 2 \quad (5-15)$$

In this case only 2 stages of optoelectronic switches and 1 stage of optics are required to perform full routing between source and destination planes, independent of the total number of communication channels ( $P$ ) in the MIN. As described in Fig. (5-4), the principle of the optoelectronic system for routing application requires 2 stages of optoelectronic switching elements and a single stage of optical interconnects. This optical interconnection system consists of two identical planes of diffractive optical elements containing  $\sqrt{P}$  lenslets. For use within an OTIS-MIN system, each optoelectronic stage of the network contains  $\sqrt{P}$  optoelectronic  $\sqrt{P} \times \sqrt{P}$ -switches (switches with  $\sqrt{P}$  inputs and  $\sqrt{P}$  outputs), arranged in a square 2-D array with the

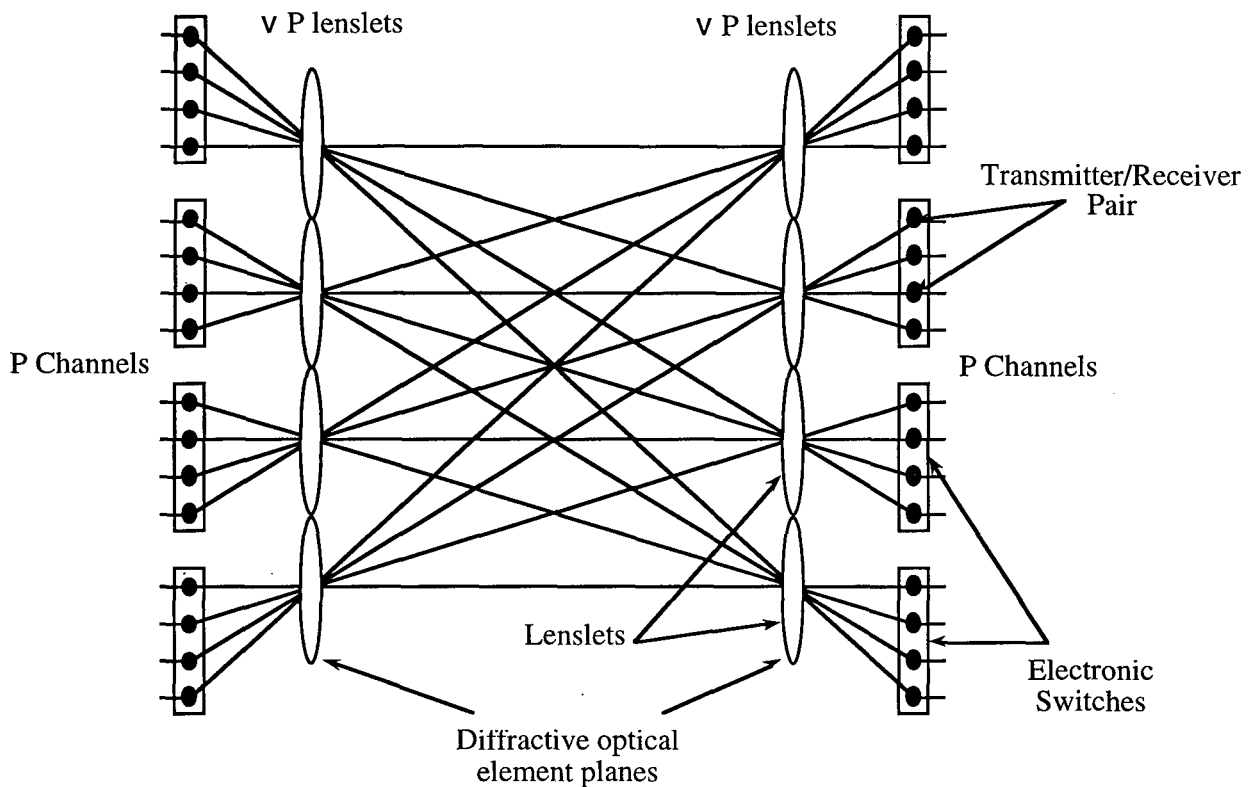


Figure 5-4. OTIS as a  $\sqrt{P}$ -shuffle interconnection.

modulators and the detectors being uniformly distributed in the plane. Note that in a related study the area, the power consumption and speed of such approach have been analyzed and proven to be near optimal.<sup>(5-5)</sup>

### 5.2.2 Additional Consideration on OTIS

Another important feature of the Optical Transpose Interconnection System is that it can be made bi-directional. This is crucial in the 3-D VLSI computer environment since it does not put any restriction on the vertical through wafer electronic bus. The implementation of the bi-directional OTIS optical system is shown in Fig. (5-5). Plane 1 and Plane 2 are now both transmitter/receiver planes. Plane 2 is actually rotated 180° with respect to plane 1 so that a transmitter on plane 1 faces a receiver on plane 2 and vice-versa. Beam blocks between adjacent lenses are required in order to avoid crosstalk. These beam blocks are located on the lower half of the transmitter lenses and the upper half of the receiver lenses thereby reducing slightly the light efficiency of the system.

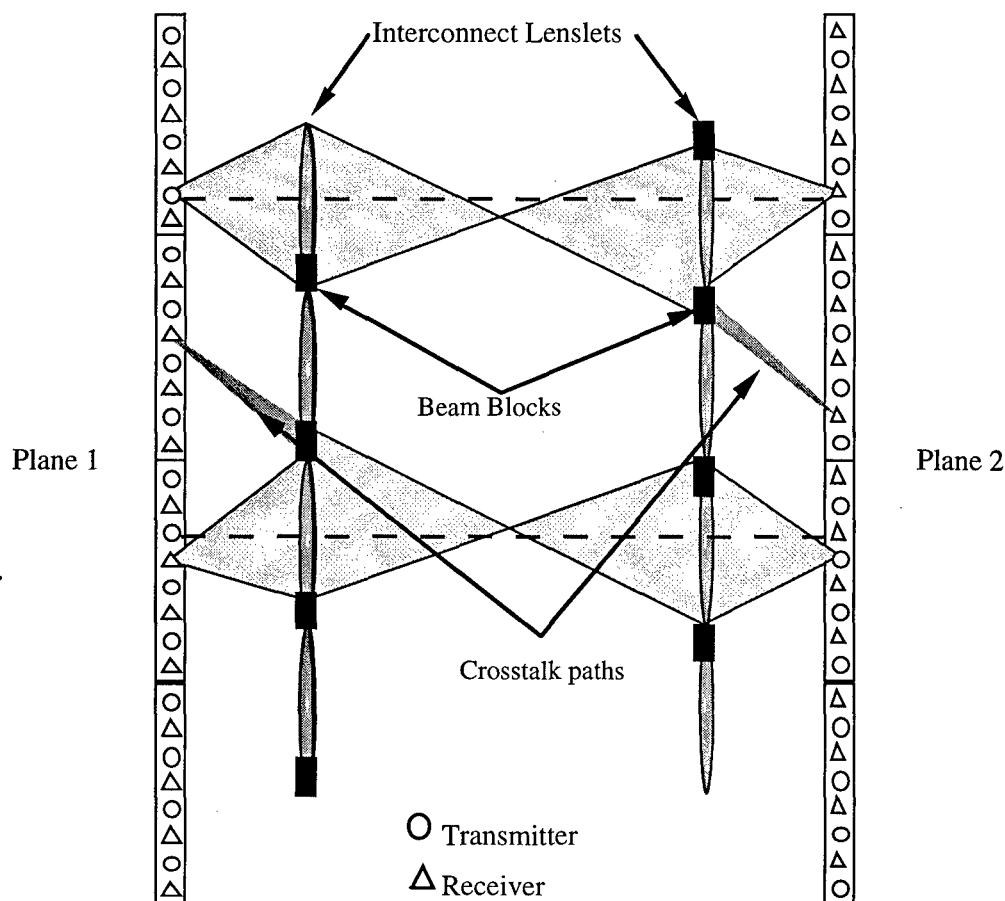


Figure 5-5. Bi-directional OTIS for switching applications.

An illustration of the schematic assembly of the OTIS-MIN in the 3-D computer environment is given in Fig. (5-6). In this case, only one power coupling element (usually a Polarizing Beam Splitter) is required for the implementation of a single stage OTIS. This element also provides the mechanical structural support for the system. The optical data (dashed lines on Fig. (5-6)) is then transmitted from the 3-D stack 1 to 3-D stack 2 and back via the bi-directional OTIS optical system. The power for the modulators is routed to the OEICs (solid lines on Fig. (5-6)) through an optical system that uses identical lenses as the OTIS interconnection system. It is interesting to notice that new technologies such as the Birefringent Computer Generated Holograms<sup>(5-6)</sup> allow dramatic simplifications of the optical system by providing the possibility to combine in the same element the spot array generator and the OTIS lenses.

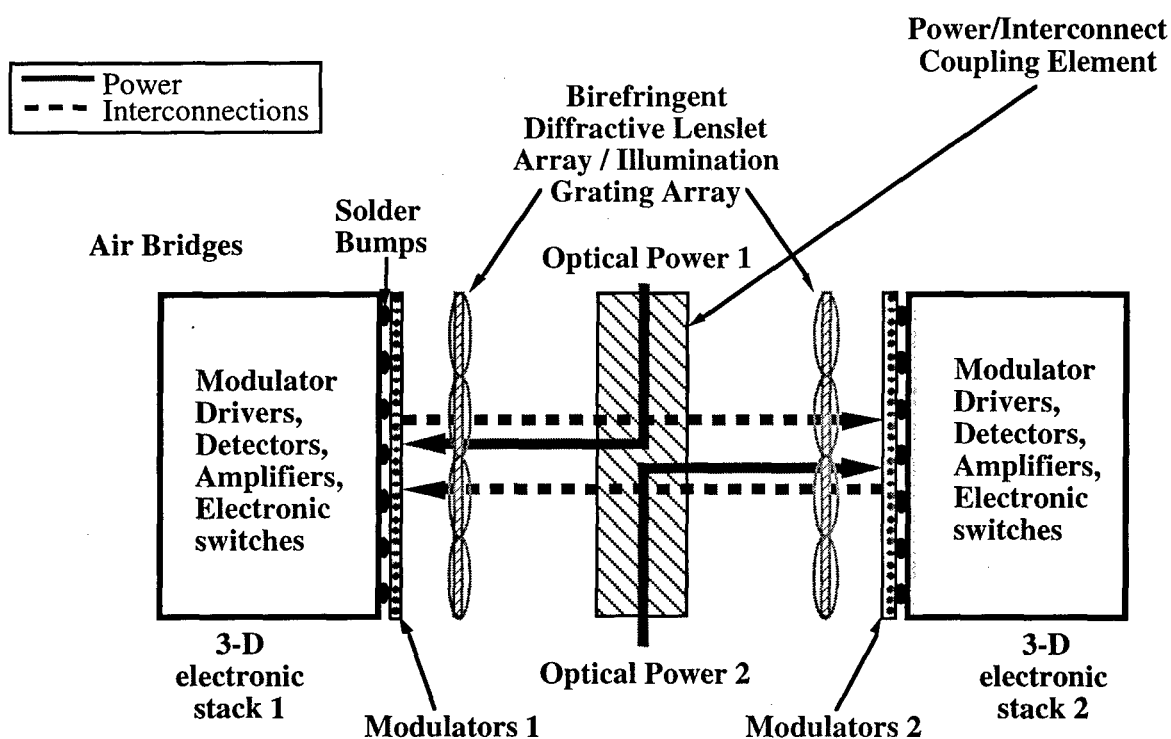


Figure 5-6. Principle of the assembly of the optically augmented 3-D VLSI computer.

### 5.2.3 Time Dilated Network

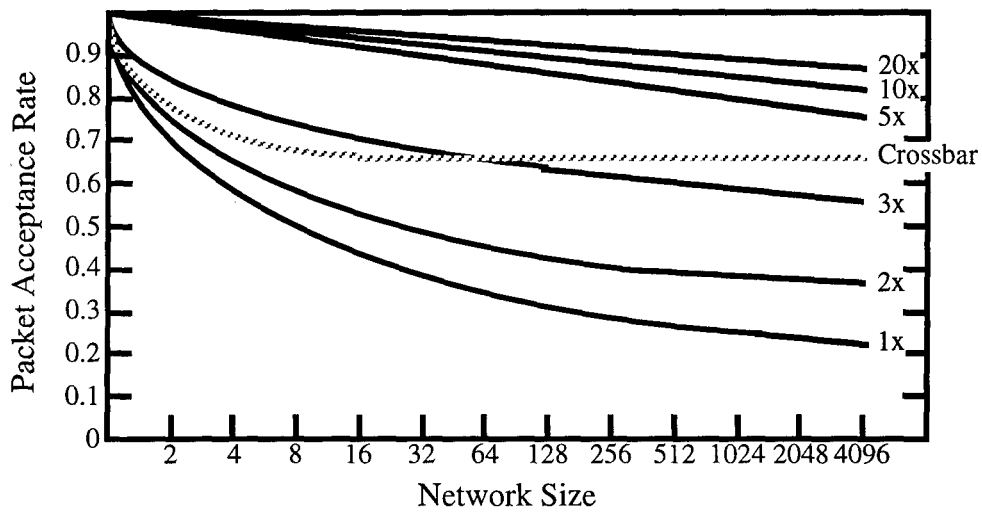
The metric of importance to evaluate the performance of a network is its bandwidth. The bandwidth of the network is the expected number of network requests accepted per unit time. Network bandwidth is defined as the product of system clock speed, network size ( $N$ ), and probability that an arbitrary request will be accepted by the network ( $P_a$ ). When two packets are routed to the same output of the  $2 \times 2$  basic switching element, it is assumed that one randomly chosen packet is dropped. Destination addresses for the packets are generated independently, with

uniform probability  $P$ . Under these assumptions, it can be shown that the average bandwidth of the 2-D shuffle-exchange network for  $2 \times 2$  grain, for large values of  $N$ , is given by:

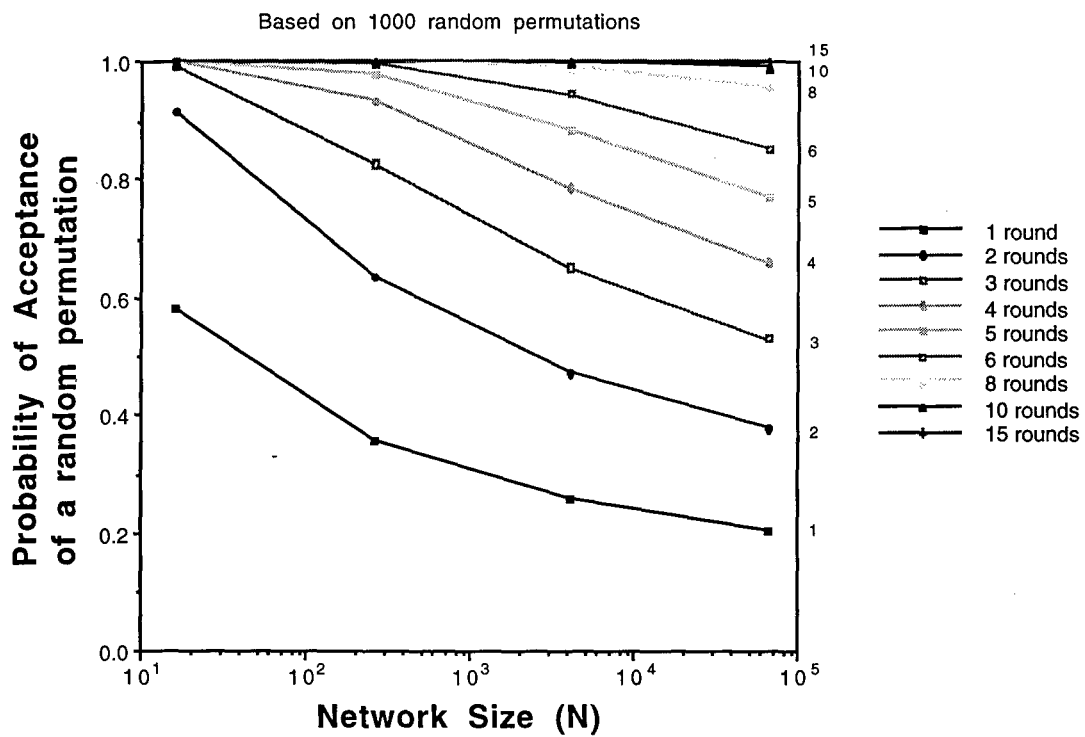
$$BW_2 = F N P_a = F N \frac{4}{\text{Log}_2 N} \quad (5-16)$$

where  $F$  is the network clock speed and  $P_a = 4/\text{Log}_2 N$ . It should be noted that the worst case bandwidth can be as low as  $O(\sqrt{N})$ , and the worst case includes important permutations of bit reversal and matrix transpose. The formula given in Eq. (5-16) is also valid for MINs with  $K \times K$  grain since each  $K \times K$  grain is built using simple  $2 \times 2$  switching elements.

Figure (5-7a) shows the analytical acceptance rate of the network as a function of network size. The dashed line on the plot shows the standard reference point for network performance which is that of a crossbar. The other lines are the performance of our network for various conditions; the line marked  $1 \times$  shows the acceptance rate for the standard network. In the case of the optically augmented 3-D computer with a one-stage OTIS based shuffle network, Fig. (5-7a) shows that the time dilated network concept<sup>(5-7)</sup> offers great potential for lowering the blocking probability of the system. This concept is very simple, it assumes that the network can be operated faster than the processors attached to the network and that blocked data packets are buffered at the input of the network and then resent if they have been blocked. In this approach, it is a practical solution since the clock frequency of the processors is only a few tens of MHz and the data packet size is only 16 bits. Note that the performance shown on Fig. 5-7(a) are for random traffic only. For permutation traffic, the acceptance rate of a Crossbar is one and the acceptance rate of our time dilated network is expected to approach one. To evaluate the performance of the time-dilated network under permutation traffic conditions, we performed simulations for which the results are given in Fig. 5-7(b). These results are based on the average of 1,000 permutations. It shows that for a network with 4096 channels only 10 rounds are required for routing the complete permutation. This means that a  $10 \times$  time-dilated network will route a random permutation with probability one. However, it should be noted that there will always be a worst-case routing pattern that will require  $\sqrt{N}$  rounds in the network for complete routing. This is the case for example of the identity permutation. Such patterns can be detected a priori and time can be allocated to perform the routing. Note also that in this network routing a transpose operation permutation, which is usually a worst-case routing pattern for most networks, will only require one routing step.



(a)



(b)

Figure 5-7. Performance of the time-dilated network for (a) random traffic and (b) permutation traffic.

## 5.3 APPLICATIONS STUDIES

### 5.3.1 FFT Studies

One of the important application areas where silicon based systems remain inadequate is the manipulation and processing of large data arrays as required, for example, by image processing and understanding applications. Although many parallel algorithms exist in this domain, their mapping on existing system architectures usually lead to unsatisfactory performance when the image sizes are large. This is because the computational speed of the algorithms that require such manipulation of large data arrays is presently limited by hardware considerations rather than by software and/or algorithm mapping. Thus, new hardware solutions capable of performing operations such as histogram, centroid, moment, segmentation, and FFT calculations at high speeds are critically needed for the implementation of real time and adaptive signal processing systems. For example, if such operations could be performed on  $1024 \times 1024$  data arrays with 32 bit accuracy at high speed video rates, significant improvements could be achieved in electronic warfare and industrial control applications.

The present hardware limitations result from an intricate relationship between chip area, allowable power dissipation, and the number of channels available for I/O, memory access, and inter-chip communication as well as their respective bandwidth. Indeed, as the size of the data arrays increase, it becomes exceedingly difficult to pack the required processing units and sufficient memory within one single chip to carry out the required computation at high speeds. On the other hand, the use of parallel hardware with many chips is very difficult because of the bandwidth required by I/O, inter-chip communication, and memory access. In this case, the delays and power required to support the required communication become prohibitively large.

In this report, we focus our efforts on a 2-D free-space optoelectronic FFT engine capable of processing  $1024 \times 1024$  or larger images. The selection of FFT as an application example stems from two reasons. First, FFT operations are essential in many digital image processing applications and the implementation of FFT processors has been studied in detail by the electronics community. Thus, performance benchmarks are readily available which enable us to identify the benefits of the proposed optoelectronic approaches. Second, many systems would benefit significantly from faster 2-D FFT engines. For example, faster and more efficient 2-D video compression units and real time adaptive noisy image recovery systems could be implemented.

Section 5.3.1.1 provides a background on FFT algorithms and outlines the state of the art in current and projected FFT performance on all electronic systems including dedicated chip sets, more general DSP chips, and supercomputers. The roadblocks and limitations of these FFT systems are then outlined. Section 5.3.1.1 also describes chip to chip digital interconnection technologies such as MCM and free-space optical interconnects. In Section 5.3.1.2, we discuss



two possible OTIS based free-space optoelectronic 2-D FFT architectures that perform 1K×1K-point FFTs. We also estimate the potential performance of the proposed architectures if we were to implement them with present state of the art MCM technologies and extend our analysis to future MCM technologies for the next five years. Then, we compare both optoelectronic approaches to their MCM interconnect based counterparts for 1K×1K points FFT operations. In all cases, we show that from a pure performance point of view, a 1K×1K-point or larger FFT engine operating at 1,000 frames per second should be implemented with free-space optical interconnects. Finally, Section 5.3.1.3 presents some discussions and conclusions about the findings of this study.

### 5.3.1.1 Background

#### 5.3.1.1.1 FFT Computation

The Discrete Fourier Transform (DFT), which expresses a discrete-valued function as a superposition of a discrete set of frequencies, has applications in many domains. However, a straightforward formulation of an N-point DFT requires  $N^2$  steps to compute. Fast-Fourier Transform algorithms, such as those attributed to Cooley and Tukey,<sup>(5-8)</sup> can reduce this to approximately  $N \log N$ , a significant difference for even moderately large transform sizes.

One way to generate such FFT algorithms is to begin with FFT algorithms for fixed sized transforms. For example, a 2-point FFT algorithm is:

$$F(0) = f(0) + f(1)$$

$$F(1) = f(0) - f(1) \tag{5-17}$$

where  $f$  is the original function and  $F$  is its Fourier Transform. Such an algorithm would then be used as a building block in a larger algorithm using a mixed-radix approach. Intuitively, applying this 2-point transform across the entire data can be thought of as a filter which divides the data into low and high frequency components. Another stage of 2-point transforms divides each of those components into two components which cover narrower frequency windows. By repeating this  $\log N$  times, we obtain an N-point transform. Even more efficient algorithms can be obtained by using an 8- or 16-point transform as the building block. The resulting algorithms are then termed radix-8 or -16 FFTs. Some additional work is required between stages in order to implement the intuitive picture described above. The data must be multiplied by a constant (often called a “twiddle factor”) and the data array must be rearranged. This rearrangement poses a serious problem for parallel implementation of FFTs. Between each stage, each processor will be required to exchange data with many other processors in order to accomplish the data motion needed to rearrange the array. Thus, a parallel architecture for FFTs must be able to support such communication.

The FFT algorithms described above were for 1-D data. To perform transforms on 2-dimensional data (e.g. images), similar techniques are used. The 2D data is partitioned into sub-images; for example, each row can be considered as a sub-image. In this case, a 1-D FFT is performed on each sub-image, using the methods outlined above. The data array is then rearranged; in our example, each column would now become a sub-image: this operation requires a transpose of the 2-D pattern. In parallel FFT system, this can cause serious communication bottlenecks termed commonly the "corner turn". Finally, a second 1-dimensional FFT is performed, producing the complete transform of the image. Note that the sub-image could very well be a 2-D subsection of the original image in which case the building block of the global 2-D FFT is a smaller 2-D FFT. In any case global communications are required in parallel FFT systems.

#### **5.3.1.1.2 Electronic FFT Systems**

The wide applicability of the FFT has led to many implementations of the algorithms on a wide variety of hardware. At one end of the spectrum, commercially available Digital Signal Processing (DSP) chips are widely used in small-scale applications which require FFT computations. Among the best available are the Analog Devices ADSP-21060 and the Texas Instruments TMS-320-C80, capable of performing a 1K-point 1-D FFT in approximately 460  $\mu$ sec and 160  $\mu$ sec, respectively. There also exist dedicated FFT chip-sets, usually consisting of a specialized FFT processor, memory chips, and address generators. The Sharp LH9125/LH9320 and the Plessey PDSP16150 are examples of such systems, performing 1K-point 1-D FFTs in 87  $\mu$ sec and 96  $\mu$ sec, respectively.<sup>(5-9)</sup> Certainly, technological advances in VLSI design will lead to faster and faster systems. One proposed next-generation dedicated FFT chip would potentially offer 10 times the performance of an existing FFT chip-set.<sup>(5-10)</sup> However, none of these chips has enough computational power to provide 1K $\times$ 1K FFTs at a rate of 1,000 frames/second. For all of these chips, the power consumption, area and cost are either known or can be projected. Table 5-2 summarizes the results for the computation of a 1K-point 1-D FFT and 1K $\times$ 1K-point 2-D FFT.

The areas for the Analog Device and Texas Instruments chips are an estimate based on the fact that these chips are engineered to operate without glue-logic. In the case of a large 2-D FFT performance, they would actually require additional external memory chips. Area figures for the Plessey and Sharp chips are for the chip-set which include the area required by interface, address generator, and memory chips. The speed estimate of the 2-D FFT computation is based on the given speed of the 1-D FFT and the internal architecture of each chip, i.e. using a  $N\log N$  speed scaling to evaluate 2-D FFTs speed from 1-D FFT numbers. We also neglect any overhead that would result from external memory access. Thus, the actual computation times will be somewhat larger for the 2-D FFT case leading to an optimistic performance evaluation of these chips for 2-D FFTs.

TABLE 5-2. Performance Comparison of DSP and dedicated FFT Chip-Sets.

Chip	Power (W)	Cost (\$)	Area (in <sup>2</sup> )	Precision (bits)	Speed ( $\mu$ sec) 1K FFT	Speed (msec) 1K $\times$ 1K FFT
AD 21060	3.6	250	1	32 float.	460	920
TI C80	10	400	1	32 float.	160	326
Plessey	11	3,000	5	16 block	96	192
Sharp	30	4,000	18	24 block	87	174
<i>Future Chip</i>	6	N/A	2.8	24 block	8.3	16

Table 5-2 shows that special purpose chips outperform the more general purpose DSPs at the expense of power consumption, system area and cost. From the table it is also clear that none of the currently available chips can provide the kind of performance required for implementing a 1,000 frames-per-second 1K $\times$ 1K-point complex FFT. Even making use of a projected next-generation chip and ignoring the cost of inter-processor communication, 16 chips would be required to provide that level of performance. Alternatively, one could use 16 of these next generation chips in a pipeline architecture, and in this case, the 1,000 frames per seconds performance could be achieved. This would only be possible at the cost of a very large latency: 16 msec, not adequate for any adaptive systems.

To obtain dramatic speed-up over the existing one chip systems, it will be necessary to combine many chips together in a parallel system. Indeed, FFT computation is an important use of existing supercomputers. However, only large supercomputers have the computational power necessary to solve large 2-D FFTs at high speed. Sample codes written by Aware Inc.<sup>(5-11)</sup> provided the performance shown in Table 5-3.

Table 5-3 shows that even a supercomputer with relatively large parallelism can not achieve the desired performance. Note that other supercomputers (such as the Fujitsu) are given to be faster than the ones mentioned in that table, however no 2-D FFT benchmark data was available for the faster machines. In any case, the improvement will be far less than the order of magnitude required to even approach the desired performance. Table 5-3 also shows that for systems with multiple processors, doubling the number of processors does not double the speed of the system. This is mostly due to the inefficiencies in the memory I/O and the communication between the processors as their number increases.

Thus, in order to offer a good technological solution to the problem of a 2-D 1K $\times$ 1K-point complex FFT at 1,000 frames per seconds the common roadblocks of all these FFT systems must first be identified.

**TABLE 5-3. Summary of 2-D Complex FFT Performance of Various Super-Computer Configurations.**

Intel Paragon Number of nodes	1K×1K FFT (msec)	IBM SP2 Number of nodes	1K×1K FFT (msec)
2	818		
4	428	4	280
8	225	8	150
16	126	16	80
32	80	32	40
		64	30

#### **5.3.1.1.3 Present Roadblocks for Large-Scale FFT Systems**

The limitations of the existing and future electronic solutions to the FFT problem are summarized in this section. They fall into four broad categories:

- For single chip electronic solutions, computation, i.e. the speed of the Floating Point Units (FPUs), is the main limiting factor.
- As the computation problem is solved, through parallelism, the speed of inter-processor communication become critical. If instead of using a fully interconnected system one chose to utilize a highly pipelined architecture then latency becomes a significant issue.
- As the size of the images on which the FFT is performed increases, memory and FPUs will not be on the same chip. In this case, high-speed processor to memory communication might become a limitation.
- As the required frame rates at which the FFT needs to be performed increase, I/O also becomes a critical point. For example, a fast frame system should be able to handle a sustained 64 Gbits/sec I/O for 1Kx1K-point, 1,000 frames per second, 32 bit precision complex FFT and 1 Tbit/sec for 1,000 frames per second 4Kx4K-point FFTs.

Thus, a parallel system architecture based on the combination of state-of-the-art FPU technologies and high-speed digital interconnects for both I/O and inter-chip communication, with the appropriate packaging technology, will offer the best solution to the problem.

#### **5.3.1.1.4 Interconnection Technologies Modeling**

Since the FFT problem is highly parallel, parallel implementation of FFT engines for large scale problems seems natural. However, such systems become quickly limited by the interconnections. In order to evaluate these limitations and further extract the benefits of an

optoelectronic approach with respect to all electronic solutions, we summarize here the state of the art in present and near future interconnection technologies, both electronic and optoelectronic. In Subsection 5.3.1.2, we will use the interconnection models described here to analyze the expected overall performance of the proposed optoelectronic FFT engines. The modeling is based on work performed at UCSD which includes optoelectronic devices such as VCSELs and modulators, their associated receiver and transmitter circuits,<sup>(5-12)</sup> free-space optical systems based on diffractive optics,<sup>(5-13)</sup> and on-chip and off-chip electronic interconnections.<sup>(5-14)</sup> The latter will be particularly useful when we compare our optoelectronic approach to a fully electrical approach based on MCM implementation. The modeling work is based on present and projected parameters as listed in Table 5-4. It takes into account the fact that processor chips are in general implemented with technologies that are one or two generations behind DRAM technology. For 1995 parameters, we only considered commercially available chips. However, we assumed state of the art off-chip electrical interconnections. In addition, we assumed that by the year 2000, new ceramic materials will be available for MCMs yielding a drop of the interconnect capacitance (per unit length) by a factor of at least 3.

#### **On-chip interconnections**

On-chip electrical connections are important in both an all electrical as well as an optoelectronic implementation. For example, in the optoelectronic approach described in Section 5.3.1.2, there will be a need for evaluating the performance of on-chip electrical connections. Thus, we have calculated the power requirement for lines of various lengths. In this analysis, it is assumed that optimally sized repeaters are used along the lines in order to minimize delay. In Table 5-5 and Table 5-6, the power and energy are related linearly which means that the power at 600 MHz is approximated to simply 10 times more than at 60 MHz.

#### **Off-Chip Interconnections**

As will be shown in Section 5.3.1.2.3, we will compare our optoelectronic approaches to all electrical approaches. The most performant all electrical packaging approaches to date and in the near future remain MCM type implementations. Table 5-4 lists the parameters and their values for the best implementations reported in the literature to date, as well as 5 year projections. MCMs are assumed to be copper wires on co-fired ceramic designated as MCM-C. Using these parameters we can derive the energy requirements and maximum operation frequency of an MCM connection. In the derivations, we assume that the lines are lossless and that the cost of the vias in terms of power and delay is negligible. Note that for lossless lines the maximum frequency of operation is only limited by the impedance matched driver of the line. All the lines are assumed to be series terminated in order to minimize their power consumption. If parallel or active termination is used, the maximum operation frequency of a line will increase by 20 to 30% for an increase of 2 to 3 in power (this is the case both for today's and future technologies). These assumptions lead to results

that are quite optimistic for the MCM implementation. In order to provide insight as to what the performance of such interconnections are, some results for typical line lengths are summarized in Table 5-7.

TABLE 5-4. Today's and Future Parameters for MCM Implementations.

Parameter	Symbol	1995	2000
Chip Spacing	D	5 mm	2 mm
Wire pitch	d	75 $\mu\text{m}$	25 $\mu\text{m}$
Number of layers	L	10	40
Flip-chip bump capacitance	C <sub>pin</sub>	500 fF	100 fF
Via depth	L <sub>via</sub>	200 $\mu\text{m}$	100 $\mu\text{m}$
Propagation speed	v	15 $10^9$ cm/sec	18 $10^9$ cm/sec
Off-chip capacitance/unit length	C <sub>intoff</sub>	2 pF/cm	0.6 pF/cm
Off-chip resistance/unit length	R <sub>intoff</sub>	0.95 $\Omega/\text{cm}$	0.5 $\Omega/\text{cm}$
CMOS technology	2 $\lambda$	0.8 $\mu\text{m}$	0.25 $\mu\text{m}$
Voltage Supply	V <sub>dd</sub>	5 V	3.3 V
Transistor Threshold Voltage	V <sub>th</sub>	.85 V	0.6 V
Minimum transistor resistance	R <sub>min</sub>	3.3 K $\Omega$	5 K $\Omega$
Minimum Logic Time Constant	R <sub>Cmin</sub>	0.2 nsec	0.1 nsec
Minimum transistor transconductance parameter	K <sub>tr</sub>	50 $\mu\text{A}/\text{V}^2$	80 $\mu\text{A}/\text{V}^2$
Minimum inverter input capacitance	C <sub>mini</sub>	15 fF	10 fF
Minimum inverter output capacitance	C <sub>mino</sub>	15 fF	12 fF
On-chip capacitance/unit length	C <sub>inton</sub>	440 fF/cm	150 fF/cm
On-chip resistance/unit length	R <sub>inton</sub>	600 $\Omega/\text{cm}$	1.5 K $\Omega/\text{cm}$

TABLE 5-5. Power Consumption of On-Chip Wires for 0.8  $\mu$ m CMOS.

Wire length (mm)	Energy (pJ)	RC limit	Power at 60 MHz ( $\mu$ W)
1.25	1	> 1 GHz	60
2.50	2	> 1 GHz	120
3.75	3	> 1 GHz	180

TABLE 5-6. Power Consumption of On-Chip Wires for 0.35  $\mu$ m CMOS.

Wire length (mm)	Energy (pJ)	RC limit	Power at 60 MHz ( $\mu$ W)
1.25	0.4	> 1 GHz	24
2.50	0.8	> 1 GHz	48
3.75	1.2	> 1 GHz	72

TABLE 5-7. Performance of MCM Connections.

Line Length (cm)	1995			2000		
	Energy (pJ)	Max. Freq. (MHz)	Power (mW) 200 MHz	Energy (pJ)	Max. Freq. (MHz)	Power (mW) 300 MHz
1	58	390	12	8.1	740	2.5
5	108	320	22	14.7	555	4.4
10	170	265	34	22.8	424	6.9
15	233	225	47	31	343	9.3

From Table 5-7 we can see that the expected improvement in performance for MCM technology over the next five years is significant. At a given line length, the power figures are expected to drop by almost an order of magnitude while the maximum frequency of operation will almost double for lines below 10 cm. However, for large area MCMs with line lengths of 15 to 20 cm or above, the maximum frequency of operation of the interconnection will remain limited to about 300 MHz.

## Optoelectronic interconnections

Here we provide an estimate of the power consumption of an optoelectronic link. The detectors are assumed to be PIN diodes and the receivers are transimpedance circuits where the number of stages is optimized for electrical power vs. optical power trade-off. The transmitters are either VCSELs or MQW absorption based modulators. The driver circuits are based on a super-buffer design<sup>(5-15)</sup> which is a geometrically staged cascaded buffer circuit, designed to drive large capacitance loads with minimum signal delay. For MQWs, this design reduces to a single large inverter due to the low capacitance of an MQW diode, typically 35 to 100 fF. In the case of the VCSELs, the drivers must deliver relatively high currents since a laser is modulated between threshold and a high current value for maximum speed. The main drawback of both receiver and driver designs in terms of performance is that they have a high DC power consumption (except for the MQW drivers).

In Table 5-8, several types of transmitters and their associated circuits are evaluated in a 4096 channel system configuration and the corresponding power consumption per channel is provided. The transmitters are VCSELs with 1 mA or 100  $\mu$ A threshold current and  $20 \times 20 \mu\text{m}^2$  MQW modulators.<sup>(5-16)</sup> Depending on the architecture and implementation of the optical interconnect system architecture, different loss factors will be involved. Here we based our calculation on the OTIS system, since it will be the interconnect system that is used in the optoelectronic approaches.

In Table 5-9, we project the performance of the optoelectronic link if 0.35  $\mu\text{m}$  CMOS technology is used for the driver and receiver circuits. In Table 5-8 and Table 5-9, the numbers in parenthesis for the receiver columns indicate the number of stages in the transimpedance receiver circuit. The optical power column indicates how much laser power is delivered by the VCSELs or how much optical power is required for the external laser for the MQW modulators. Finally, the number in parenthesis in the power per channel column indicates the total power required per modulator including their share of the power consumed by the external laser. In the following, we will assume that either VCSELs or MQW modulators can be operated at 600 MHz. This yields a link budget of about 2 mW and a total power consumption of about 9 W for 4096 channels. Note that MQW modulator technology is readily available, while further development is required for low threshold VCSELs. The choice between transmitter technology will be decided based on scalability issues, i.e. which technology will accommodate faster links, and packaging issues. At present, it appears that VCSELs may quickly become a better candidate since their speed will not be as limited as modulators and they do not require an external laser source. However, based on the numbers in Table 5-7, Table 5-8, and Table 5-9; it is critical for the ultimate success of FSOI to develop VCSELs with low threshold power integrated in 2-D arrays and suitable for flip-chip bonding.



TABLE 5-8. Power Consumption of an Optoelectronic Link for 0.8  $\mu\text{m}$  CMOS.

0.8 $\mu\text{m}$ CMOS for 4096 channels	Receiver Power	Transmitter Power	Optical Power	Power per Channel
VCSELs 1 mA				
60 MHz	8.7 W (1)	11.2 W	0.5 W	4.9 mW
600 MHz	29.8 W (3)	18.6 W	4.5 W	11.8 mW
VCSELs 100 $\mu\text{A}$				
60 MHz	8.7 W (1)	2.0 W	0.5 W	2.6 mW
600 MHz	29.8 W (3)	9.4 W	4.5 W	9.6 mW
MQW, 5V, 20x20 $\mu\text{m}$				
60 MHz	8.7 W (1)	0.1 W	1.5 W	2.2 mW (3.3)
600 MHz	38.0 W (4)	1.4 W	3.9 W	9.6 mW (12.5)

TABLE 5-9. Power Consumption of an Optoelectronic Link for 0.35  $\mu\text{m}$  CMOS.

0.35 $\mu\text{m}$ CMOS for 4096 channels	Receiver Power	Transmitter Power	Optical Power	Power per Channel
VCSELs 100 $\mu\text{A}$				
60 MHz	2.0 W (1)	2.2 W		1.0 mW
600 MHz	6.0 W (3)	3.6 W		2.3 mW
MQW, 5V, 20x20 $\mu\text{m}$				
60 MHz	2.3 W (1)	0.1 W	1.0 W	0.5 mW (0.8)
600 MHz	8.0 W (4)	0.8 W	4.0 W	2.2 mW (3.1)

If we compare the results of the link analysis, it becomes clear that optics offer significant advantages in terms of performance. Note that even with projected ceramic materials the interconnection speed of MCM does not scale well. In fact, the situation is worse for electronics than our optimistic projections predict, as demonstrated by the Semi-conductor Industry Association Roadmap that predicts that off-chip interconnects will be limited to 250 MHz at the year 2001. Optical interconnects can easily scale this number up to 600 MHz or more with

presently available devices. Optics can therefore match the predicted on-chip clock speeds and optically interconnected chip sets will be able to operate at single chip speeds. In terms of power dissipation optics also offers an advantage. This is especially true if one considers the fact that we have neglected performance degradation resulted from vias and corner turns in MCMs. Also, we used presently available OE device parameters for optoelectronic link power calculation while we used projections for the year 2000 for estimating the power consumed in electrical links. It should also be noted that the optical interconnects link budget were calculated based on the OTIS interconnection architecture that provides a good interconnection power efficiency. We should therefore caution that the above results cannot be generalized for any optical interconnection scheme. Nevertheless, we can conclude that optical solutions offer a power-delay product per link advantage exceeding a factor of 10 at 250 MHz. We will next describe the OTIS architecture and discuss its usefulness in the context of FFT interconnects.

#### **5.3.1.1.5 OTIS Approaches**

In general, a 2-D implementation of multistage interconnection networks based on bounded degree networks require a transpose operation to be embedded in the circuit. The usefulness of the transpose interconnection for global connectivity is therefore obvious in the context of a 2-D FFT computation. The transpose operation however, is challenging to implement in electronics since it requires global data movements over long interconnection distances. On the other hand an optical implementation can be quite straightforward.

Figure (5-8) shows a case where OTIS is used for bit-serial communication. In this case  $N \times N$  PEs are arranged in  $\sqrt{N} \times \sqrt{N}$  groups in the input plane. Each PE has a transmitter/receiver pair and via OTIS, each PE of a given group in the input plane is connected to one given PE in each group of the output plane. Since this system is symmetrical with respect to the vertical axis in the middle of the optical system, it can be easily folded onto itself by placing a mirror along that axis. In this case, the input and output planes become the same, and global communications is established on the PE plane.

Alternatively, Figure 5-9 illustrates the case where OTIS is used for bit-parallel communication. In this case, each PE in plane 1 on the left has a transmitter/receiver pair for each bit of it's parallel output. OTIS maps optically the bit outputs of one PE to different groups in plane 2 on the right. If each group on the right is a crossbar equivalent electronic switch, then all the bits can be routed identically by these switches as illustrated in Figure 5-9. OTIS maps the switched bits back onto plane 1 on the left, and all the bits end-up on the detector inputs of a single PE. Note that the switches in plane 2 on the right are local and very simple and can all be controlled via a single centralized controller since they all switch the same way at any given time.<sup>(5-17)</sup> This system provides full routing (crossbar equivalent switching) in a two-pass, single-stage optoelectronic system.

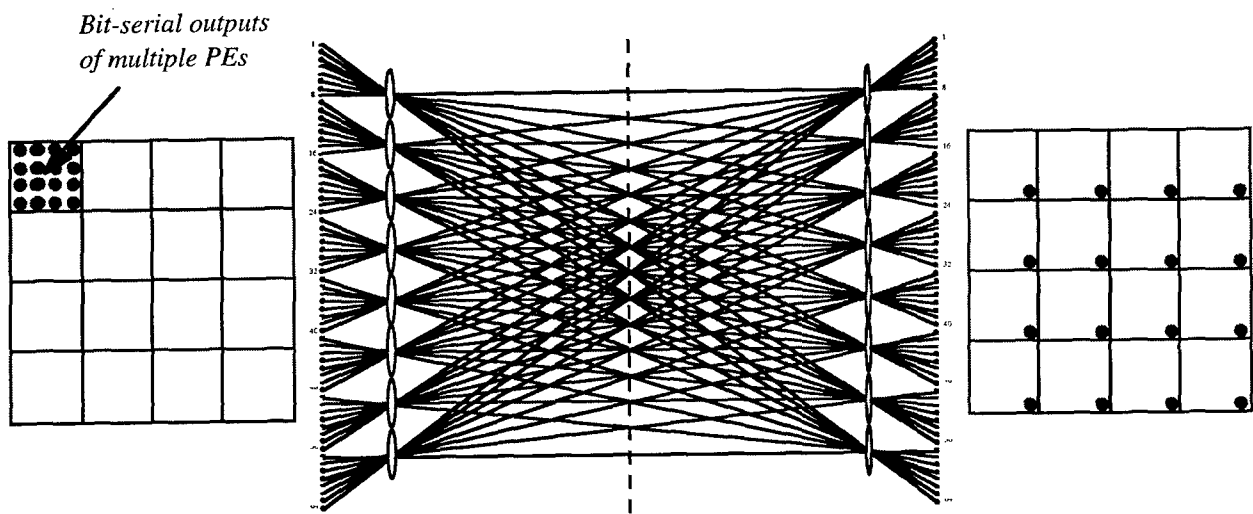


Figure 5-8. OTIS for a bit-serial connection between PEs.

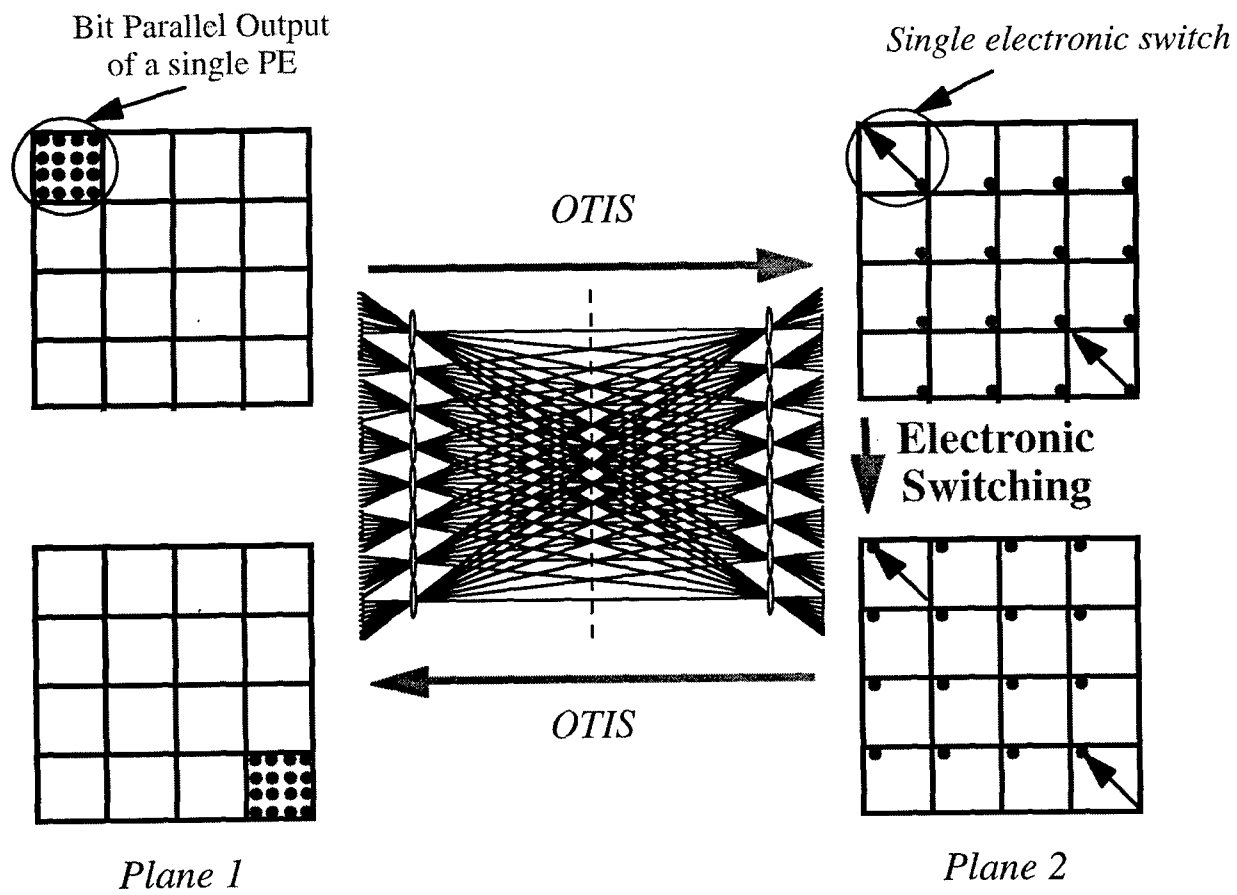


Figure 5-9. OTIS for a bit-parallel communication between PEs.

### **5.3.1.2 Optoelectronic Approach**

In this section, we first describe two optoelectronic system architectures that remove the roadblocks and limitations outlined previously. We evaluate their potential performance and compare them to all electrical approaches based on MCM technology.

#### ***5.3.1.2.1 Optoelectronic Systems Configurations and Performance***

The optoelectronic approaches for a parallel FFT machine are based on optimally combining electronics technology with free-space optical interconnection technology. In order to select a good potential parallel optoelectronic implementation of an FFT machine, we have analyzed several possible implementations in terms of performance over cost. Namely, we have looked at throughput versus power consumption for all the operations involved in the FFT computation for various technologies and system implementations. These operations include the data input, the memory to processor connections, the processor to processor connections, the processor computations, and the data output.

In the following, we show the performance and cost analysis of two different optoelectronic systems for FFT computations. The first one is based on custom silicon chips interconnected via the Optical Transpose Interconnection System (OTIS) based system. In this case, I/O and communication to the chips are performed in a Word-Parallel/Bit-Serial fashion. The second system uses Commercial Off-The-Shelf (COTS) chips which are also interconnected via an OTIS based system. In this case, however, I/O and communication between chips is performed in a Word-Parallel/Bit-Parallel way.

In the following, the two systems are evaluated for performing  $1024 \times 1024$  2-D complex to complex FFTs on 32 bit word precision. It is assumed that light transmitters and detectors are flip-chip bonded to silicon and are interconnected using a free-space optical system. In our calculations, we have assumed that the optical interconnect system supports 4096 channels and consists of two planes of diffractive lenslet arrays and the additional optics required to illuminate Multiple Quantum Well (MQW) modulators. Although for this report we have assumed that the system utilizes MQW modulators, it can be equally well implemented using optical sources such as Vertical Cavity Surface emitting Lasers (VCSELs) flip-chip bonded to the chips, in which case the optical system may not require an external laser and additional illumination optics.

##### **5.3.1.2.1.1 Bit-Serial / Custom-Electronics approach**

In the Bit-Serial approach, an electronics plane consists of an  $8 \times 8$  array of custom chips where each chip consists of an  $8 \times 8$  array of Processing Elements (PEs) for a total of  $64 \times 64$  (4096) PEs. Each PE consists of an FPU that performs the required complex multiplications and additions. Each PE also contains the necessary memory to store the data and program required for performing the FFT. The amount of memory required per PE to map a  $1024 \times 1024$  FFT onto the  $64 \times 64$  PEs is 16 Kbits for data storage, and performing the FFT algorithm will require an additional 16 Kbits

for program/workspace. Also, each PE has an optical Transmitter/Receiver pair and six 32-bit wide on-chip electrical channels for communicating with other PEs. The on-chip connections form a hypercube among the 64 PEs of each chip. Figure 5-10 shows a schematics of this approach.

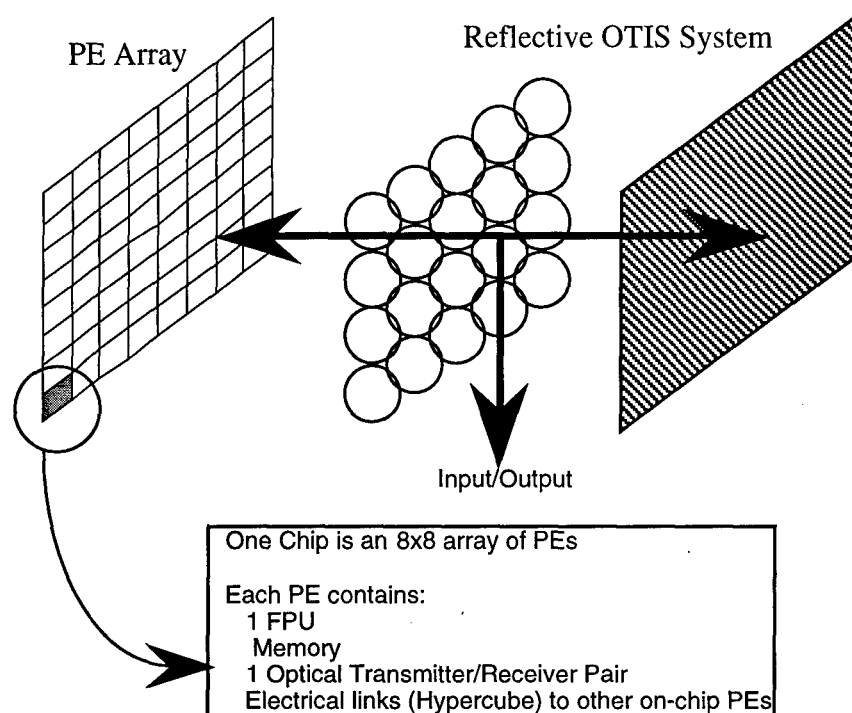


**Figure 5-10. Bit-Serial / Custom Electronic chips approach.**

We first designed a 64-bit FPU optimized for computing higher-radix butterflies for the optoelectronic FFT architecture. The design was laid-out for 0.8 and 0.5 micron CMOS technologies available from MOSIS. We also estimated the performance of the design with a 0.35 micron CMOS process. Table 5-10 summarizes these results. The FFT Processing Unit (FPU) is a computational engine that performs the complex mathematical operations required for the calculation of an FFT. Broken down into primitive operations, the FFT is just a series of multiplications, additions, and subtractions. The FPU can perform the multiplication of two complex numbers, as well as the addition and subtraction of two complex numbers. Furthermore, it can mix the operations of addition and multiplication or subtraction and multiplication. Finally, building on the operations mentioned above, it can achieve a multiply-accumulate function which is heavily used in higher-order radix FFT implementations.

The FPU is composed of a data storage unit and an arithmetic unit. The data storage unit is a 512x64 high-speed SRAM. This is used to store the initial data values, and the intermediate calculation results as necessary. The arithmetic unit contains a complex multiplier, a complex adder/subtractor, and some scratchpad storage registers. All of these components are connected by a 64-bit data bus which represents the size of each data word. Each data word is a complex number

with a 32-bit real part and a 32-bit imaginary part. The adder/subtractor unit is a block that is composed of a 64-bit high-speed adder, a column of inverters, and a multiplexer. Two complex numbers are added when the multiplexer is set to pass the non-inverted data straight to the adder input. In a binary system, subtraction can be achieved by adding an unchanged number to the 2's complement of another number. Subtraction is performed in the adder/subtractor unit when the data to input A is inverted and the Carry In bit is set to a '1' to form a 2's complement addition. During normal addition, the Carry In bit is set to '0'. The sum or difference is then stored in a register.

**TABLE 5-10. Design Parameters of the FPU and Memory for the Bit-Serial/Custom-Chip Optoelectronic Approach.**

	0.8 $\mu$ m CMOS	0.5 $\mu$ m CMOS	0.35 $\mu$ m CMOS
<b>Technology</b>	<b>MOSIS HP26G</b>	<b>MOSIS HP14B</b>	<b>Projected</b>
<b>Supply voltage</b>	5V	3.3V	3.3V
<b>Area (Overall)</b>			3 mm <sup>2</sup>
<b>Area (Logic)</b>	7 mm <sup>2</sup>	1.6 mm <sup>2</sup>	0.95 mm <sup>2</sup>
<b>Area (32 Kbits SRAM)</b>	1.6 mm x 2 mm	1.2 mm x 1.6 mm	2 mm <sup>2</sup>
<b># of transistors (Overall)</b>	268,000	268,000	268,000
<b># of transistors (SRAM)</b>	200,000	200,000	200,000
<b># of transistors (Logic)</b>	68,000	68,000	68,000
<b>Power consumption</b>	725mW	407mW	229mW
<b>Clock speed</b>	100MHz	150MHz	200MHz
<b>Time to compute radix-16 butterfly</b>	4.8 $\mu$ sec	3.2 $\mu$ sec	2.4 $\mu$ sec

The complex multiplier decomposes the multiplication of two complex numbers as follows:

$$\text{PROD} = (\text{Br} + j\text{Bi}) * (\text{Wr} + j\text{Wi})$$

$$\text{PROD} = (\text{Br} * \text{Wr} - \text{Bi} * \text{Wi}) + j(\text{Br} * \text{Wi} + \text{Bi} * \text{Wr}) \quad (5-18)$$

Therefore, the multiplier unit consists of four 32-bit  $\times$  16-bit multipliers and two 32-bit adders. The output of the multiplier unit is a 64-bit combined real and imaginary number.

Additional technology assumptions were made in order to evaluate this optoelectronic approach:

*An on-chip wire needs to be at least  $4\lambda$  wide and spaced apart by  $3\lambda$ , where  $\lambda$  is half the CMOS feature size.*

Thus, for a CMOS feature size of  $0.35\ \mu\text{m}$ , each wire and associated spacing occupies a width of about  $1\ \mu\text{m}$ . Because the PEs are laid out as a hypercube, each PE is connected to  $\text{Log}N$  other PEs. This yields a total connection length requirement per PE of  $2 \times N^{1/2} \times \Delta$  where  $\Delta$  is the PE spacing, each connection is 32 bits wide, and each of these 32 wires is bi-directional. Each wire requires electrical transmitter and receiver circuits. Each PE also requires an optical transmitter/receiver pair and their associated circuits operating at 600 MHz. The area and energy requirements of these components are given in Table (5-11). Note that these values are only approximations but provide insight about the technology capabilities and trade-offs. Under these assumptions, one of the custom chips (8x8 PEs) is estimated to occupy a little  $1\ \text{cm}^2$  die. For a 60 MHz clock speed this yields about 5 W power consumption and  $5\ \text{W}/\text{cm}^2$  power dissipation while for 600 MHz these numbers become about 50 W and  $50\ \text{W}/\text{cm}^2$  respectively. These figures are dominated by the FPU and electrical wires which account for over 90% of both power and area requirements. For the entire system that consists of 64 such chips, the power consumption becomes 320 W for a 60 MHz clock and 3.2 KW for a 600 MHz clock.

**TABLE 5-11. Summary of Area and Power Requirements of the Various System Components.**

Component	Area	Energy/Power
FPU	$1\ \text{mm}^2$	
Optical Trans./Rec.	$50 \times 50\ \mu\text{m}^2$	—
On-chip memory	$1\ \mu\text{m}^2 / \text{bit}$	$.01\ \mu\text{W} / \text{bit}$
On-chip wires	$1\ \text{mm} \times 1\ \mu\text{m}$	—

The FFT is computed using 8- and 16-point FFT building blocks used in row-column fashion and combined in a mixed-radix algorithm. The idea here is to use large radix building blocks, as they involve many fewer multiplications at the cost of more additions. For a  $1024 \times 1024$  FFT on a  $64 \times 64$  PE system, each group of PEs on a chip has a  $128 \times 128$  array of values. Each PE starts with a  $16 \times 16$  array of these values. Using the radix-16 FFT block, it computes the FFT of its values using a row-column approach, which we define as a “16-point main block.” Then, it redistributes its data across the processors in its group. In the next step, each processor's 256

values can be thought of 4  $8 \times 8$  blocks, and 8-point transforms, called 8-point main block will be used on them (this is because  $128 = 16 * 8$ ). At this point, a  $128 \times 128$  2-D FFT has been performed on the values in each group. Then, the optoelectronic OTIS-based shuffle performs the next reorganization, a transpose of the data, and the process is repeated again.

The time required to perform a radix-16 FFT block can then be calculated. It requires 148 additions and 20 multiplications, which is equivalent to 1740 clock steps or 29  $\mu\text{sec}$  at 60 MHz and 2.9  $\mu\text{sec}$  at 600 MHz. The time for a 16-point main block is then  $16 \times 29 = 464 \mu\text{sec}$  or 46.4  $\mu\text{sec}$  respectively. Under these assumptions, the run-time of a  $1024 \times 1024$  complex to complex valued FFT as described in the previous paragraph can be estimated. At 60 MHz, we find that the total time is about 4.5 msec with 4.1 msec compute time, 0.3 msec electrical connect time, and about 0.1 msec optical connect time where compute time is consumed only in the FPU, electrical connect time is spent communicating on-chip, and optical connect time is spent for I/O and communications between chips. At 600 MHz, the total time becomes 0.5 msec with a breakdown of 0.41, 0.03, and 0.11 msec for compute, electrical connect, and optical connect respectively. Thus, by using optics, the interconnect times have become negligible and the overall speed remains limited by the electronic computations in the FPU. This is an important conclusion that indicates that this approach will remain viable even with improving electronics. The results of the Bit-Serial/Custom-Electronics approach are summarized in Table 5-12.

**TABLE 5-12. Performance Results for the Bit-Serial/Custom Chips Optoelectronic FFT Approach.**

<b>1024x1024 FFT</b>	<b>60 MHz clock</b>	<b>600 MHz clock</b>
<b>Total Time (msec)</b>	<b>4.5</b>	<b>0.5</b>
Compute Time	4.1	0.41
Electrical Connect Time	0.3	0.03
Optical Connect Time	0.11	0.11
<b>Total Power (W)</b>	<b>269</b>	<b>2600</b>
FPU Power	246	2460
Electrical Connect Power	13	130
Optical Connect Power	10	10
<b>Power Density (W/cm<sup>2</sup>)</b>	<b>4.2</b>	<b>41</b>



Important conclusions can be derived from the evaluation of this configuration:

- This configuration allows 1,000 frames per second with no latency (assuming about 300 MHz clock rate). However, at high speeds, the required power is large, consumed mainly by the FPU's and on-chip electrical connections. Note that the power required for the optical interconnects is essentially negligible compared to the other system components at high speed.
- The speed of the electronics (FPU's) is the main limiting factor in the system. Thus, better ways of implementing the FPU's must be developed. However, as can be seen from Table 5-12 the power densities reached for fast silicon chips become rapidly unmanageable. Thus, faster technologies with good power delay products should be targeted: low-voltage CMOS or GaAs complementary FET technology (if made practical) would be good candidates at this point.
- Optics is essentially free in terms of power and performance.

In the previous estimates, one of the assumptions was that an FPU can perform a complex addition in 5 clock cycles and a complex multiplication in 50. To further improve the performance of the Bit-Serial approach, let us consider a case where the FPU can perform these operations in 1 and 10 clock cycles respectively. This is a difficult assumption to justify since such FPU's tend to be very large in area and would lead to a Bit-Serial/Custom chips implementation that might not be realistic. In this case, the total time for performing a  $1K \times 1K$  FFT becomes 1 msec (60 MHz clock) and 0.16 msec (600 MHz clock) respectively. Therefore, the performance goals can be achieved even for a fairly low system clock speed.

At this point, it should be emphasized that the optoelectronic interconnect technology does not solve all aspects of the parallel FFT implementation problem but only removes the interconnect roadblock making room for aggressive electronic VLSI technologies.

#### 5.3.1.2.1.2 Bit-Parallel / Commercial-Off-The-Shelf chips OE approach

In this approach, the electronics plane consists of an  $8 \times 8$  array of Commercial-Off-The-Shelf (COTS) DSP or FFT chips. Also, a switching plane of  $8 \times 8$  routing chips will be used, and free-space optics will be utilized to connect the two planes. The switching plane will consist of either OTIS hypercubes, crossbar chips, or cyclic shift circuitry. The OTIS system that connects the processing plane to the switching plane will be used in a Bit-Parallel fashion for interconnections (Fig. (5-11)). Each processor chip is now given a  $128 \times 128$  sub-image (= 16K word-pairs) of the image.

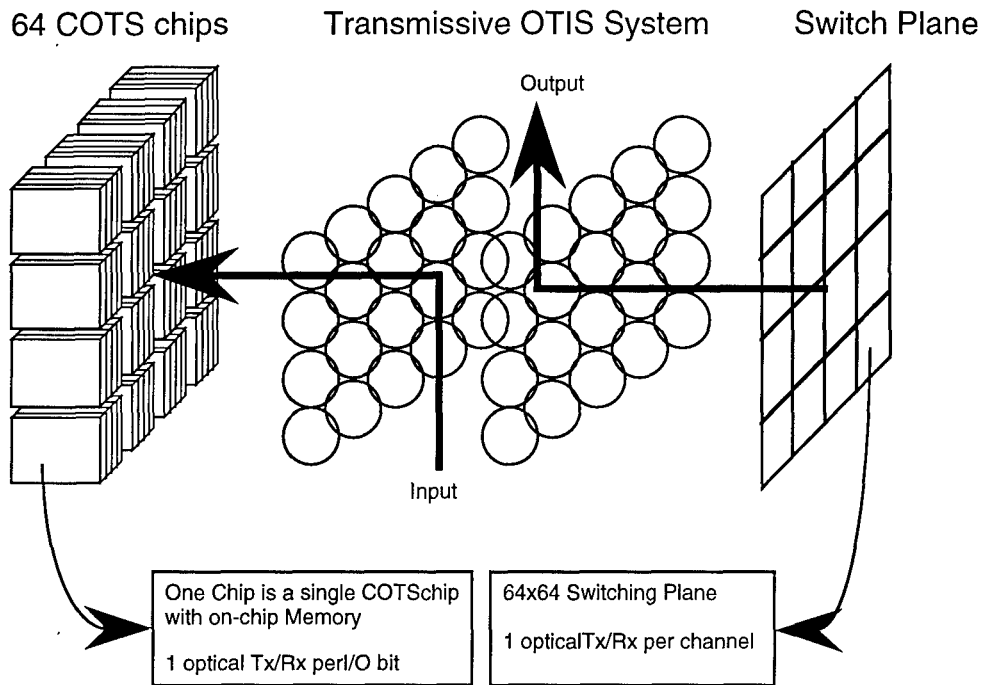


**Figure 5-11. Bit-Parallel / COTS chips approach.**

Two assumptions need to be made in order to evaluate the performance of such system. First it is assumed that an arbitrary  $N$  point 2-D FFT can be computed as fast as an  $N$  point 1-D FFT on the processing chip. It is also assumed that the time required for an  $N$  point FFT scales as  $N \log N$  as  $N$  grows. Second, it is assumed that the routing in the switch plane can be performed at the same speed as the processing chip clock. This last assumption is fair since DSP or dedicated FFT chips have reasonable clock speeds and switch planes operating at speeds of 200 MHz have already been demonstrated.<sup>(5-17)</sup> In this second optoelectronic approach we consider several DSP and FFT chips for which the performance is described in the literature.<sup>(5-9,5-18)</sup>

To perform the 2-D  $1K \times 1K$  FFT, data is first loaded on the 64 chips, where each chip receives a  $128 \times 128$  data block. The FFTs of the  $128 \times 128$  data blocks are computed locally on each of the chips. For the chips we consider, this is done in the time required for computing the equivalent 32  $1K$ -point 1-D FFTs. Data is redistributed among the chips by using the Bit-Parallel OTIS system. Another set of local FFTs on  $128 \times 128$  data blocks is then performed and the data is finally output. The chips we consider are the same as described in Section 5.3.1.1.2. The first two have enough on-chip memory to store the required  $128 \times 128$  data block while for the others, external memory chip(s) will be required. Note that in the case of the Plessey system these memory chips are included in the chip-set. We assume that the cost in terms of performance for adding these memory chips has little effect. Indeed, with the rapid progress in DRAM and SRAM technologies and by utilizing parallel RAM banks in a pipelined fashion the access time to these devices can be essentially neglected. In any case, we will do the same assumption later when evaluating the

potential performance of an MCM based implementation. Table 5-13 summarizes the results of the Bit-Parallel/COTS approach.

**TABLE 5-13. Performance Results for the Bit-Parallel/ COTS Chips Optoelectronic FFT Approach.**

<b>1024x1024 FFT</b>	<b>ADSP21060</b>	<b>C80</b>	<b>Plessey</b>	<b>Future Chip</b>
<b>Total Time (msec)</b>	<b>18.2</b>	<b>8.5</b>	<b>6.6</b>	<b>0.70</b>
Compute Time	14.9	5.2	3.2	0.26
Optics I/O Time	1.6	1.6	1.6	0.22
Optics Connect Time	1.6	1.6	1.6	0.22
<b>Total Power (W)</b>	<b>296</b>	<b>706</b>	<b>770</b>	<b>581</b>
Compute Power	230	640	704	384
Switch Power	64	64	64	192
Optics Power	2	2	2	5
<b>Chips Cost (\$)</b>	<b>16,000</b>	<b>25,600</b>	<b>192,000</b>	<b>N/A</b>

As was the case in the previous optoelectronic approach, the systems based on existing chips are very largely dominated by the computation time and power requirements. It can also be observed that performance can be increased by using more computationally efficient chips at the expense of system power and system cost. One sure way to achieve the 1K×1K 1,000 frames per second performance is to utilize future FFT chips specially designed for providing orders of magnitude improvements in computation for reasonable power figures. Today, such chips may be impractical, however, with evolving feature sizes, they may become viable within the next five years. Thus it is critical to start investigating means by which the interconnect roadblocks can be removed in systems that use these chips. Another important factor to consider is that when using COTS chips the I/O to and off the chips is limited due to power considerations as they are designed to be assembled as single chips in standard packages and must drive large I/O pins. For example, the existing chips have an I/O bandwidth of 40 MHz, 32 bits wide while it is projected that the future generation FFT chip I/O bandwidth will be 150 MHz, 64 bits wide. Thus, this explains while in Table 5-14 the Compute, I/O and Connect times are essentially of the same order with the future generation FFT chip. Alternatively, in the Bit-Serial/Custom-Electronics design the I/O could be tailored to the optics capabilities and was not limiting the system's performance.

### **5.3.1.2.2 Why Not More Optics?**

One of the conclusions of the system analysis previously presented is that the optoelectronic technology allows fast inter-processor communication at essentially no cost in terms of power. Based on this conclusion, one could think that the Bit-Serial/Custom-Electronics system could be designed to use more optoelectronics and that the overall performance could therefore be improved. However, by utilizing parallel electrical paths between the PEs on a chip, rather than serial optical links, the system speed is optimized at the expense of a larger electrical power consumption. If serial optical links were used instead, the power consumption of the connections could be reduced but this would occur at the expense of system speed. Since the main source of power consumption in the system is due to the FPUs, this would not bring any significant power savings but would slow down the system. Alternatively, more optical links could be used to keep the inter-PE connections on a chip parallel. In this case, the cost in terms of numbers of transmitters and receivers would jump to large values (over 750,000: 6 connections per PE with 32 bits wide for  $64 \times 64$  PEs) and the additional complexity of the optics and related reliability issues would essentially make the system impractical.

Alternatively, a system design that uses more serial optical links between more optoelectronic PEs could be envisioned. This approach would essentially allow us to remove all electrical connections between PEs and reduce the memory requirements per PE. However, as the size of the FFT problem grows this hardware approach would become rapidly unmanageable. For example assuming that an FPU area is  $1 \text{ mm}^2$ , the total silicon area required would be  $1 \text{ m}^2$  for the  $1024 \times 1024$  FFT, which is very unrealistic. The number of receivers and transmitters would also grow and create problems of its own in terms of packaging, available optical power and optical system. Thus, it seems that the approaches described above represent a good compromise in terms of hardware complexity and feasibility vs. performance and power consumption.

### **5.3.1.2.3 Why Not More Electronics?**

One way to justify that optoelectronic systems are worthwhile developing is to compare them to a potential all electrical implementation based on MCM technology. Both the Bit-Serial/Custom-Electronics and the Bit-Parallel/COTS chips options could be built with MCM technology. The required wire lengths on the MCM can be calculated based on the chip areas and their minimum spacing on the MCM using Manhattan distances. Then, their power consumption can be derived for existing and projected MCM technologies. For each one of these implementations there is a minimum FFT size and clock rate that justifies the use of optoelectronics as the off-chip interconnect technology of choice.

#### **5.3.1.2.3.1 Bit-Serial/Custom-Electronics approach**

In this case we use the same FPU chips as described before. The chips are about  $1 \text{ cm}^2$  and each chip contains 64 PEs; the chips are built using  $0.35 \text{ }\mu\text{m}$  technology. Each chip has a serial

connection to all the other chips which yields 4096 total connections. In addition power, ground and various control signals need to be routed to all the chips. Note that as opposed to the optics case the I/O of data to the chips might be quite difficult to implement since it will require additional demultiplexer circuits to route the correct image data to the chips. Based on the parameters described before and omitting the required demultiplexing circuits for I/O, the following MCM performance can be estimated (see Table 5-14). All the wire lengths are calculated based on the chip areas and their minimum spacing on the MCM. Then, their power consumption can be derived for existing and projected MCM technologies.

**TABLE 5-14. Performance of the Bit-Serial/Custom-Electronics MCM Implementation.**

<b>1Kx1K FFT</b>	<b>1995</b>	<b>2000</b>
<b>Total MCM area (cm<sup>2</sup>)</b>	<b>11.5 x 11.5</b>	<b>9.4 x 9.4</b>
<b>Number of wires per plane</b>	<b>&gt;400</b>	<b>&gt;100</b>
<b>Off-chip maximum frequency of longest line</b>	<b>200 MHz</b>	<b>300 MHz</b>
<b>Off-chip Connect Time (msec)</b>	<b>0.33</b>	<b>0.22</b>
<b>Off-chip Power (W)</b>	<b>70</b>	<b>6</b>
<b>Total Time (msec) @ 60 MHz</b>	<b>4.7</b>	<b>4.6</b>
<b>Total Power (W) @ 60 MHz</b>	<b>330</b>	<b>265</b>
<b>Power Density (W/cm<sup>2</sup>)@ 60 MHz</b>	<b>5.1</b>	<b>4.1</b>
<b>Total Time (msec) @ 600 MHz</b>	<b>0.77</b>	<b>.66</b>
<b>Total Power (W) @ 600 MHz</b>	<b>2660</b>	<b>2600</b>
<b>Power Density (W/cm<sup>2</sup>)@ 600 MHz</b>	<b>41.5</b>	<b>41</b>

From Table 5-14, it is clear that an all electrical system based an MCM implementation of custom chip has a very similar behavior as the optoelectronic implementation described previously. The projected numbers (right column in Table 5-14) are actually almost identical as those of the optoelectronic implementation.

The factors of choice in this case are however fairly clear. First, it can be argued that the feasibility of such a large MCM is questionable. Remember that the area quoted in the table is only for the FPU chips and do not include the I/O chips and unavoidable glue logic that will be required in the system, making the area grow by a significant amount to at least 12x12 cm<sup>2</sup>. Second and

most important, the MCM interconnections are frequency limited to 300 MHz, even with a five year projection. This limitation is in effect due to the drivers which must be impedance matched to the off-chip wire. This puts an upper bound on how fast such a system could run when FPUs become more and more efficient, since in this case, the system will become I/O and interconnect limited. Note that in the case of VCSEL based optoelectronic implementation, this limit is much higher.

#### 5.3.1.2.3.2 Bit-Parallel / COTS-chips approach

To simplify the comparison for this approach we only evaluate the implementation of the system with future generation FFT chips and 5 years projected MCM performance. In this case, the system requires 64 FFT chips which are interconnected to switches in order to establish global communications between all the FPU chips. We assume that the chips are identical to those used in the optoelectronic modeling. Each FFT chip is assumed to have a 32 bit wide I/O port operating at a maximum speed of 150 MHz which is the projected number for such chips. In addition, switching chips are required so that global communications can be established. We assume that four 64-inputs/64-output crossbars can be implemented on a single chip utilizing the same power as the switching plane in the optoelectronic approach. We also assume that each FFT chip requires an additional 1 Mbit memory chip to store the required 64 Mbits of data of a 1024×1024 image along with the required control logic. This yields an MCM that must accommodate 132 chips with 4096 global (FFT chips to crossbars) and 2048 local (FFT chip to memory) wires. Based on the future generation FFT and MCM projections parameters, the performance of the system can be calculated (see Table 5-15).

**TABLE 5-15 Performance of the Bit-Parallel/COTS-chip MCM Implementation.**

<b>1Kx1K FFT</b>	<b>MCM</b>
<b>Area (cm<sup>2</sup>)</b>	<b>14.2 x 15.4</b>
<b>Number of wires per plane</b>	<b>&gt; 200</b>
<b>Off-chip maximum frequency of longest line (MHz)</b>	<b>250</b>
<b>Off-Chip Connect and I/O Time (msec)</b>	<b>0.44</b>
<b>Off-Chip Connect Power (W)</b>	<b>7</b>
<b>Total Time (msec)</b>	<b>.70</b>
<b>Total Power (W)</b>	<b>583</b>

As was the case for the Bit-Serial approach, the numbers indicate that this MCM implementation is very close in performance to the corresponding optoelectronic approach. The main difference is still in the interconnections maximum operating frequency which will be limited

to about 250 MHz on the MCM. However, this has no bearing on the Bit-Parallel/COTS-chip approach that uses the next generation FFT chip since the I/O of that chip is only 150 MHz.

#### 5.3.1.2.3.3 Comparison Summary

Based on the previous discussion, we can conclude that for  $64 \times 64$  transpose and clock rates in excess of 200 MHz (presently), and 300 MHz (in 2000), it becomes interesting to consider an optoelectronic implementation. If larger size transpose or higher clock speeds are desired, the only foreseeable implementation technology remains the optoelectronic interconnects. Beyond, 300 MHz clock rates and  $1K \times 1K$  image sizes, additional limitations are imposed on the memory and system I/O that might also require optical interconnects. These limitations require further studies that we intend to conduct in the near future.

To get the previous results, we have only considered MCMs with series terminated transmission lines. If more speed is needed, different termination schemes (parallel or active) can be adopted. However, these solutions cost power. Our simulations show that a parallel termination brings potentially 30 % more speed for 3 to 5 times more power. In this case optics becomes significantly more power efficient (well over 10 times) for similar or better speeds.

### **5.3.2 Routing and Sorting applications**

Of particular interest of EOCA system is the implementation of interconnection networks to provide for processor to processor communication. The basic interconnect proposed as an integral part of the 3-D computer is the two-dimensional mesh which allows each processor to communicate with either one of four nearest neighbors. This network is important in image processing applications and any other function which exhibits local data dependencies. To broaden the scope of applications of the 3-D computer and expand its capabilities with more powerful communications and high bandwidth I/O, a two-stage electro-optical network (2S-EON) has been proposed.

The purpose of this analysis is to provide a summary of the routing characteristics of the 2S-EON. First, it will be shown that the 2S-EON is an Expanded Delta Network (EDN) and that as such it can perform any permutation in exactly two passes using global knowledge (off-line routing). Bounds on on-line routing are developed by means of mapping a sorting algorithm onto the structure which in turn can effectively emulate the mesh.

#### **5.3.2.1 System Architecture**

There are two distinct sections to the 3-D computer defined here: the wafer-scale 3-D processor array and the global two-stage router/permutation network implemented as an electro-optical hybrid. Figure 5-12 shows a simplified version of the system.

The set of stacked VLSI wafers define the processing elements with functions distributed across the wafers rather than on a single wafer surface. Consistent with this concept, planar

processing connectivity also exists within at least one wafer in the stack. A typical interconnect of this kind would be the two-dimensional grid encountered in typical mesh-connected parallel computers. Because the cost of communications can become an overburden, algorithms that run on a two-dimensional array must exhibit good locality and require communications with nearest neighbors only.

9429-08-011

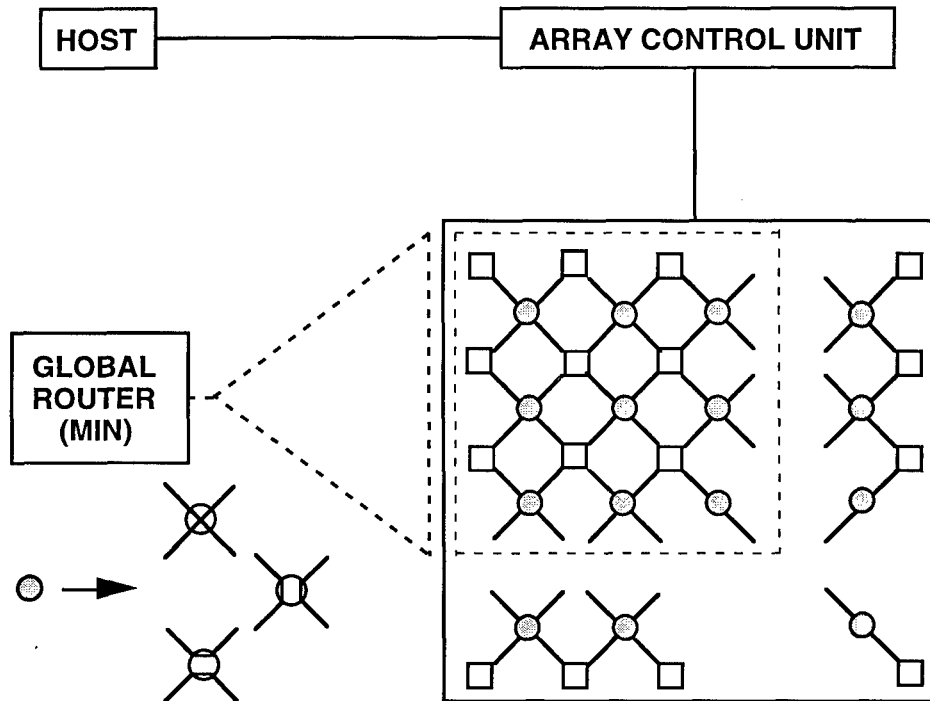


Figure 5-12. A simplified version of a two-stage electro-optical network.

To accommodate scattered communications patterns, a 2S-EON is provided in the enhanced 3-D architecture. This network, as shown in Figure 5-4, is defined below. Its routing capabilities will be analyzed by developing upper bounds relative to its sorting capabilities.

**Definition 1.** The two-stage interconnect consists of a set of  $2n \times n$  ( $n$ -input,  $n$ -output) electronic switches arranged into two columns of  $n$  switches each. Let  ${}_1s_i$  denote the  $i$ -th switch of column 1 and let  $I_k$  represent each one of the  $n^2$  inputs to the network.  $I_k$  connects to input  $j$  of switch  ${}_1s_i$  if, and only if,  $k = in + j$ .

The interconnection between stages is such that output  $i$  of switch  ${}_1s_j$  connects to input  $j$  of switch  ${}_2s_i$ .

Note that according to the definition above, the first stage groups the columns of an  $n \times n = n^2$  array where the grid nodes have been mapped onto an  $n^2$  linear array assuming a row major



indexing scheme. In between stages, the columns are transposed such that each switch of the second stage groups the rows of the same array. The transpose permutation is done by optical means following the natural geometry of lenslets optics. As a matter of convenience, the input transpose permutation can be transferred to the output of the network and thus obtain an equivalent functionality.

### 5.3.2.2 Off-line Permutation Routing

The 2S-EON can be seen as a particular case of the Expanded Delta Network shown in Figure 5-3. Note that the inputs are single wire lines while the interstage interconnect carry many signals simultaneously. Whether the implementation of this bandwidth multiplication mechanism is electrical or optical is a matter of implementation. For the purpose of analysis, they are equivalent. The ratio of high bandwidth interstage connections to the low bandwidth input is called the expansion factor.

9429-08-013

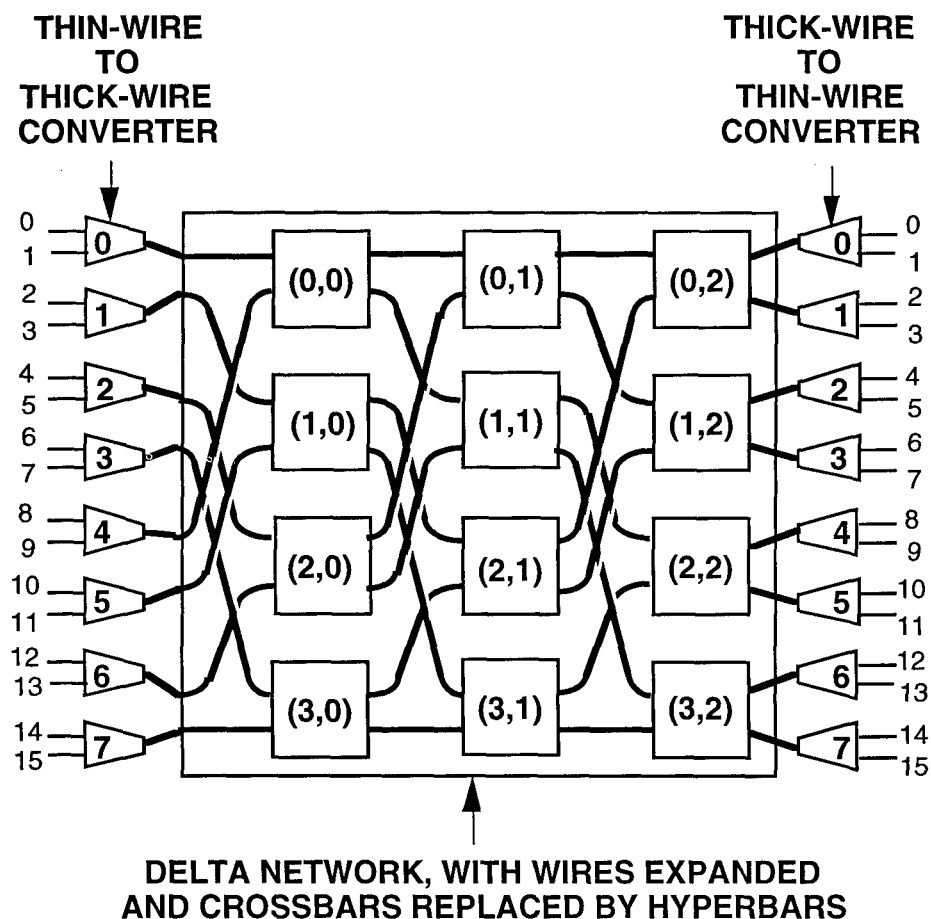


Figure 5-13. The 2S-EON as a particular case of the Expanded Delta Network.

Referring to Figure 5-14, a Delta Network with expansion factor of 1 is shown and used in Figure 5-15 to build a two-pass network (two nets in series). By reduction of the middle two stages to a single less powerful stage the two cascaded networks are shown to behave as a single Clos network. Because it is known that the Clos network can perform any permutation in one pass with global knowledge, the cascaded version of the 2S-EON is capable of the same.

To study on-line routing bounds, one must use other techniques. Because the network naturally maps the Shearsort algorithm, it will be used to derive on-line routing bounds.

9429-08-014

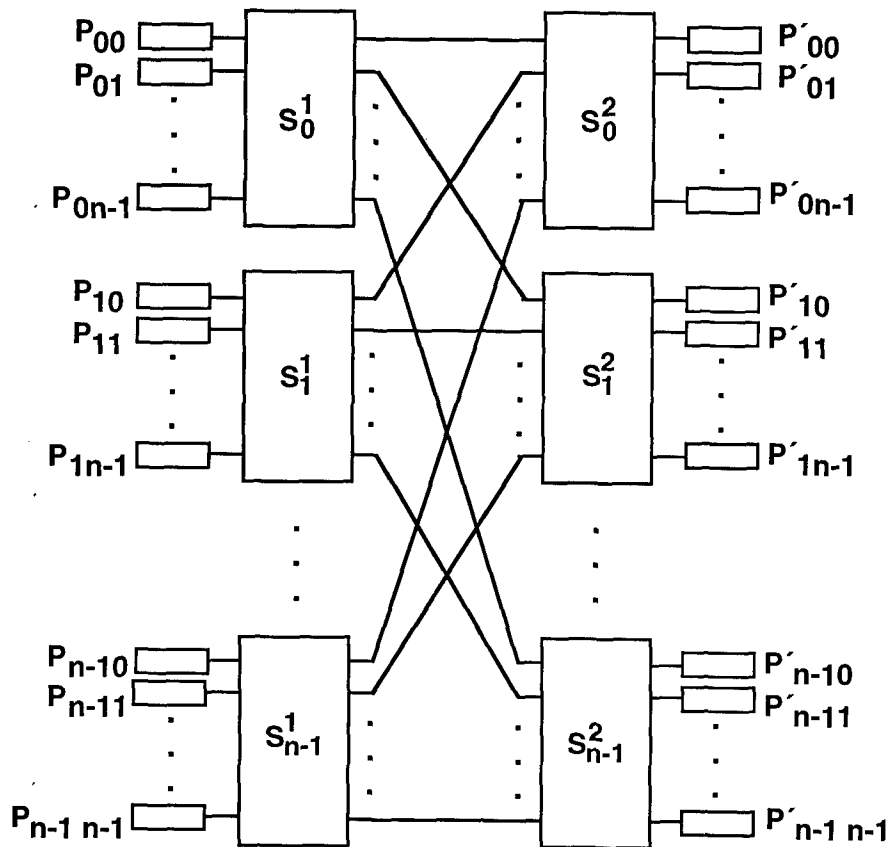


Figure 5-14. Schematic of Delta Network constructed using  $n \times n$  switches.

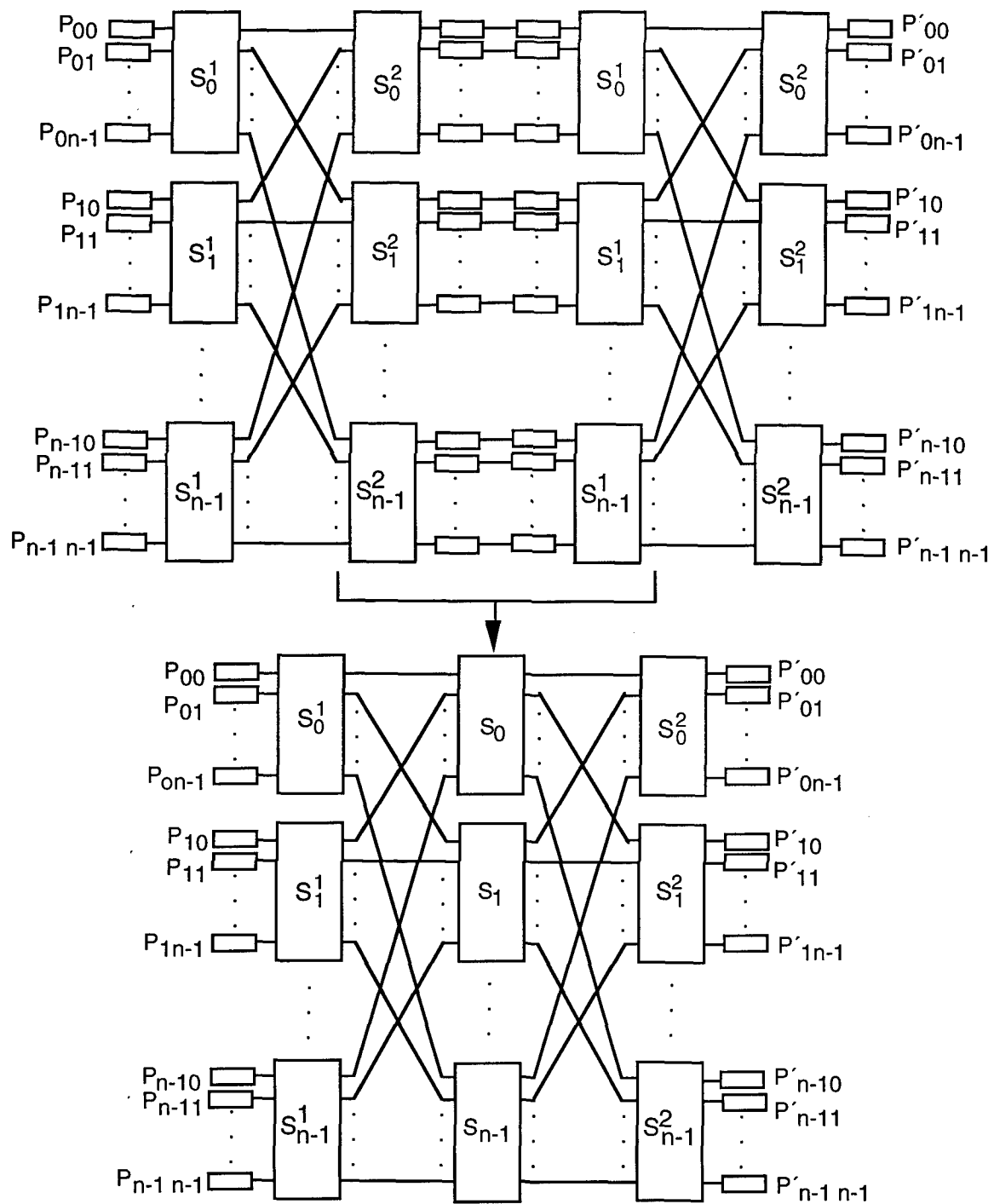


Figure 5-15. With global control, Delta Network is a two-pass network.

### 5.3.2.3 The Shearsort Algorithm

Shearsort is a two-dimensional sorting algorithm for  $n \times n$  arrays like the one shown in Figure 5-16. The basic operation allowed to define the method of computation are given in Figure 5-17.

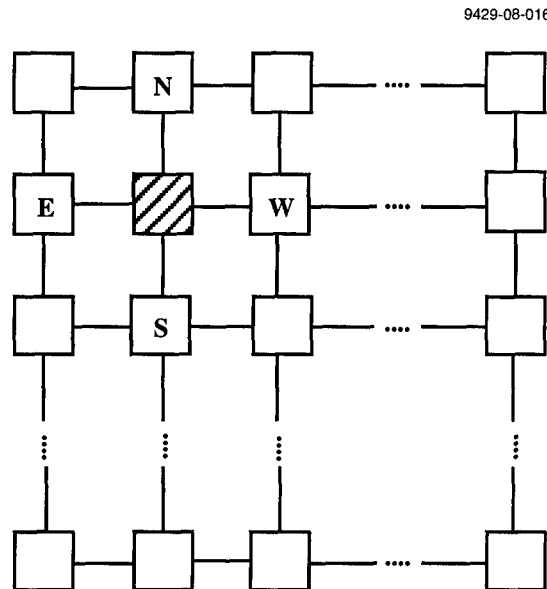


Figure 5-16. Shearsort algorithm: two dimensional computation model for  $n \times n$  array.

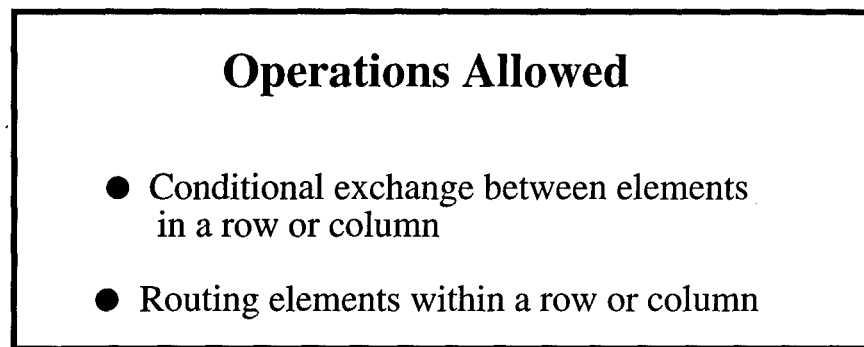


Figure 5-17. The basic allowed operations for the shearsort algorithm.

Given an  $n^2$ -element sequence, shearsort is an iterative algorithm as follows:

**Definition 2.** Shearsort (array  $n \times n$ );

repeat  $\log n$  times

sort all columns in parallel in non-decreasing order from top to bottom

sort all even numbered rows in non-decreasing order from left to right  
 sort all odd numbered rows in non-decreasing order from right to left  
 end repeat

Shearsort can run in a two-dimensional mesh connected array with a total time complexity of  $O(n \log n)$  nearest neighbor compare-exchange operations. To prove this we use the Zero-one principle given in Figure 5-18. Note that when sorting the columns of a row-sorted  $2 \times n$  array, one row will become clean with all zeros (ones) while the other will remain dirty (a combination of 0s and 1s, Figure 5-19). When pairs of rows are thus sorted in the  $n \times n$  array and the column sort is carried out to completion, the 1-clean rows fall to the bottom of the array while the 0-clean rows float to the top of the array. Thus, exactly half of the array is cleaned at every shearsort iteration. This completes the proof outlines as a sorted array in one with only clean 0-rows on top, clean 1-rows at the bottom and a single sorted dirty row separating them.

A typical embedding for shearsort is shown in Figure 5-20. Note that the structure is reminiscent of the 2S-EON and shearsort can be easily mapped into the two-stage electro-optical network, if the switches are capable of sorting  $n$ -element sequences. In Figure 5-21 such an example is given and a recursion used to determine the number of  $2 \times 2$  switch stages needed for the network to sort.

If sequential sorting is assumed, the total sorting time in the network is  $O(n \log^2 n)$  compare-exchange operations. However, if each switch is implemented as a bitonic sorting network, then the total sorting time would become  $O(\log^3 n)$ .

The importance of the timing results above lies in the fact that routing is a subproblem of sorting, and the sorting complexity of any network is an upper bound for routing. Hence, if the two-stage electro-optical network is implemented with intelligent switches capable of some processing, routing can be effected in  $O(n \log^2 n)$ . However, if the network is implemented with only two-by-two switches arranged such that each switch of the two-stage network is an  $n$ -input bitonic network, then routing would become a  $O(\log^3 n)$  operation.

#### ZERO-ONE PRINCIPLE

If a network with  $n$  input lines sorts all 2 sequences of 0's and 1's into non-decreasing order, it will sort any arbitrary sequence of  $n$  numbers into non-decreasing order.

Figure 5-18. Zero-One principle.

0	0	0	0	0	0	1	1	1	1
1	1	1	1	1	1	1	0	0	0

(a)

0	0	0	0	0	0	1	0	0	0
1	1	1	1	1	1	1	1	1	1

(b)

Figure 5-19. Proof using the [0,1] principle: The first row is sorted from left to right and the second from right to left. The actual number of 0's and 1's is irrelevant. After the column sort one of the two rows will contain only 0's or only 1's depending on the actual number of 0's and 1's. In the most favorable case, when both are equal, we will have both rows 'clean'.

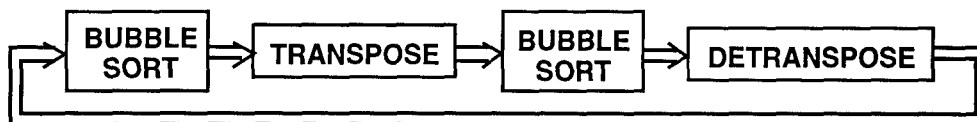
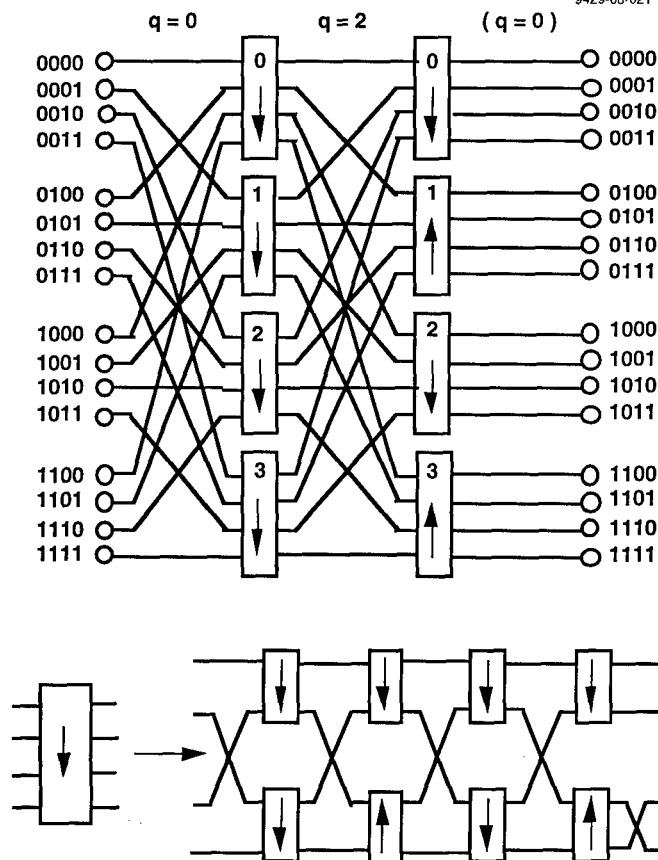


Figure 5-20. Typical embedding for shearsort:  $O(\log n)$  passes through the network will produce a sorted sequence.



$$\text{TOTAL \# OF STAGES} = (\log N^*) \frac{\log \log N^* + 3}{2}$$

Figure 5-21. Mapping the shearsort into the two-stage electro-optical network.

## Section 6

# REFERENCES

- 2-1 O. Kibar, P.J. Marchand, and S.C. Esener, "High-Speed 2-D CMOS Designs of Bypass-and-Exchange Switch Arrays for Free-Space Optoelectronic MINs," presented at the *OSA Topical Meeting on Photonics in Switching*, Salt Lake City, March 1995.
- 3-1 G. Marsden, P. Marchand, P. Harvey, and S. Esener, "Optical transpose interconnection system architectures," *Optics Letters* **18** (13), pp. 1083-1085, July 1993.
- 3-2 Ashok V. Krishnamoorthy, Philippe J. Marchand, Fouad E. Kiamilev, and Sadik C. Esener, "Grain-size considerations for optoelectronic multistage interconnection networks," *Applied Optics* **31**, 5480-5507 (1992).
- 3-3 G.J. Swanson, "Binary optics technology: the theory and design of multi-level diffractive optical elements," *DARPA Technical report* **854** (1989).
- 3-4 K.S. Urquhart, "Application of diffractive optics to free-space optical interconnections," Ph.D. Thesis, University of California San Diego, 1992.
- 3-5 K. Urquhart, P. Marchand, Y. Fainman, and S.H. Lee, "Diffractive Optics applied to free-space optical interconnects," *Applied Optics* **33**, 3670-3682, June 1994.
- 3-6 T.C. Chen, "Parallelism, pipelining, and computer efficiency," *Computer Design*, 69-74 (1971).
- 3-7 P. Yeh, "Generalized model for wire grid polarizers," *SPIE Vol. 307*, 13 (1981).
- 3-8 O. Weiner, *Sachsische Akad. Wiss.* 32, 5 (1912).
- 3-9 G. Hass, "Optical properties of metals," *AIP Handbook*, D.E. Gray, ed (McGraw Hill, New York, 1972).
- 3-10 R.E. Slocum, "Evaporative thin metal films as polarizers," *SPIE Vol. 307*, 25 (1981).
- 3-11 Code V is a registered trademark of Optical Research Associates, Pasadena, Ca.
- 4-1 M.S. Welkowsky et al, "Status of the Hughes CCD-addressed Liquid Crystal Light Valve," *Opt. Eng.* 26, 414 (1987).
- 4-2 U. Efron et al, "The CCD-addressed Liquid Crystal Light Valve, - an update," *SPIE Vol. 1455*, 237-247 (1991).
- 4-3 K. Sayyah, M.S. Welkowsky, P.G. Reif, and N.W. Goodwin, "High performance single crystal silicon liquid crystal light valve with good image uniformity," *Applied Optics* 28, (no. 22), 4748-4756 (1989).
- 4-4 Z-Epoxy (ZXUV.102.3012Au) from Zymet, 7 Great Meadow Ln., E. Hanover, NJ 07936

- 5-1 M. Little and J. Grinberg, "The 3-D computer: an integrated stack of WSI wafers," in *Wafer Scale Integration*, Chapter 8, Kluwer Academic Publishers (1988).
- 5-2 F. Kiamilev, E. Stevens, A. Krishnamoorthy, and S. Esener, "A modular architecture for optoelectronic multistage interconnection networks," *International Journal of Optoelectronics*, 9, 6, pp. 457-470, (1994).
- 5-3 N.C. Li, J.L. Haviland, and A.A. Tuszynski, "CMOS tapered buffer," *IEEE J. of Solid State Circuits*, 25, 4, pp. 1005-1008, August 1990.
- 5-4 H.B. Bakoglu, *Circuits, Interconnections and Packaging for VLSI*, (Addison Wesley Publishing Co., 1990)
- 5-5 A. Krishnamoorthy, P. Marchand, F. Kiamilev, K.S. Urquhart, S. Esener, and S.H. Lee, "Grain-size considerations for optoelectronic multistage interconnection networks," *Applied Optics* **31**, 5480-5507, September 1992.
- 5-6 J. Ford, F. Xu, K. Urquhart, and Y. Fainman, "Polarization-selective computer generated holograms," *Optics Letters*, **18**, 456-458 (1993).
- 5-7 A.V. Krishnamoorthy and F. Kiamilev, "Fanout, Replication, and Buffer Sizing for a Class of Self-Routing Packet-Switched Multistage Photonic Switch Fabrics", *Technical Digest, OSA Topical Meeting on Photonic Switching*, Salt Lake City, pp. 87-89, March 1995.
- 5-8 J.W. Cooley and J.W. Tukey, "An Algorithm for the Machine Computation of Complex Fourier Series," *Mathematics of Computation* **19**, p. 297 (1965).
- 5-9 Winthrop W. Smith and Joanne M. Smith, *Handbook of Real-Time Fast Fourier Transforms*, IEEE Press, New York, 1995.
- 5-10 D. Schwartz, Hughes Research Laboratories, Private communication, August 1995.
- 5-11 Richard Tolimieri, Final Report, Contract No. F49620-C-91-0098, Aware Inc., 1 Memorial Drive, Cambridge, MA 02145, Dec. 6, 1994
- 5-12 C. Fan, B. Mansoorian, D. Van Blerkom, M. Hansen, V. Ozguz, S. Esener, and G. Marsden, "Digital free-space optical interconnections: a comparison of transmitter technologies," *Applied Optics* **34** (17), pp. 3103-3115, June 1995.
- 5-13 W. Lee Hendrick, P. Marchand, F.B. McCormick, I. Çokgör, and S. Esener, "Computer Simulation and Optimization of a Free-Space Optical Interconnection System," *SPIE Proceedings of the International Symposium on Optical & Opto-Electronic Applied Science and Engineering*, San Diego, July 1995.
- 5-14 G. Yayla, P. Marchand, and S. Esener, "Analysis of on-chip and off-chip electrical connections in 3-D electronic packages and their comparison to optoelectronic interconnections," UCSD, OptoElectronic Computing Group, Internal Communication.



- 5-15 R. Geiger, P. Allen, and N. Stroder, *VLSI Design Techniques for Analog and Digital Circuits*, McGraw-Hill, New York, 1990, pp. 590-593.
- 5-16 W. Lee Hendrick, O. Kibar, P. Marchand, C. Fan, D. Van Blerkom, F. McCormick, I. Çokgör, M. Hansen, and S. Esener, "Modeling and Optimization of the Optical Transpose Interconnection System," *Optoelectronic Technology Center, Annual Review*, Cornell University, September 1995.
- 5-17 O. Kibar, P. Marchand, and S. Esener, "High-Speed CMOS Switch Designs for Free-Space Optoelectronic MINs," Submitted to *IEEE Transactions on VLSI*, September 1995.
- 5-18 M. Levy and J. Leonard, "DSP-Chip Directory," *Electronic Design News*, pp. 40-92, May 11, 1995.

# DISTRIBUTION LIST

addresses	number of copies
PAUL L. REPAK ROME LABORATORY/OCPC 25 ELECTRONIC PKY ROME NY 13441-4515	5
U. EFRON HUGHES RESEARCH LABORATORIES 3014 MALIBU CANYON ROAD MALIBU CA 90265	5
ROME LABORATORY/SUL TECHNICAL LIBRARY 26 ELECTRONIC PKY ROME NY 13441-4514	1
ATTENTION: DTIC-OCC DEFENSE TECHNICAL INFO CENTER 8725 JOHN J. KINGMAN ROAD, STE 0944 FT. BELVOIR, VA 22060-6218	2
ADVANCED RESEARCH PROJECTS AGENCY 3701 NORTH FAIRFAX DRIVE ARLINGTON VA 22203-1714	1
RELIABILITY ANALYSIS CENTER 201 MILL ST. ROME NY 13440-8200	1
ROME LABORATORY/C3AB 525 BROOKS RD ROME NY 13441-4505	1
ATTN: GWEN NGUYEN GIDEP P.O. BOX 8000 CORONA CA 91718-8000	1

AFIT ACADEMIC LIBRARY/LDEE 1  
2950 P STREET  
AREA 3, BLDG 642  
WRIGHT-PATTERSON AFB OH 45433-7765

ATTN: R.L. DENISON 1  
WRIGHT LABORATORY/MLPD, BLDG. 651  
3005 P STREET, STE 6  
WRIGHT-PATTERSON AFB OH 45433-7707

WRIGHT LABORATORY/MTM, BLDG 653 1  
2977 P STREET, STE 6  
WRIGHT-PATTERSON AFB OH 45433-7739

ATTN: GILBERT G. KUPERMAN 1  
AL/CFHI, BLDG. 248  
2255 H STREET  
WRIGHT-PATTERSON AFB OH 45433-7022

ATTN: TECHNICAL DOCUMENTS CENTER 1  
DL AL HSC/HRG  
2698 G STREET  
WRIGHT-PATTERSON AFB OH 45433-7604

US ARMY SSDC 1  
P.O. BOX 1500  
ATTN: CSSD-IM-PA  
HUNTSVILLE AL 35807-3301

COMMANDING OFFICER 1  
NCCOSC ROTEE DIVISION  
ATTN: TECHNICAL LIBRARY, CODE D0274  
53560 HULL STREET  
SAN DIEGO CA 92152-5001

NAVAL AIR WARFARE CENTER 1  
WEAPONS DIVISION  
CODE 48L0000  
1 ADMINISTRATION CIRCLE  
CHINA LAKE CA 93555-6100

SPACE & NAVAL WARFARE SYSTEMS CMD 2  
ATTN: PMW163-1 (R. SKIANO) RM 1044A  
53560 HULL ST.  
SAN DIEGO, CA 92152-5002

SPACE & NAVAL WARFARE SYSTEMS 1  
COMMAND, EXECUTIVE DIRECTOR (PD13A)  
ATTN: MR. CARL ANDRIANI  
2451 CRYSTAL DRIVE  
ARLINGTON VA 22245-5200

COMMANDER, SPACE & NAVAL WARFARE 1  
SYSTEMS COMMAND (CODE 32)  
2451 CRYSTAL DRIVE  
ARLINGTON VA 22245-5200

CDR, US ARMY MISSILE COMMAND 2  
REDSTONE SCIENTIFIC INFORMATION CTR  
ATTN: AMSMI-RD-CS-R, DOCS  
REDSTONE ARSENAL AL 35998-5241

ADVISORY GROUP ON ELECTRON DEVICES 1  
SUITE 500  
1745 JEFFERSON DAVIS HIGHWAY  
ARLINGTON VA 22202

REPORT COLLECTION, CIC-14 1  
MS P364  
LOS ALAMOS NATIONAL LABORATORY  
LOS ALAMOS NM 87545

AEDC LIBRARY 1  
TECHNICAL REPORTS FILE  
100 KINDEL DRIVE, SUITE C211  
ARNOLD AFB TN 37389-3211

COMMANDER 1  
USAISC  
ASHC-IMD-L, BLDG 61801  
FT HUACHUCA AZ 85613-5000

US DEPT OF TRANSPORTATION LIBRARY 1  
FB10A, M-457, RM 930  
900 INDEPENDENCE AVE, SW  
WASH DC 22591

AWS TECHNICAL LIBRARY 1  
859 BUCHANAN STREET, RM. 427  
SCOTT AFB IL 62225-5118

AFIWC/MSY 1  
102 HALL BLVD, STE 315  
SAN ANTONIO TX 78243-7016

SOFTWARE ENGINEERING INSTITUTE 1  
CARNEGIE MELLON UNIVERSITY  
4500 FIFTH AVENUE  
PITTSBURGH PA 15213

NSA/CSS 1  
K1  
FT MEADE MD 20755-6000

ATTN: DM CHAUHAN 1  
DCMC WICHITA  
271 WEST THIRD STREET NORTH  
SUITE 6000  
WICHITA KS 67202-1212

PHILLIPS LABORATORY 1  
PL/TL (LIBRARY)  
5 WRIGHT STREET  
HANSCOM AFB MA 01731-3004

ATTN: EILEEN LADUKE/D460 1  
MITRE CORPORATION  
202 BURLINGTON RD  
BEDFORD MA 01730

DUSD(P)/DTSA/DUTD 2  
ATTN: PATRICK G. SULLIVAN, JR.  
400 ARMY NAVY DRIVE  
SUITE 300  
ARLINGTON VA 22202

ROME LABORATORY/ERD 1  
ATTN: RICHARD PAYNE  
HANSCOM AFB, MA 01731-5000

ROME LABORATORY/ERDC 1  
ATTN: JOSEPH P. LORENZO, JR.  
HANSCOM AFB, MA 01731-5000

ROME LABORATORY/ERDP  
ATTN: JOSEPH L. HORNER  
HANSCOM AFB, MA 01731-5000

1

ROME LABORATORY/EROC  
ATTN: RICHARD A. SOREF  
HANSCOM AFB, MA 01731-5000

1

ROME LABORATORY/ERXE  
ATTN: JOHN J. LARKIN  
HANSCOM AFB, MA 01731-5000

1

ROME LABORATORY/ERDR  
ATTN: DANIEL J. BURNS  
525 BROOKS RD  
ROME NY 13441-4505

1

ROME LABORATORY/IRAP  
ATTN: ALBERT A. JAMBERDINO  
32 HANGAR RD  
ROME NY 13441-4114

1

ROME LABORATORY/C3BC  
ATTN: ROBERT L. KAMINSKI  
525 BROOKS RD  
ROME NY 13441-4505

1

ROME LABORATORY/DCP  
ATTN: MAJOR GARY D. BARMORE  
25 ELECTRONIC PKY  
ROME NY 13441-4515

1

ROME LABORATORY/GCP  
ATTN: JOANNE L. ROSSI  
25 ELECTRONIC PKY  
ROME NY 13441-4515

1

NY PHOTONIC DEVELOPMENT CORP  
MVCC ROME CAMPUS  
UPPER FLOYD AVE  
ROME, NY 13440

1